West Pomeranian
University of Technology
in Szczecin

mgr inż. Krzysztof Sielicki

Study on application of carbon materials and its hybrids in electrochemistry

Badania nad zastosowaniem materiałów węglowych i ich hybryd w elektrochemii

Doctoral thesis

Supervisor: prof. dr. hab. Ewa Mijowska

Assistant supervisor: dr. hab. Xuecheng Chen, prof. ZUT

Szczecin, 2023

Declaration

I declare, that this thesis represents my work and that is not been previously included in a report, dissertation, or the thesis submitted in any institution for a degree, diploma or other qualification.

Signed_____

Acknowledgement

I would like to take this opportunity to express my deepest gratitude to all those who have contributed to the successful completion of my PhD thesis. This journey has been akin to constructing a ship, and today, as I finished writing my thesis, it feels like setting sail on its much-anticipated maiden voyage. First and foremost, I extend my heartfelt appreciation to my esteemed supervisors, Prof. Ewa Mijowska and Prof. Xuecheng Chen. Their profound knowledge, invaluable guidance, and unwavering support have been instrumental in shaping the course of my research. Their expertise, constructive feedback, and encouragement have steered me in the right direction, ensuring the success of my work. I am truly grateful for their mentorship and the immense contribution they have made to my academic growth.

I am also deeply grateful to my parents, Wojciech and Magdalena, whose unwavering love, boundless support, and sacrifices have been a constant source of strength throughout my journey. Their belief in my abilities and their endless encouragement have propelled me forward, even during the most challenging times. I am forever indebted to them for their unwavering presence in my life and their immeasurable contribution to my personal and academic development.

To my beloved partner, Kamil, I extend my heartfelt gratitude for your unwavering support, understanding, and assistance in every aspect of my life. Your presence by my side has provided me with the strength and motivation to overcome obstacles and pursue my goals with unwavering determination. Your love, encouragement, and belief in me have been the wind in my sails, propelling me towards success. Thank you for being my pillar of support and my greatest source of inspiration.

I would also like to express my sincere appreciation to my colleagues and fellow researchers who have accompanied me on this academic journey. Prof. Beata Zielińska, Dr Karolina Wenelska, Dr Małgorzata Aleksandrzak, Dr Marcin Biegun, Dr Krzysztof Cendrowski, Dr Wojciech Kukułka, Dr Yanliang Wen, Dr Xiaoguang Liu, Xiaodong Xu, Klaudia Maślana, Jiaxin Li, and others – thank you for your collaboration, thought-provoking discussions, and shared experiences. Your contributions have enriched my research and added depth to my work. Your presence has made the journey more meaningful, and I am grateful for the camaraderie and support we have shared. Finally, I would like to express my gratitude to all the individuals and organizations that have

supported me throughout my academic endeavour. Your belief in my abilities, financial assistance, and provision of resources has played a crucial role in the successful completion of my thesis. Your contributions, whether large or small, have been instrumental in my growth and achievements.

To each person mentioned above and to all others who have played a part in my journey, I extend my deepest appreciation and gratitude. Your support, encouragement, and belief in me have been instrumental in shaping the scholar I have become. It is with immense joy, a sense of accomplishment, and profound gratitude that I acknowledge your invaluable presence in my life. Thank you all from the bottom of my heart.

Abstract

This thesis provides an in-depth exploration of hydrogen production processes. It begins by addressing the energy challenges faced by the world and subsequently delves into a range of hydrogen production methods, with a particular emphasis on electrochemical water splitting. The thesis offers a comprehensive explanation of the oxygen evolution reaction (OER) and hydrogen evolution reaction (HER), as well as the catalysts commonly employed in these processes. The experimental section of the thesis focuses on the synthesis and functionalization of aluminium-based metal-organic frameworks (Al-MOF) for electrochemical water splitting, with specific attention given to OER and HER. The research encompasses the synthesis and modification of Al-MOF structures, carbonization processes for catalyst development, and the introduction of cobalt and phosphorus for functionalization. Furthermore, the role of aluminium in enhancing the electrochemical performance of the catalysts is thoroughly explored. The thesis begins by optimizing the carbonization process of Al-MOF, identifying the temperature of 750˚C as the optimal condition for obtaining a highly active and structurally defective carbon platform. Cobalt (Co) is then deposited on the carbonized Al-MOF (CMOF), resulting in the formation of a Co-functionalized CMOF (Co-CMOF). The electrochemical characterization of Co-CMOF reveals an overpotential of 380 mV and a Tafel slope of 75 mV/dec, demonstrating its remarkable electrochemical properties and its ability to compete with the commercial catalyst ruthenium oxide (RuO_2) in OER. In addition to cobalt functionalization, the thesis explores the introduction of phosphorus (P) into the Al-MOF structure. The P-doped CMOF (P-CMOF) exhibits significant improvements in electrochemical performance compared to RuO_2, with an overpotential of 390 mV and a Tafel slope of 103 mV/dec. Phosphorus doping not only enhances the electrochemical properties but also contributes to the healing of the carbon matrix, further improving the catalyst's stability. Mechanistic investigations shed light on the active species formed during polarization at OER potential. TEM analysis reveals the formation of crystalline structures with a d-spacing of 0.24 nm on the surface of Co-CMOF, attributed to the reaction of cobalt from the Co-Al alloy, resulting in the formation of CoOOH species. XPS analysis confirms the disappearance of Co-Al bonds and CoOOH species. Similarly, TEM and XPS analysis of P-CMOF(Al) shows the formation of metallic structures, aluminium oxide (Al_2O_3), and PH_3 gas. Aluminium oxide stabilizes the structure and lowers the catalyst resistance. Although the thesis explores nickel (Ni)

functionalization for HER, the results indicate that further advancements are required to surpass platinum (Pt) catalysts, which currently demonstrate superior performance in HER. This research includes process optimization, mechanistic elucidation, catalyst engineering, scalability, device integration, and the exploration of broader applications beyond water splitting. These studies aim to enhance the efficiency and stability of functionalized Al-MOF catalysts and expand their potential in various electrochemical applications. Overall, this thesis demonstrates the successful functionalization of Al-MOF for electrochemical water splitting, highlighting the excellent electrochemical properties of Co-CMOF(Al) and P-CMOF(Al). The presence of aluminium plays a crucial role in both functionalization and OER, leading to the formation of active species and improving catalyst performance. These findings contribute to the advancement of sustainable energy technologies and offer promising opportunities for the development of efficient and durable electrocatalysts.

Keywords: aluminium-based metal-organic frameworks, electrochemical water splitting, functionalization, oxygen evolution reaction, hydrogen evolution reaction

Streszczenie

Niniejsza praca doktorska przedstawia wprowadzenie do procesu produkcji wodoru różnymi metody. Na początku skupia się na energetycznych wyzwaniach, przed którymi stoi świat. Następnie opisuje szereg metod produkcji wodoru, z naciskiem na elektrochemiczne rozszczepianie wody. Szczegółowo omawia reakcję tworzenia tlenu (OER) i reakcję tworzenia wodoru (HER), a także powszechnie stosowane katalizatory w tych procesach. Sekcja eksperymentalna skupia się na syntezie i funkcjonalizacji struktur metaloorganicznych na bazie glinu (Al-MOF) do elektrochemicznego rozszczepiania wody, ze szczególnym uwzględnieniem OER i HER. Badania obejmują syntezę i modyfikację struktur Al-MOF, proces karbonizacji w celu rozwoju katalizatorów oraz wprowadzenie kobaltu i fosforu do struktury poprzez jej funkcjonalizację. Ponadto, w pracy szczegółowo przeanalizowano rolę glinu w poprawie właściwości elektrochemicznych badanych katalizatorów. Praca w pierwszej części skupia się na optymalizacji procesu karbonizacji Al-MOF, w wyniku czego ustalono, że temperatura 750˚C jest optymalną do uzyskania wysoko aktywnej i o największej liczbie defektów platformy węglowej. Następna cześć badań skupiona była na karbonizowanym Al-MOF (CMOF), na który naniesiono kobalt (Co), co doprowadziło do powstania Co-sfunkcjonalizowanego CMOF (Co-CMOF). Charakterystyka elektrochemiczna Co-CMOF wykazuje nadpotencjał wynoszący 380 mV i nachylenie Tafela wynoszące 75 mV/dec, co świadczy o znakomitych właściwościach elektrochemicznych i zdolności do rywalizacji z komercyjnym katalizatorem, tlenkiem rutenu (RuO_2), w procesie OER. Kolejna część badań skupiona była na wprowadzeniu fosforu (P) do struktury Al-MOF. P-domieszkowany CMOF (P-CMOF) wykazuje istotne polepszenie właściwości elektrochemicznych w porównaniu z RuO_2, z nadpotencjałem wynoszącym 390 mV i nachyleniem Tafela wynoszącym 103 mV/dec. Dodatek fosforu nie tylko poprawia właściwości elektrochemiczne, ale także przyczynia się do naprawy macierzy węglowej, co w następstwie poprawia stabilność katalizatora. Ostatecznie badania mechanizmów reakcji pozwalają zrozumieć powstawanie czynnych składników podczas polaryzacji w warunkach OER. Analiza TEM ujawnia powstawanie nowych struktur na powierzchni Co-CMOF o odstępach międzywarstwowych wynoszących 0,24 nm, co wynika z reakcji kobaltu ze stopu Co-Al, prowadzącej do powstania CoOOH. Analiza XPS potwierdza zanikanie wiązań Co-Al i obecność form CoOOH. Podobnie, analiza TEM i XPS dla P-CMOF(Al) wykazuje powstawanie struktur metalicznych, tlenku glinu (Al_2O_3). Tlenek

glinu stabilizuje strukturę i obniża rezystancję katalizatora. Mimo że w pracy doktorskiej badano także funkcjonalizację niklem (Ni) struktur CMOF w reakcji HER, wyniki wskazują, że konieczne są dalsze badania, aby przewyższyć wydajność katalizatorów platynowych (Pt), które obecnie wykazują znacznie lepszą wydajność w HER. Przyszłe perspektywy tej pracy skupiają się na optymalizacji procesu, wyjaśnianiu mechanizmów reakcji, inżynierii katalizatorów i ich skalowalności i badaniach nad szerszym zastosowaniem poza rozszczepianiem wody. Wysiłki te mają na celu poprawę wydajności i stabilności funkcjonalizowanych katalizatorów Al-MOF oraz poszerzenie ich potencjału w różnych zastosowaniach elektrochemicznych. Podsumowując, niniejsza praca doktorska udowadnia skuteczną funkcjonalizację Al-MOF do elektrochemicznego rozszczepiania wody, podkreślając doskonałe właściwości elektrochemiczne Co-CMOF(Al) i P-CMOF(Al). Obecność glinu odgrywa kluczową rolę zarówno w procesie funkcjonalizacji, jak i w OER, prowadząc do powstania elektroaktywnych substancji i poprawy wydajności katalizatora. Wyniki przyczyniają się do rozwoju zrównoważonych technologii energetycznych i otwierają obiecujące możliwości rozwoju wydajnych i trwałych elektrokatalizatorów.

Słowa kluczowe: sieci metalicznoorganiczne na bazie glinu, elektrochemiczne rozszczepianie wody, funkcjonalizacja, reakcja wydzielania tlenu, reakcja wydzielania wodoru

Contents

List of abbreviations

AdEM – adsorbate evolution mechanism

AEL – alkaline electrolysis

AEM – anion exchange membrane

AFC – alkaline fuel cell

BET - Brunauer–Emmett–Teller

BP – bipolar plates

CA- cyanamide

CB – conductive band

C_{dl} – double-layer capacitance

CE – counter/auxiliary electrode

CFE - capillary-fed electrolysis

CMOF - carbonized metal-organic framework

CRM – critical raw materials

CV - cyclic voltammetry

DC – direct current

DCP – diphenyl chlorophosphate

dec – decade [log(j)]

DFT – density functional theory

DMF - dimethylformamide

EIS – electrochemical impedance spectroscopy

FE – Faraday's efficiency

g-C_3N_4 – graphitic carbon nitride

GEIS – galvanostatic electrochemical impedance spectroscopy

HBE – hydrogen binding energy

hcp – hexagonal closed-packed

HER – hydrogen evolution reaction

HFC – hydrogen fuel cell

HKUST – MOF (Hong Kong University of Science and Technology)

HOR – hydrogen oxidation reaction

HR-TEM – high-resolution transmission electron microscopy

j – current density

LbL – layer by layer

LOM – oxygen lattice mechanism

LSV – linear sweep voltammetry

LSV -linear sweep voltammetry

MIL - MOF (Materials Institute Lavoisier)

MOE- mercury oxide electrode

MOF – metal-organic frameworks

NP – nanoparticles

OCV – open circuit voltage

OER – oxygen evolution reaction

O_L – oxygen lattice

ORR – oxygen reduction reaction

PDA - polydopamine

PDC – pyridinic dicarboxylic acid

PEIS – potentiostatic electrochemical impedance spectroscopy

PEM – proton exchange membrane

PEMFC – polymer exchange membrane fuel cell

RE – reference electrode

RHE – reversible hydrogen electrode

R_u – uncompensated resistance

SA – single atoms

SAC – single-atom catalyst

SOEC – solid oxide electrolysis cell

SOFC – solid oxide fuel cell

SSA – specific surface area

SWCNT – single-walled carbon nanotubes

TEM – transmission electron microscopy

TGA – thermogravimetric analysis

TMP – transition metals phosphides

TO - transverse optical phonon mode

TOF – turnover frequency

Twh – terawatts-hours

UiO – MOF (Universitetet i Oslo)

UV – ultraviolet light

V_a – sinusoidal voltage amplitude

VB – valence band

V_O – oxygen vacancy

WE – working electrode

XAS -X-ray absorption spectroscopy

XPS – X-ray photoelectron spectroscopy

XRD – X-ray diffraction

YSZ – yttria-stabilized zirconia

ZIF- zeolitic imidazolate framework

Chapter I: Introduction

1. Background and motivation

We live in a world that is developing extremely rapidly across a wide range of platforms, and this pace is increasing. The computer era has made many things dependent on computers and electronic devices. We usually realize this when there is a shortage of electricity. As a result, it becomes evident that there is a need for new power sources and better energy storage. The goal is to achieve a state of mind in which we are no longer concerned with electricity. In order to attain such a state, however, there is still a lot to be done. Furthermore, we must take into account the condition of our planet. Therefore, we should work harder to protect our world from waste by designing recyclable materials. At the moment, the geopolitical situation reveals how critical energy sources are. New, renewable energy sources that are easily accessible throughout the world should receive all of the attention.

Therefore, the most popular eco-friendly fuel is hydrogen. As the lightest element, hydrogen is ideal as a fuel, since it produces only water molecules when electricity is generated. To make it efficient and accessible, many obstacles need to be overcome. Firstly, the hydrogen production process consumes a lot of electricity and time. Next, hydrogen must be stored, which requires advanced materials. Finally, it must be transformed into water in an electrochemical process in a hydrogen fuel cell. Therefore, the most efficient process of hydrogen evolution is electrochemical water splitting. This is where current is applied to the electrocatalyst and hydrogen is generated. Usually, the catalysts are critical raw materials (CRM) like platinum, ruthenium or iridium [1]. Commercially, platinum is deposited on a carbon platform with a mass loading of at least 20%. All of them are expensive and access is limited. In order to replace CRM, some new electrocatalysts should be proposed.

It is ideal for carbon to serve as an electrocatalyst when enriched with other atoms: non-metallic (e.g. boron - B, nitrogen - N, phosphorus - P), metallic (e.g. cobalt - Co, iron - Fe, nickel - Ni) or a combination of both. In terms of functional materials, carbon materials represent a broad range of structures with unique architectures that provide a wide variety of design opportunities. As compared to metal-based electrocatalysts, carbon-based materials show critical disadvantages arising from poor activity and low

durability under harsh conditions. Although carbon composites are relatively inexpensive, they are easily accessible, and they have a wide range of tuning capabilities.

Among the materials that combine metals and carbon are metal-organic frameworks (MOF), which can be transformed into carbon-metal composites through high-temperature treatments. Furthermore, the materials exhibit high porosity, unique structure and are readily synthesized by self-assembly. MOF can serve a wide range of applications due to their high porosity (sorption, catalysis), tuneable structure (energy storage) or composite nature (electrocatalysis and energy storage). However, MOF synthesis is strongly temperature- and time-dependent. Therefore, its synthesis is susceptible to several factors that have a direct impact on its final structure.

Taking into consideration the myriad challenges delineated above, encompassing the substantial global energy demand, hydrogen fuel production, inherent drawbacks associated with electrocatalysts, and the burgeoning prospects for MOF utilization, the principal motivation behind this thesis resides in the pursuit of rigorous research concerning MOF and carbonized MOF for the domain of electrochemical water splitting. The crux of this research centres on the careful examination of MOF structure design, processing methodologies, and their targeted implementation within one of the paramount electrochemical water splitting reactions, namely, the oxygen evolution reaction (OER). Within this thesis, a comprehensive evaluation of distinct MOF structures and MOF-based composites will be presented, unveiling a detailed comparison of their electrochemical performance in conjunction with accurate physicochemical analyses. It is noteworthy to emphasize that water splitting comprises two indispensable half-reactions, and the OER component specifically poses a considerably more arduous challenge due to its slower kinetics and more complex reaction pathway.

2. Energy needs and challenges

Electric energy consumption has risen over the years so significantly, that when we compare its usage in the USA in 1950 and 2021, it has grown over 13 times [2]. For the European Union, electricity production grew from 2132 TWh (terawatt-hours) in 1990 to 2785 TWh in 2021 [3]. Population directly influences electricity consumption, therefore, in Asia, consumption is the highest. The analyses show that just for Southeast Asia consumption increased from 500 TWh in 1990 to 1500 TWh in 2020 and in 2050 will reach over 4000 TWh [4]. The data indicate that the demand for electrical energy is extremely high and is expected to increase exponentially soon. Nevertheless, a greater

need for energy (production and consumption) is not the only challenge that will emerge in the future. According to the current trend for the decarbonization of the energy sector [5], coal and methane will no longer be burned for electricity generation. It is due to two main reasons 1) the limitations of coal and natural gas resources and 2) concern for the environment. Therefore, more capacity for energy storage will be required and other energy sources such as renewable energy or hydrogen production will be intensively developed [5].

The environment is intensively impacted by fossil fuels mining and energy generation. The main source of energy is still based on carbon/natural gas burning, causing the greenhouse effect due to CO_2 emission and global warming [6]. However, the trend is changing [7], where renewable energy sources (solar, wind, geothermal, hydropower, and bioenergy) play a key role in big countries' electricity sources. Renewable energy sources are the most intensively developed energy sources nowadays. It also led to the development of energy infrastructure. Fossil fuels cannot be stopped instantly from use. That is why one of the main research areas is carbon capture, where CO_2 is collected and not released into the atmosphere. Captured carbon dioxide can be utilized in industrial processes or stored underground [5]. The biggest problem, however, remains that not all developed countries are still relying on fossil fuels or the import of fossil fuels.

The current policy for the energy sector is in correlation with worldwide energy trends and the main goals are to reduce carbon emissions as much as possible and to mainly produce energy from renewable sources [8–11]. Almost all the biggest energy producers (the USA, China, Japan and the EU) presented their long-term plans to reduce the greenhouse effect and produce green electricity. Therefore, a lot of money and effort is put into our planet's well-being. However, electricity needs to be stored and easily used e.g. in transportation. Especially important is the transportation sector, which is a hot topic in the European Union due to the ban on the sale of new petrol and diesel cars from 2035 [12]. This will focus all attention on electrical vehicles and electric energy storage, therefore the industry will force the development of cutting-edge technologies and materials. Additionally, environmental protection is pushed forward even further. While renewable energy sources are being developed, hydrogen is also being developed as a clean fuel. For this reason, industry, science and government are emerging into regional groups for hydrogen production, development and distribution called "hydrogen valleys". Nowadays, there are more than 37 hydrogen valleys in over 20 countries, mainly located

in the European Union [13,14]. Therefore, world policy focuses on the green production of electricity from renewable energy sources and the development of hydrogen as a green fuel.

3. Objective and scope of the thesis

The thesis presenting the fundamentals of electrochemical water splitting and the challenges that has to be overcome for efficient hydrogen production. The main objective is to design and synthesis efficient electrocatalyst that overcomes the challenges and show appropriate properties towards efficient water splitting. The thesis explores the electrochemical response tuned by structural properties in carbonized metal-organic frameworks (CMOF) materials. Al-MOF structures are modified in two different approaches 1) *in-situ*, when during synthesis to reaction mixture the electrocatalytic metals are added and 2) *ex-situ*, where to the CMOF electrocatalytically active metals are added. Then both routes of modifications are investigated in two half-reactions that describe water splitting – HER and OER. Therefore, the initial modification involves metal doping (cobalt/nickel/platinum) into Al-MOF followed by carbonization and directly into nitrogen-rich carbon (CMOF), exposing aluminium nanoparticles. In this investigation, considerable attention is devoted to scrutinizing the impact of the carbonization process on the ultimate structure of the materials, followed by further functionalization through OER/HER electrocatalysts. The subsequent modification enhances electrical properties via nitrogen-rich carbon doped with phosphorus. Both strategies present distinct methodologies for enhancing OER/HER electrocatalysts and scrutinizing the transformations that emerge during the electrochemical processes.

The thesis also includes detailed ex-situ analysis techniques such as X-ray diffraction (XRD), transmission electron microscopy (TEM), and X-ray photoelectron spectroscopy (XPS). These techniques are employed to investigate structural and chemical changes in carbonized MOF structures. The results obtained from the *ex-situ* analysis inform the proposal of mechanisms to explain the observed improvements in electrochemical properties.

In summary, this thesis provides a comprehensive understanding of Al-MOF and carbonized MOF structures based on aluminium. It encompasses the modification of carbon with nitrogen and phosphorus, the modification of Al-MOF with cobalt/nickel/platinum and CMOF with cobalt, the impact of aluminium on

electrochemical properties and stability, detailed *ex-situ* analysis, and the proposal of mechanisms underlying the observed enhancements in electrochemical properties.

Chapter II: Water Splitting

1. Different methods and technologies for hydrogen generation

New green fuel – hydrogen, has recently brought a lot of attention due to climate changes and the geopolitical situation. High demand for energy and energy policies in many countries focused on the development of renewable energies. Cheaper and more accessible electrical energy from those sources makes hydrogen generation extremely attractive. Hydrogen can be produced through various methods and technologies (Figure 1), from which the electrolysis of water is most efficient.

Figure 1. Different types of hydrogen based on the process and source of its production.

1.1 Natural gas reforming

The fossil fuel transformation into hydrogen is a well-known process. Therefore, instead of gas, coal can be used instead. It is a fossil fuel-based hydrogen generation, where CO_2, CO, CH_4 and H_2 are involved. It is however not the ecological way to produce hydrogen, whereas for every ton of hydrogen, about 5 tons of CO_2 is produced and 2.5 tons are released into the atmosphere [15]. The reforming is managed at a high temperature of at least 500˚C with nickel as a catalyst in reactions:

$$CH_4 + H_2O \rightarrow CO + 3H_2,$$
$$CO + H_2O \rightarrow CO_2 + H_2.$$

Natural gas is mostly composted from methane (CH_4) due to organic matter decomposition. Therefore, it can be collected from biomass. However, the majority of natural gas is still mined from natural gas wells located near coal or oil mines. Another obstacle to reforming fossil fuels is sulphur contamination. To produce hydrogen, desulfurization is required. This process can be conducted in two routes: 1) high temperature (350-400˚C), for large-scale production, where the catalysts are lead oxide, cobalt oxide or molybdenum oxide, 2) low-temperature process (<300˚C), where the process is based on adsorption of sulphide by-products rather than a chemical reaction in the first process [16–19].

1.2 Biomass gasification

As a result of thermochemical reactions involving gasification, biomass, a widely investigated material group, can be transformed into hydrogen. It is a process which includes pyrolysis, oxidation and reduction in an atmosphere of air, water vapours and other gasification agents under high-temperature conditions. Gasification produces: CO, H_2 and CH_4. Biomass gasification shows an advantage over coal gasification, where a lower temperature (600-800˚C) is required (coal above 1000˚C). Biomass gasification can be classified as pyrolysis gasification (lowest H_2 generation rate), oxygen-rich gasification, steam gasification and supercritical water gasification (most efficient gasification) [16]. Pyrolysis gasification is as follows:

$$biomass \xrightarrow{heat} CH_4 + CO + H_2 + other\ products,$$

while oxygen-rich/steam gasification is as follows:

$$biomass \xrightarrow{O_2 or H_2O} H_2O + CO + CO_2 + CH_4 + H_2 + other\ CHs + char + tar + ash.$$

1.3 Supercritical water gasification

Under a temperature and pressure above its critical point temperature, supercritical water has unique properties. It presents strong solubility in solving organic compounds from biomass and forming liquids with high density and low wage. Such mixtures, when

rapidly vaporized under high pressure and high temperatures, produce a mixture of gases with hydrogen. The advantage of supercritical water gasification is that it not requires a drying process. It is also more efficient than steam gasification due to not forming a tar above 600˚C. The chemical process of supercritical water gasification is composed of three reaction paths that take place simultaneously [16]:

$$biomass + H_2O \rightarrow CO + H_2$$
$$CO + H_2O \rightarrow CO_2 + H_2$$
$$CO + H_2 \rightarrow CH_4 + H_2O$$

1.4 Water photolysis

It has been known for more than 50 years that photocatalytic reactions are possible, starting with a published paper by Fujishima and Honda [20], where light irradiation was used to photolyze water on titanium dioxide (TiO_2). During heterogeneous reactions, light (visible or UV) is used to irritate the semiconductor. In the case of higher energy than the bandgap, electrons are excited from the valence band (VB) to the conduction band (CB), and positively charged holes are formed in their place in the VB. However, the process shows low efficiency and sacrificial reagents are added, forming not only hydrogen but also organic side products. Moreover, the reaction:

$$H_2O \xrightarrow{light} H_2 + {}^1\!/_2\, O_2$$

is challenging due to 1) water oxidation to oxygen, 2) protons reduction to hydrogen and 3) inhibiting the reverse reaction (which is more favourable) of oxygen and hydrogen back to the water. For this process to be applied in mass production, many obstacles need to be overcome, such as boosting the quantum efficiency of visible light and scaling up the photocatalytic process [21].

1.5 Water electrolysis

At first, water electrolysis was noneconomic due to the high costs of electric energy. However, recent development in renewable energies and progress in catalysts advance made it more accessible for broader application and use. Water splitting is an endothermic reaction, so energy has to be delivered. It consists of two reactions on the cathode– hydrogen evolution reaction (HER) and anode – oxygen evolution reaction (OER), both separated by a membrane. Both reactions have different pathways depending on the pH of the electrolyte as follows:

in acidic electrolytes:

HER $4H^+ + 4e^- \rightarrow 2H_2$,

OER $2H_2O \rightarrow 4H^+ + O_2 + 4e^-$,

in alkaline electrolytes:

HER $2H_2O + 4e^- \rightarrow 2H_2 + 4OH^-$,

OER $4OH^- \rightarrow O_2 + H_2O + 4e^-$.

The thermodynamic potential for water splitting is 1.23 V with the addition of potential called overpotential (η) due to energy barriers related to kinetics and mass transportation. Moreover, the additional potential is required to overcome the resistances of electrolyte, contact, and membrane followed by the resistance of side reactions like electrode corrosion and dioxygen reduction. The contact resistance can be further driven by the diffusion of the reactants and gas products. Overall potential can be presented as follows:

$$E = 1.23\,V + \eta_{HER} + \eta_{OER} + \eta_{other},$$

where E is applied potential, η_{HER} is HER overpotential, η_{OER} is OER overpotential and η_{other} is a sum of system voltage drops [22].

2. Principles of water splitting

As a general rule, water splitting is the process of splitting a water molecule into hydrogen and oxygen molecules. However, the process is not spontaneous and must be driven by an external force, which in this instance is electric current. The current depends on the pH of the electrolyte when voltage is applied. The total reaction where hydrogen and oxygen are generated can be divided into two half-reactions: the hydrogen evolution reaction (HER) and the oxygen evolution reaction (OER). For both reactions, plenty of obstacles are present: 1) system resistances – between catalyst and electrode, between a catalyst and the electrolyte, 2) overpotential of electrocatalytic process induced the catalyst, any departure from theoretical voltage values for half-reactions (0 V for HER and 1.23 V for OER), 3) kinetics of the reaction [16].

The hydrogen evolution reaction is a two-electron migration process. It can be divided by the adsorption-desorption process into [23]:

Acidic electrolyte	**Alkaline electrolyte**
$\boldsymbol{2H^+ + 2e^- \rightarrow H_2}$	$\boldsymbol{2H_2O + 2e^- \rightarrow H_2 + OH^-}$

$H^+ + e^- \rightarrow H_{ads}$	**Volmer step**	$2H_2O + 2e^- \rightarrow 2H_{ads} + 2OH^-$
$2H_{ads} \rightarrow H_2$	**Tafel step**	$2H_{ads} \rightarrow H_2$
$H^+ + H_{ads} + e^- \rightarrow H_2$	**Heyrovsky step**	$H_2O + H_{ads} + e^- \rightarrow H_2 + OH^-$

However, the oxygen evolution reaction depending on pH shows much-complicated reaction paths [24]:

Acidic electrolyte	**Alkaline electrolyte**
$\boldsymbol{2H_2O \rightarrow O_2 + 4H^+ + 4e^-}$	$\boldsymbol{4OH^- \rightarrow O_2 + 4H_2O + 4e^-}$
$OH^* \leftrightarrow O^* + H^+ + e^-$	$OH^- + OH^* \leftrightarrow O^* + H_2O + e^-$
$H_2O + O^* \leftrightarrow OOH^* + H^+ + e^-$	$O^* + OH^- \leftrightarrow OOH^* + e^-$
$OOH^* \leftrightarrow * + O_2 + H^+ + e^-$	$OOH^* + OH^- \leftrightarrow * + H_2O + O_2 + e^-$
$H_2O + * \leftrightarrow OH^* + H^+ + e^-$	$OH^- + * \leftrightarrow OH^* + e^-$

Comparing those two half-reactions, it is clear that OER has more complexity and steps to start water splitting, OER also requires a higher potential - 1.23 V. However, some energetic barrier occurs when voltage is applied, therefore overpotential (η) is inevitable. The overpotential is the excess of potential that has to be applied for the splitting of water to begin, e.g. graphene shows 540 mV of overpotential, which drops to 330 mV after phosphorus doping[25]. It indicates that pristine materials must be modified/functionalized to lower the overpotential as a critical parameter of water splitting. Through linear sweep voltammetry (LSV), polarization curves can be determined to estimate overpotentials. In electrolytic cells driven by photoelectric, overpotential equals current density (10 $mA \cdot cm^{-2}$) required for water splitting by electrolytic cells to produce 10% efficiency of solar water decomposition and conversion [16]. The efficiency of water splitting is tidily bonded with reaction kinetics. To determine it, the Tafel slope is calculated, where overpotential (η) vs. logarithm of current density (j) is linearly fitted:

$$\boldsymbol{\eta = a + b}\,log\boldsymbol{j} \qquad (1)$$

In equation (1) the b refers to the Tafel slope, however, it can be calculated as presented in Figure 2. Usually, the lower the slope value the faster the current density rises with an increase of external potential. The exchange current density (j_0) can be calculated from the same equation (1) for $\eta = 0$. As a result of material intrinsic properties,

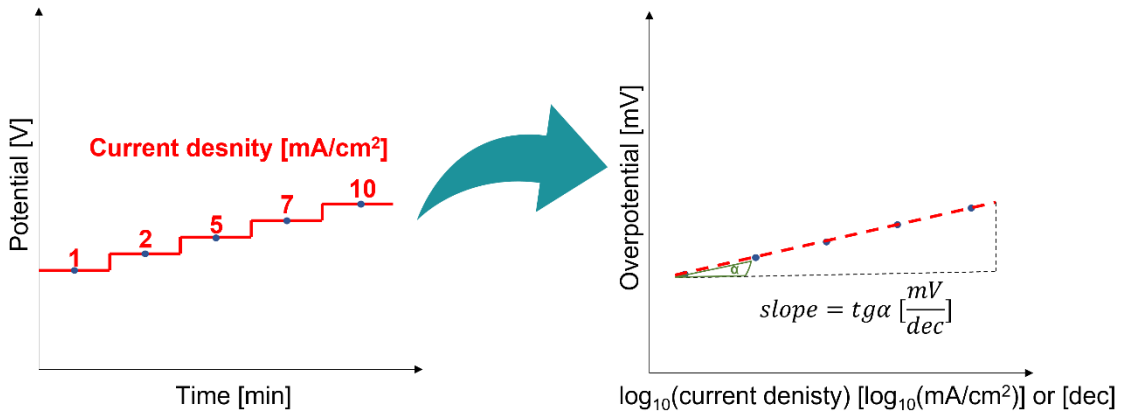

Figure 2. Chronopotentiometry measurement of system response to applied current over time (left) and Tafel slope calculated from this measurement (right).

it is a current signal formed under the equilibrium potential, which describes the material's intrinsic ion adsorption and desorption activities.

Additionally, it is possible to measure the electrochemical active surface area (ECSA) by integrating the current response from the double-layer capacitance (C_{dl}) via cyclic voltammetry (CV) measurement. The CV curves in a non-faradaic region (capacitive process, the charge is progressively stored) are plotted as a function of various scan rates (e.g. 20 mV/s, 50 mV/s, 100 mV/s, and 200 mV/s). Then, the double layer capacitance (C_{dl}) is assessed from the slope of the linear regression between the current density differences ($\Delta j/2 = (j_{anodic}-j_{cathodic})/2$) in the middle of the potential window of CV curves versus scan rates. C_s stands for the specific capacitance of standard electrode materials on a unit surface area (Figure 3). In the literature, C_s values for carbon electrode materials were usually calculated based on 0.02 mF/cm^2. The ECSA can be converted from cm^2 to m^2/g by dividing the ECSA area by the mass loading of catalysts [26].

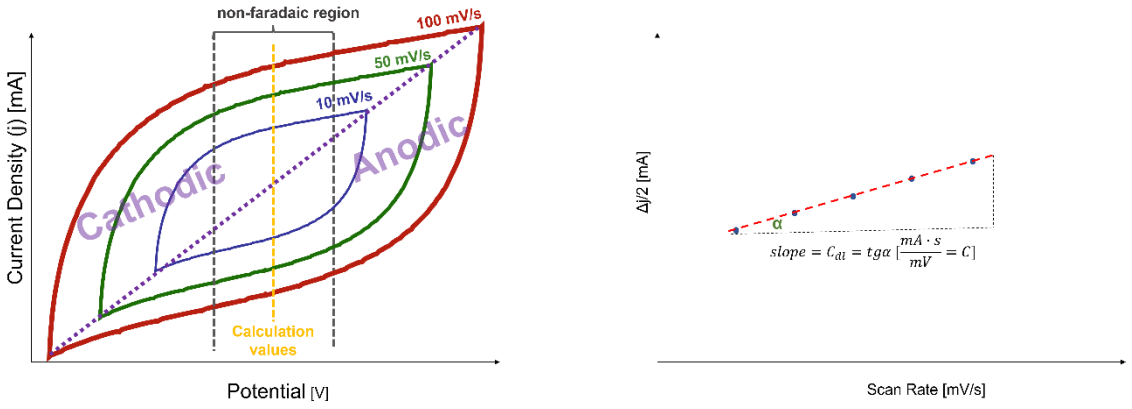

Figure 3. CV measurements for different scan rates (left) and current difference vs scan rate (right).

Another parameter that describes the water splitting is the turnover frequency (TOF), called also conversion frequency. TOF refers to the number of reactions occurring per unit of time and unit active site under certain conditions of temperature, pressure, reactant ratio, and reaction degree [16]. TOF directly indicates the speed of the reaction and can be calculated from equation (2):

$$TOF = \frac{jA}{zFN}, \quad (2)$$

where j is current density, A is an electrochemically active area, Z is the number of transferring electrons generated by each molecule, F is Faraday's constant F= 96 485.3321 $A \cdot s \cdot mol^{-1}$ and N is the amount of matter (mol).

The reaction is not always carried out by all sites, as should be noted. Furthermore, it is very common for some active sites to become "hidden" as the reaction proceeds. When this occurs, the calculated TOF value is often low, even though the material is highly active. For comparing catalysts' activities with those reported in the literature, the TOF value is nevertheless a very high reference value [16]. The stability of electrocatalysts for water splitting is one of the most important parameters despite their electrochemical performance. Under the condition of continuous current, the electrocatalyst can maintain a constant voltage. Generally, chronopotentiometry and chronopotentiometry are used to observe changes in potential under constant current and constant potential, respectively. A wide range of currents can be tested with multistep chronopotentiometry, in particular. Stability tests can also be conducted by comparing the LSV curves before and after electrochemical reactions [16]. Faraday efficiency refers to the proportion of moles of real products produced compared to theoretical products. Factors such as temperature, electrolyte concentration, applied voltage, solution acidity, and electrode material purity can influence this efficiency. The formula to calculate Faraday efficiency (FE) is:

$$FE = \frac{m \cdot n \cdot F}{I \cdot t}, \quad (3)$$

where M represents the actual number of moles of products, n is the number of reactive electrons, F is the Faraday constant that denotes the charge contained in a mole of electrons, I is current, and t is the time.

Electrocatalytic water splitting is measured by comparing the measured hydrogen/oxygen production to the calculated hydrogen/oxygen production for a constant current catalytic reaction. In practical applications, the actual number of electrons used in REDOX reactions can be determined by collecting the volume of gas generated per unit time [16].

When two half-reactions (HER and OER) are combined in one electric device, we talk about electrolyzer. However, when two opposite processes – hydrogen oxidation reaction (HOR) and oxygen reduction reaction (ORR) are combined in the device, it is called a hydrogen fuel cell. The schematic representation of all four processes in the form of polarization curves is presented in Figure 4.

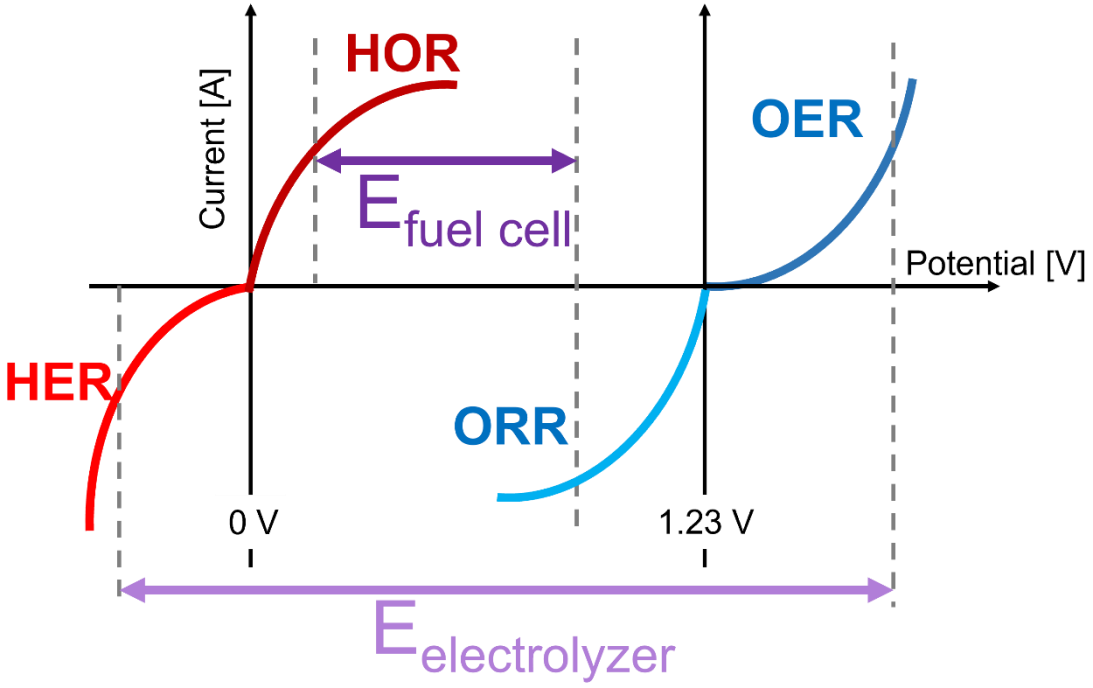

Figure 4. Schematic representation of polarization curves for HER, HOR, ORR and OER.

2.1 Electrolyzers

Electrolyzers can process water splitting by electric potential, where water molecules are dissociated by an electric field (HER and OER). Hydrogen is evolved on the cathode (-) and oxygen on the anode (+). Between electrodes lies an electrolyte, which is an electrical insulator, an ionic conductor and the source of water molecules. The ions in the electrolyte are mostly H^+, OH^- or O^{2-} and are transferred between electrodes. The electrolyzers can be divided into four main groups (Figure 5): 1) proton exchange membrane (PEM), 2) anion exchange membrane (AEM), 3) alkaline electrolysis (AEL) and 4) solid oxide electrolysis cell (SOEC). The first two are based on the membrane

between the electrodes where H^+ (PEM) is transferred from anode to cathode or OH^- from anode to cathode (AEM). In alkaline electrolyzers, alkaline electrolytes are used between electrodes, which provide excess OH^- ions. The SOEC is based on the transfer of O^{2-} anions through solid electrolytes. Furthermore, four of the processes require different temperatures to operate: <80˚C (PEM,AEM), <220˚C (AEL) and above 600˚C (SOEC) [27–29].

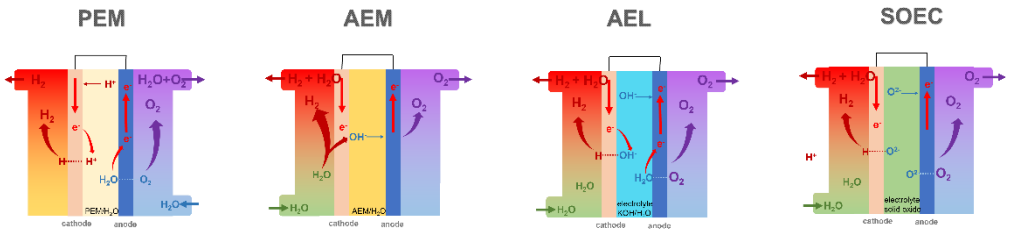

Electrolyte	acidic	alkaline		O_2^- - conducting
Type	solid (polymer)		liquid	solid (ceramic)
Working temperatures	50 – 80 ˚C	40 – 80 ˚C	95 – 220 ˚C	700 – 1000 ˚C

Figure 5. Schematic representation of different types of electrolyzers and their working parameters.

2.1.1 Proton Exchange Membrane (PEM) electrolysis

Proton exchange membrane (PEM) electrolysis was first conducted in the early fifties by Grubb and General Electric Co. The polysulfonated membrane (Nafion®, fumapem®) plays a crucial role in water electrolysis as a proton conductor [30]. PEM water electrolysis involves the electrochemical separation of water into its constituent elements, hydrogen and oxygen, at the cathode and anode respectively. In the process, water is pumped to the anode, where it splits into oxygen (O_2), protons (H^+), and electrons (e^-). The protons then pass through a proton-conducting membrane to the cathode side, while the electrons exit from the anode through an external power circuit that provides the driving force or cell voltage for the reaction. The first generation of PEM electrolyzers was similar to the first generation of AEL electrolyzers, where the electrolyte was between the electrodes and membrane. The next generation of PEM electrolyzers (from 1970) was based on zero-gap systems, where the cathode and anode were separated by membrane without electrolyte between them; each electrode has contact with an electrolyte. PEM electrolyzers use the same system as zero-gap electrolyzers, but there is no contact with the electrolyte at the cathode side. A proton can only be transferred from the anode through contact with the electrolyte to the cathode, where hydrogen is generated. Capillary-fed electrolysis (CFE) has been recently developed to minimize

contact between the electrolyte and electrodes, thereby preventing oxygen and hydrogen bubbles [29]. The reactions on the electrodes are as follows:

$2H_2O \rightarrow 4H^+ + O_2 + 4e^-$	anode
$4H^+ + 4e^- \rightarrow H_2$	cathode
$2H_2O \rightarrow 2H_2 + O_2$	total reaction

The advantages of PEM electrolyzers are low gas permeability, high proton conductivity (~0.1 $S \times cm^{-2}$) lower thickness than AEL and high-pressure operation. Furthermore, PEM is highly durable for up to 10 years of continuous use. Moreover, the PEM is capable of high current density (above 2 $A \times cm^{-2}$), high efficiency with fast response and producing ultrapure hydrogen [27]. Nevertheless, some disadvantages are still present. The biggest challenge to overcome is to reducing PEM cost production. 40% of the cost is the catalysts (HER: Pt/Pd; OER: IrO_2/RuO_2). Bipolar plates (BP), which act as heat and electric conductors, as well as channels for gas and electrolytes, are also expensive parts. The most expensive component is still electricity, which can be reduced by designing better electrocatalysts with lower overpotentials and improved kinetics or by harvesting renewable sources of energy.

2.1.2 Anion Exchange Membrane (AEM) electrolysis

Anion exchange membrane (AEM) electrolysis is a type of water electrolysis that uses an anion exchange membrane to facilitate the electrolytic process. In AEM electrolysis, the anode and cathode are separated by a membrane that selectively conducts anions, while preventing cations from passing through. When an electric current is applied, water molecules are split into hydrogen ions (H^+) and hydroxide ions (OH^-) at the anode and cathode respectively. The hydrogen ions migrate through the anion exchange membrane to the cathode, where they combine with electrons from the external circuit to produce hydrogen gas (H_2). The hydroxide ions migrate through the membrane to the anode, where they combine with electrons to produce oxygen gas (O_2). AEM is a third generation of electrolyzers - it utilizes the advantages of both PEM – solid polymer electrolyte architecture and high performance and selectivity and AEL – low-cost electrocatalytic materials and alkaline electrolysis. Similarly to PEM, the AEM system is also based on zero-gap architecture, whereas the polymer membrane is composed of quaternary ammonium salts [28]. The reactions on the cathode and anode are as follows:

$4OH^- \rightarrow 2H_2O + O_2 + 4e^-$	anode
$2H_2O + 4e^- \rightarrow 2H_2 + 4OH^-$	cathode
$2H_2O \rightarrow 2H_2 + O_2$	total reaction

The advantages of AEM electrolyzers are mostly low costs of production due to reduced capital costs and cheaper electrode materials. AEM systems are also less sensitive to impurities of the electrolyte, which allows broader electrolytes to be used. Finally, AEM electrolyzers show higher durability than PEM systems, which directly impacts the long-term performance of the electrolyzers. However, AEM systems present some drawbacks: they show poorer energy conversion than PEM systems, present slower response time and have lower hydrogen purity than PEM electrolyzers.

2.1.3 Alkaline electrolyzer (AEL)

An alkaline electrolyzer (AEL) is a technology the first commercial technology used to produce hydrogen and oxygen from water using an alkaline solution as an electrolyte. The process involves applying electric current to water, which splits water molecules into hydrogen and oxygen gases at the cathode and anode, respectively. The AEL electrolysis cell consists of two electrodes (anode and cathode) separated by a porous membrane, commonly composed of a polymer material, that allows the passage of hydroxide ions (OH-) between the electrodes. The anode is made of a material that resists corrosion in the highly alkaline electrolyte, typically nickel or a nickel alloy. The cathode is made of a material that is highly conductive and catalytic to the hydrogen evolution reaction. This is typically a metal such as platinum or a nickel-based alloy. During AEL electrolysis, an alkaline solution, such as potassium hydroxide (KOH), is used as the electrolyte, which provides hydroxide ions for the electrochemical reaction. Electrolyte concentration must be carefully controlled to maintain high conductivity while avoiding side reactions and membrane degradation [27]. The reactions on the cathode and anode are the same as for AEM electrolysis:

$4OH^- \rightarrow 2H_2O + O_2 + 4e^-$	anode
$2H_2O + 4e^- \rightarrow 2H_2 + 4OH^-$	cathode
$2H_2O \rightarrow 2H_2 + O_2$	total reaction

The advantage of AEL is that the technology is developed for more than 100 years. Moreover, it presents the highest nominal output of >200 MW and lowest investment

costs of 1000 €/kW followed by a long lifetime. The total costs and accessibility strongly impact the fact that this type of electrolyzer does not require the CRM for electrodes. However, the AEL technology also has some limitations, such as the requirement for a highly alkaline electrolyte, which can be corrosive and hazardous. Additionally, AEL electrolyzers are typically less efficient than PEM electrolyzers. Moreover, AEL presents a vulnerability to impurities in the product gases and a relatively long cold start time (~50 min; for PEM it is ~15 min) [27,30].

2.1.4 Solid oxide electrolysis cell (SOEC)

Solid electrolyte electrolysis cell (SOEC) of water is a type of water electrolysis in which a solid-state electrolyte is used instead of a liquid or polymer electrolyte. In this process, water is split into hydrogen and oxygen at the anode and cathode, respectively, under the influence of an electric current. The solid-state electrolyte is typically a ceramic material that is ionically conducting at high temperatures, usually above 600°C. Briefly, the process is as follows: water vapour is introduced into an oxide electrolysis cell, then a solid electrolyte (e.g. ceramic material such as yttria-stabilized zirconia - YSZ) transfers oxygen ions from the cathode to the anode. Next, at the anode, oxygen ions react with water to form oxygen gas and electrons. The electrons are conducted through an external circuit to the cathode where they react with hydrogen ions to form hydrogen gas [27]. Reaction in SOEC at the cathode and the anode are as follow:

$2O^{2-} \rightarrow O_2 + 4e^-$	anode
$2H_2O + 4e^- \rightarrow 2H_2 + 2O^{2-}$	cathode
$2H_2O \rightarrow 2H_2 + O_2$	total reaction

What is more interesting, is that SOEC can be used for CO_2 reduction in a similar system [31], where instead of water CO_2 is a source. The reactions are as follows:

$2O^{2-} \rightarrow O_2 + 4e^-$	anode
$2CO_2 + 4e^- \rightarrow 2CO + 2O^{2-}$	cathode
$2CO_2 \rightarrow 2CO + O_2$	total reaction

Therefore, both processes can be conducted simultaneously, which is more common for SOEC systems [32]. The advantages of SOEC are efficiency, which is up to 100%, thermoneutral voltage, non-noble catalysts and high-pressure operations. Nevertheless, SOEC has its drawbacks, bulky system design and poor durability [33].

2.1 Hydrogen fuel cells (HFC)

The low amount of energy that can be obtained from burning hydrogen with oxygen into water molecules prevents it from being burned directly with oxygen. Therefore, in a similar process to electrochemical water splitting, hydrogen electrochemically must be reacted into water. In this way, energy production is higher. A hydrogen fuel cell (HFC) converts chemical energy stored in hydrogen into electrical energy, without harmful emissions. Fundamentally, HFC are composed of an anode, a cathode, and an electrolyte membrane. When hydrogen is supplied to the anode, it is split into positively charged hydrogen ions (protons) and negatively charged electrons. The protons are conducted through the electrolyte membrane to the cathode. The electrons travel through an external

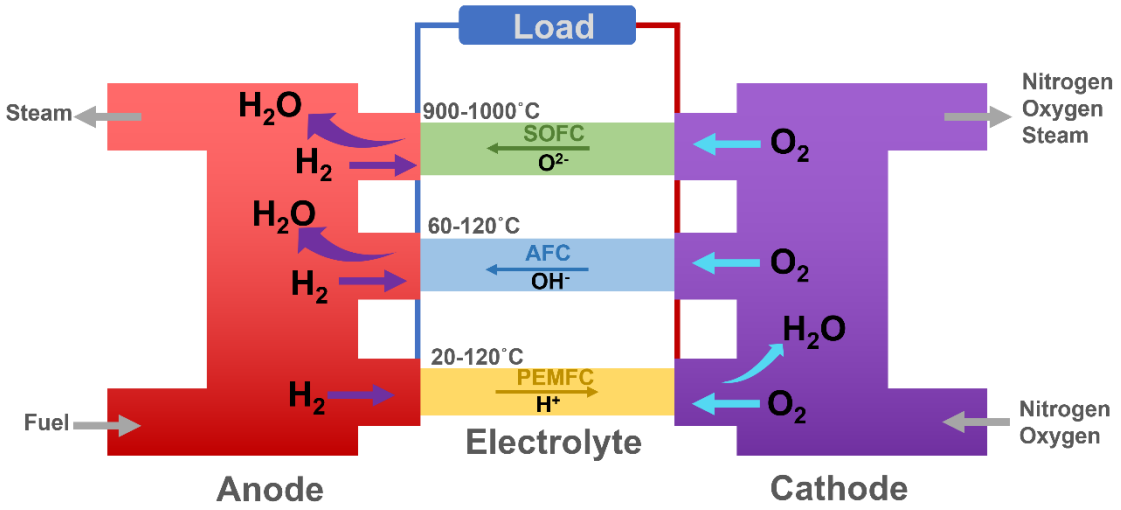

Figure 6. Hydrogen Fuel Cells (HFC) presenting three different types: proton exchange membrane fuel cells (PEMFC), alkaline fuel cells (AFC) and solid oxide fuel cells (SOFC).

circuit to the cathode, creating an electrical current that can power a device or charge a battery. At the cathode, protons and electrons combine with oxygen to produce water and heat as by-products. HFC have several advantages over conventional batteries and internal combustion engines, including higher efficiency, longer operating times, and zero harmful emissions. Hydrogen fuel cells can be divided into many types, which include proton exchange membrane fuel cells (PEMFC), solid oxide fuel cells (SOFC) and alkaline fuel cells (AFC). The principles of how they work are presented in Figure 6.

2.2.1 Proton exchange membrane fuel cells (PEMFC)

A proton exchange membrane fuel cell (PEMFC) is a type of fuel cell that uses hydrogen and oxygen from the air to produce electrical energy through an electrochemical

reaction. PEMFC have several advantages over other types of fuel cells, including high power density, low operating temperature, and quick start-up time. Hydrogen is supplied to the anode side of the fuel cell while air is supplied to the cathode. A proton exchange membrane, also called an electrolyte, is separating the two sides of a fuel cell. Hydrogen molecules split into protons and electrons on the anode. The protons travel through the electrolyte to the cathode, while electrons travel through an external circuit and produce electrical energy. On the cathode, protons and electrons combine with oxygen to form water, which is then released into the environment. PEMFC consists of several components, including a fuel cell stack, a proton exchange membrane, electrodes, and bipolar plates. The fuel cell stack consists of several individual fuel cells, each consisting of an anode and a cathode. The bipolar plates (BP) distribute the reactants to the electrodes and collect the fuel cell current. However, PEMFC faces several challenges, including the high cost of materials and the susceptibility of the catalysts to poisoning. Efforts are underway to address these challenges through the development of novel materials and catalysts [34]. The reactions on the anode and cathode are as follows:

$2H_2 \rightarrow 4H^+ + 4e^-$	anode
$O_2 + 4e^- + 4H^+ \rightarrow 2H_2O$	cathode
$2H_2 + O_2 \rightarrow 2H_2O$	total reaction

2.2.1 Alkaline fuel cells (AFC)

An alkaline fuel cell (AFC) is a type of fuel cell that uses alkaline electrolytes such as potassium hydroxide (KOH) or sodium hydroxide (NaOH) as the electrolyte. AFC has been in use for over half a century and is known for its high efficiency and long lifespan. AFC work on the same principle as other types of fuel cells, with hydrogen gas supplied to the anode and oxygen from the air supplied to the cathode. The alkaline electrolyte allows the flow of negatively charged hydroxide ions (OH^-) from the cathode to the anode. At the anode, hydrogen is oxidized, releasing electrons and protons. The electrons flow through an external circuit, producing electrical energy, while the protons combine with the hydroxide ions from the electrolyte to form water. AFC consists of several components, including an anode, a cathode and an alkaline electrolyte. The electrodes are coated with catalysts, such as platinum, which facilitate the electrochemical reaction. AFC faces several challenges, including materials cost and reliability of hydrogen source.

Efforts are underway to address these challenges through the development of new materials and the implementation of innovative solutions for hydrogen storage and distribution. Another challenge is the susceptibility of the electrodes to contamination and poisoning, which can reduce the fuel cell's efficiency over time [35]. The reactions on the electrodes are as follows:

$2H_2 + 4OH^- \rightarrow 4H_2O + 4e^-$	anode
$O_2 + 2H_2O + 4e^- \rightarrow 4OH^-$	cathode
$2H_2 + O_2 \rightarrow 2H_2O$	total reaction

2.2.3 Solid oxide fuel cells (SOFC)

Solid oxide fuel cells (SOFC) are a type of fuel cell that uses a solid oxide electrolyte to conduct ions between the anode and the cathode. They operate at high temperatures, typically between 700 and 1000°C, which allows them to use a range of fuels including hydrogen, methane, and biogas. SOFC are known for their high efficiency and potential and co-generation of electricity and heat. SOFC work on the principle of electrochemical reaction, similar to other types of fuel cells. The fuel, typically hydrogen or a hydrocarbon, is supplied to the anode side of the fuel cell, while oxygen is supplied to the cathode. The electrolyte in SOFC is a solid oxide material, which conducts oxygen ions (O^{2-}) from the cathode to the anode. At the anode, the fuel is oxidized, releasing electrons and protons. The electrons flow through an external circuit, producing electrical energy, while the protons travel through the electrolyte to the cathode, where they react with oxygen to form water. The electrodes are coated with catalysts, such as nickel or platinum, which facilitate the electrochemical reaction. SOFC face several challenges, including the high operating temperature, which can lead to thermal stress and mechanical failure. They also require expensive materials, such as rare metals, and can be sensitive to impurities in the fuel. However, research is ongoing to address these challenges, including the development of new materials and the optimization of the fuel cell design [36]. Reactions occurring on the electrodes are as follows:

$2H_2 + 2O^{2-} \rightarrow 2H_2O + 4e^-$	anode
$O_2 + 4e^- \rightarrow 2O^{2-}$	cathode
$2H_2 + O_2 \rightarrow 2H_2O$	total reaction

3. Hydrogen Evolution Reaction (HER)

Hydrogen evolution reaction (HER) as one of the half-reactions for overall water splitting is one of the most interesting due to the production of hydrogen. The most efficient electrocatalyst generates hydrogen by electrolysis. In a matter of just hydrogen evolution, we can use any conductive material as a cathode for HER. However, the excess electricity we will have to use (also called overpotential) will be enormous. Furthermore, the electrocatalyst will corrode to collapse and fail to produce hydrogen. Therefore, the challenge is to design and manufacture a catalyst which will allow long and cheap hydrogen production. The electrocatalyst as the name indicates affects the activation energy in an electrochemical reaction – a function of voltage at which the reaction occurs

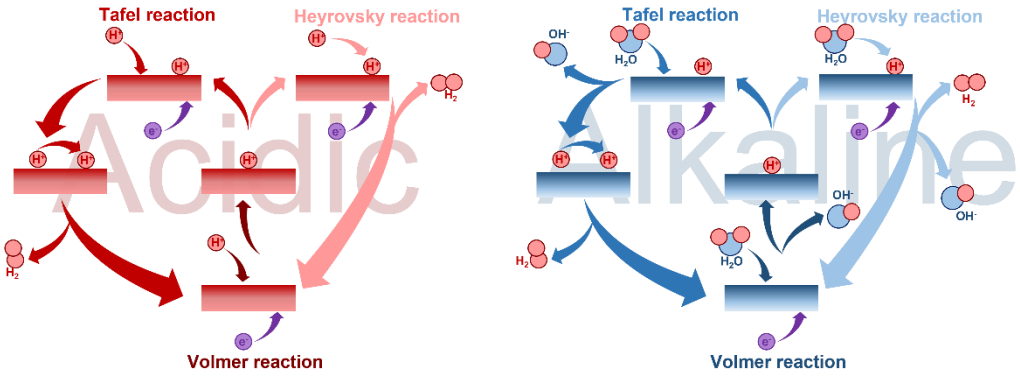

Figure 7. Graphical representation of HER mechanism in acidic and alkaline conditions.

leads to the electrocatalyst changing REDOX potential at the electrode-electrolyte interface. According to their properties, HER catalysts are selected by three criteria: activity, stability and selectivity [37]. Moreover, the electrocatalyst utilised for HER can be divided into three main categories: 1) noble-metal based, 2) non-noble metal based and 3) non-metal based. The process of hydrogen evolution in an alkaline medium can be explained by many theories, i) water dissociation theory, ii) hydrogen biding energy (HBE) theory, iii) interface water and/or anion transfer theory, where water dissociation or hydrogen adsorption are the key elements of HER kinetics [38]. Figure 7 represents the adsorption of hydrogen on the catalyst surface in acidic and alkaline conditions.

The first step in acidic conditions is a process of proton (H^+) adsorption on the active site of the catalyst surface (M), by binding to the electron and forming intermediate species on the surface (MH_{ads}). Volmer step:

$$H^+ + M + e^- \rightarrow MH_{ads}.$$

Therefore, H_{ads} attaches to an additional proton and acquires an electron to form a hydrogen molecule, which is also called the Heyrovsky reaction. Additionally, H_{ads} reacts with adjacent H_{ads} to form hydrogen molecules, a mechanism known as the Tafel reaction. The chemical equations for these steps are presented below:

$$MH_{ads} + H^+ + e^- \rightarrow M + H_2, \qquad \text{Heyrovsky step;}$$

$$2MH_{ads} \rightarrow 2M + H_2, \qquad \text{Tafel step.}$$

Moreover, the adsorption-free energy for hydrogen in Volmer-Heyrovsky and Volmer-Tafel is a useful indicator of hydrogen evolution and matches nearly zero. As a result, HER has a very high catalytic activity. Nevertheless, the alkaline process is also possible, despite no free protons in the electrolyte and two to three orders of magnitude slower than that in acid environments. Therefore, the process starts with the dissociation of water molecules on the catalyst's active surface.

$$H_2O + M + e^- \rightarrow MH_{ads} + OH^-$$

Consequently, the formation of hydrogen molecules can occur through the merging of H_{ads} with water molecules or by combining H_{ads} with other H_{ads} (Tafel reaction). This implies that the rate of the hydrogen evolution reaction is sluggish in alkaline environments. Thus, it is crucial to maintain a balance between desirable energy for the

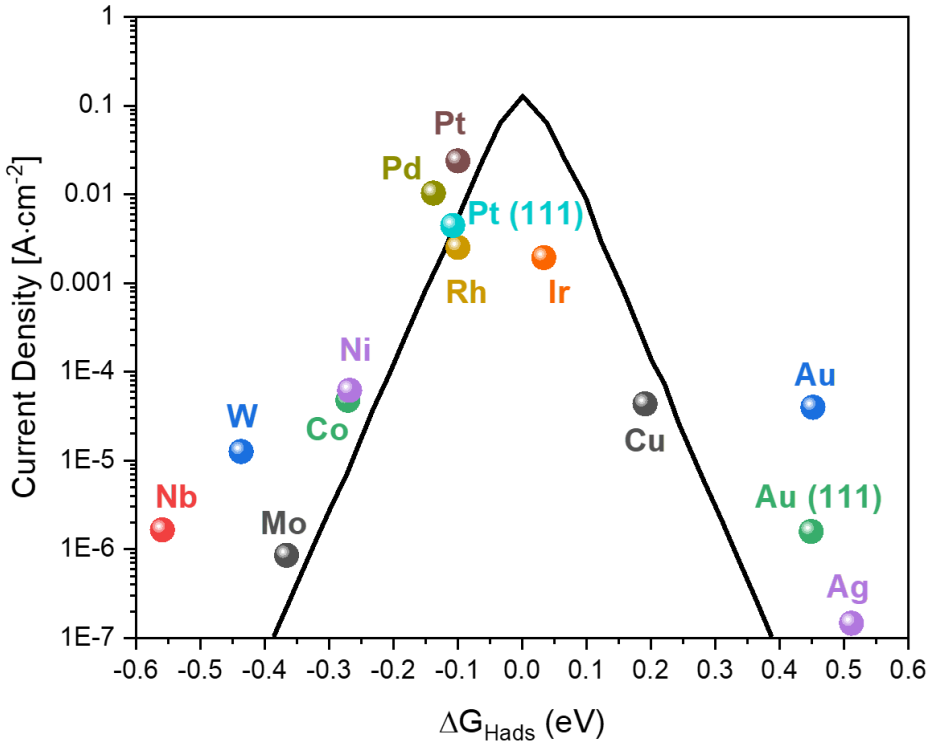

Figure 8. Volcano plot of the catalysts for HER.

dissociation of water and reasonable energy for the adsorption of hydrogen. The Heyrovsky reaction is as follows:

$$MH_{ads} + H_2O + e^- \rightarrow M + OH^- + H_2$$

In summary, electrocatalyst improvement can be achieved by improving the bonding energy between catalytic electricity and reaction intermediates [16,38]. Therefore, connecting the kinetics of the HER with its thermodynamics, which is well described on the volcano plot (Figure 8) presents the electrocatalyst on the current density vs. free energy Gibbs for hydrogen adsorption (ΔG_{Hads}). Catalysts inside the "volcano" are thermodynamically promising materials, whereas the energy of the catalyst is neither too high nor too low to bind hydrogen. Thus, the best way to predict HER's excellent electrocatalyst is to use its kinetics and thermodynamics.

3.1 HER catalysts based on noble metals

3.1.1 Platinum-based catalysts

Platinum (Pt) exhibits the highest HER activity due to its thermodynamic properties towards hydrogen as can be seen on the volcano plot. The Pt-based catalyst, however, does not show good stability in corrosive electrolytes. Additionally, platinum is an expensive CRM material. The main route to reduce Pt catalyst costs catalyst is to reduce its loading without losing efficiency. Platinum nanoparticles (NP) combined with carbon support are one of the most promising approaches to HER. Additionally, carbon-Pt composites enhance the electrical conductivity allowing fast electron transfer, thus improving HER kinetics [39]. The other way to improve Pt electrocatalytic performance is alloying, where Pt is added to other metals or other metals are added to Pt-NP [38].

Platinum NP can be combined with sophisticated carbon structures, such as single-walled carbon nanotubes (SWCNT). Hu et al. [40] have presented a facile way to introduce platinum into SWCNT doped with cobalt (Co) by adding acetylacetonate salts – $Pt(acac)_2$ and $Co(acac)_3$ and treating it with acid. A variety of ratios of the Pt-Co electrocatalyst have been investigated by the group. As a result, the most optimal composition of 90% Pt and 10% of Co inside SWCNT was similar to commercial Pt/C with significantly lower mass loading. This resulted in reduced costs.

As the other way to reduce the costs of Pt-based catalysts is alloying, Zhou et al. [41] have presented the silver-nanowire-based support which was modified with nickel (Ni) – NiO/Ni. Nickel then was used as a platform to introduce single atoms of Pt to synthesis

the single-atom catalyst (SAC). Such structure allowed for efficient HER in an alkaline medium. In their studies, they show that NiO/Ni interface presented a preferred affinity towards both OH_{ads} and H_{ads}. It led to barrier-free water dissociation on the catalyst surface. The platinum thus effectively promoted H_{ads} conversion and H_2 desorption.

3.1.2 Ruthenium-based catalysts

Ruthenium (Ru) as a cheaper alternative for Pt with similar metal-hydrogen bond strength (~65 kcal×mol^{-1}) show an interesting alternative for platinum as a catalyst in HER [39].

Yang at al. [42] have overcome the challenges of transition metal phosphides (TMP) by introducing to Cu@Cu_3P interface Ru-SAC. It was reported that a new type of HER catalyst was synthesized, consisting of Ru-single-atomic sites (SA) with Cu_3P nanoparticles supported on chemically converted graphene (Cu@Cu3P-Ru/CCG). Investigated structures shoved an average diameter of the Cu@Cu3P-Ru/CCG-500 nanoparticles equal to 2 nm. Density functional theory (DFT) calculations revealed that the Ru-SA on Cu_3P facilitated H_2O dissociation, while the Ru-SA on CCG promoted the formation of hydrogen from H_{ads}.

Zhu et al. [43] have demonstrated that the well-dispersed ruthenium-based clusters with adjacent Ru-SA on layered sodium cobalt oxide (Ru/NC) are an excellent electrocatalyst for alkaline HER. According to the study, the Ru/NC catalyst showed a two-fold increase in activity compared to the commercial Pt/C. The researchers utilized operando characterizations in conjunction with DFT simulations to establish a structure-performance relationship and uncover the origin of the superior activity. They found that under HER conditions, the real active species are Ru-SA and metallic Ru clusters supported on the NC substrate. The study revealed that the excellent alkaline HER activity of the Ru/NC catalyst can be attributed to a spatially decoupled water dissociation and hydrogen desorption mechanism. The NC substrate accelerates the water dissociation rate, and the generated H intermediates migrate to the Ru-SA or clusters and recombine to form H_2, resulting in high catalytic activity. Moreover, the researchers discovered that the Ru cluster plays a dominant role in the HER activity when compared to the Ru-SA.

3.1.3 Iridium-based catalyst

Iridium (Ir) has emerged as a promising catalyst for the hydrogen evolution reaction due to its weak hydrogen binding energy, which allows hydrogen atoms to readily bind

and unbind to the Ir surface, a crucial aspect of the HER mechanism. In addition, Ir has demonstrated remarkably high thermal stability and a balanced capacity for hydrogen adsorption and desorption. Moreover, Ir's position near the top of the HER volcano plot, which represents the catalytic activity of various materials for HER, suggests its excellent potential as a viable alternative to Pt for HER. Therefore, there is increasing interest in exploring Ir-based catalysts for HER and understanding their catalytic mechanisms to develop highly efficient and sustainable energy conversion technologies [39,44].

The novel 10 %wt Ir/$W_{18}O_{49}$ nanowire catalyst for enhancing the performance of HER under a neutral medium was developed by Peng et al. [45]. The $W_{18}O_{49}$ support enhances electron transfer capability and promotes the dissociation of water molecules, leading to improved performance. The catalyst exhibits low overpotential and low Tafel slope under neutral conditions. The use of tungsten oxide as a support material is shown to have significant effects on the performance of neutral HER. In addition, the tungsten oxide support showed a unique property of serving as a "proton container" by releasing protons at the start of the reaction. This property facilitates the hydrogen evolution reaction through an acidic pathway and leads to enhanced performance.

In their study, Geng et al. [46] grew hexagonal close-packed (hcp) Ir onto Ni using spherical aberration electron microscopy. The resulting hcp Ir had high activity for the alkaline HER, with a low overpotential, high specific activity and a high turnover frequency. The epitaxially grown structure of the hcp Ir also made it highly stable. Theoretical calculations showed that the hcp Ir promoted fast water adsorption and dissociation, contributing to its remarkable HER activity. These findings can inform the development of noble metal nanomaterials with specific crystal phases for catalytic applications.

3.2 HER catalysts based on non-noble metals

Noble metal-based electrocatalysts offer high performance for HER, but are also expensive and require advanced composites and structures. Therefore, non-noble metals are an attractive alternative due to their low costs, accessibility and excellent electrocatalysis performance [47]. Non-noble transition metals like iron (Fe), cobalt (Co), nickel (Ni), copper (Cu), molybdenum (Mo), and tungsten (W) have been used to create catalysts for HER. According to voltammetric techniques, Ni had superior performance, followed by Mo, Co, W, Fe, and Cu accordingly. Metallic nickel is considered the most effective electrocatalyst for HER in alkaline conditions, similar to metallic Co-based

catalysts, which have also been explored for HER electrolysis. Non-noble metal electrocatalysts made from earth-abundant metals offer promising alternatives to noble-metal-based ones. However, these electrocatalysts can corrode in strongly acidic or alkaline environments and can form larger particles during catalytic cycling [48].

3.2.1 Nickel-based catalyst

The use of Pt-based electrocatalysts for the hydrogen evolution reaction is still necessary, despite their high cost and limited availability. As a result, nickel-based materials are being explored as alternative - earth-abundant HER electrocatalysts. Advanced nickel-based catalysts have been developed through various synthesis strategies, such as controlling their shape, modifying their structure, and engineering their interfaces, resulting in significantly improved HER performance [49].

During the process of hydrogen evolution reaction, low-cost catalysts such as dichalcogenides and their single-atom modified analogues have great potential for electrocatalyst application. Pattengale et al. [50] synthesized the Ni-based SAC on molybdenum disulphide (MoS_2) and through in situ X-ray absorption spectroscopy (XAS), have been able to observe the intermediate structure of the Ni active site during catalytic conditions. During catalysis in an acidic electrolyte, the active site structure of the Ni centre remains the same intrinsically but undergoes a net reduction in its oxidation state. On the other hand, in an alkaline electrolyte, coordination changes occur as a result of immersion in the electrolyte, forming NiS_xO_y species. Upon applying a catalytic potential, a metallic Ni species is reversibly formed as the active site. Therefore, Ni-SA shows a high-performance rate in HER.

3.2.2 Cobalt-based catalyst

Cobalt (Co) is attractive as HER catalyst for several reasons. It is an earth-abundant metal, which makes it a low-cost alternative to expensive noble metals like platinum. Secondly, cobalt has good stability and durability under harsh reaction conditions, such as high temperatures and acidic or alkaline environments, making it a reliable choice for practical applications. New electrocatalysts are mostly based on advanced architecture like single-atom-based (SA).

Liu et al. [51] presented their work on Co-SA electrocatalysts for HER. As a support for a catalyst their synthesized graphitic carbon nitride (g-C_3N_4) on graphene oxide. Such structure presented electrochemical properties similar to Pt/C with much higher

durability. Co-N plays a role of a catalyst while GO supported the electrical conductivity. Therefore, advanced architecture allowed for high performance and durable HER, especially showing that non-noble catalysts can compete with platinum.

3.3. HER catalyst based on non-metallic catalysts

Non-metallic catalysts play a crucial role in the hydrogen evolution reaction (HER) by providing an alternative to precious metal catalysts such as platinum. Non-metallic catalysts are typically low-cost, abundant, and exhibit high catalytic activity and stability under certain conditions. Examples of non-metallic HER catalysts include metal-free carbon materials, metal-free nitride materials, metal-free sulphide materials, and metal-free phosphide materials. These catalysts often have unique surface chemistry and electronic properties that make them attractive alternatives to traditional metal-based catalysts. Non-metallic catalysts can also be modified with different functional groups to further enhance their HER activity and selectivity. Overall, the development of non-metal-based HER catalysts has the potential to significantly reduce hydrogen production costs and make hydrogen a more accessible energy carrier [52–54].

4. Oxygen Evolution Reaction (OER) as a critical step in water splitting

Oxygen evolution reaction (OER) is the second half-reaction of electrochemical water splitting. In this reaction, multiple intermediates are produced by the four-step electron transfer.

4.1 Adsorbate evolution mechanism

Adsorbate evolution mechanism (dcp) in acid medium:

$$2H_2O + M \rightarrow MOH_{ads} + H^+ + H_2O + e^-$$

Firstly, the water molecule is adsorbed on the active site of the catalyst (M). Then it breaks down into hydroxide groups adsorbed on the catalysts (MOH_{ads}) and hydrogen ion (H^+) and electron (e^-).

$$MOH_{ads} + H_2O \rightarrow MO_{ads} + H^+ + H_2O + e^-$$

Then, the adsorbed hydroxyl group react with a water molecule to form an adsorbed oxygen on the catalyst surface (MO_{ads}) and H^+ with an electron.

$$MO_{ads} + H_2O \rightarrow MOOH_{ads} + H^+ + e^-$$

Adsorbed oxygen combines further with water molecules to form $MOOH_{ads}$, H^+ and electrons.

$$MOOH_{ads} \rightarrow M + O_2 + H^+ + e^-$$

Finally, it generates oxygen by OOH_{ads} decomposition. In basic/neutral electrolytes, the OH^- ions are the starting reactants and the reaction is as follows [16]:

$$4OH^- + M \rightarrow MOH_{ads} + 3OH^- + e^-$$
$$MOH_{ads} + 3OH^- \rightarrow MO_{ads} + 2OH^- + H_2O + e^-$$
$$MO_{ads} + 2OH^- + H_2O \rightarrow MOOH_{ads} + OH^- + H_2O + e^-$$
$$MOOH_{ads} + OH^- + H_2O \rightarrow M + O_2 + H_2O + e^-$$

The OER process involves four uphill reactions that produce intermediates of MOH_{ads}, MO_{ads}, and $MOOH_{ads}$ at each step. The highest energy step is the speed-limiting step and determines electrode materials' catalytic activity. The energy barriers of each reaction are related and follow a proportional relationship. The energy required for the $MOH_{ads} \rightarrow MO_{ads}$ and $MO_{ads} \rightarrow MOOH_{ads}$ steps is approximately the same at 3.2 eV. The total free energy change for OER is 4.92 eV. It can be evenly distributed among the four basic steps with different adsorbents. Metal oxide catalysts have a fixed adsorption-free energy of 3.2 eV between MOH_{ads} and $MOOH_{ads}$. The ideal position for MO_{ads} is in the middle of the volcano map to reduce the variation of free energy as much as possible

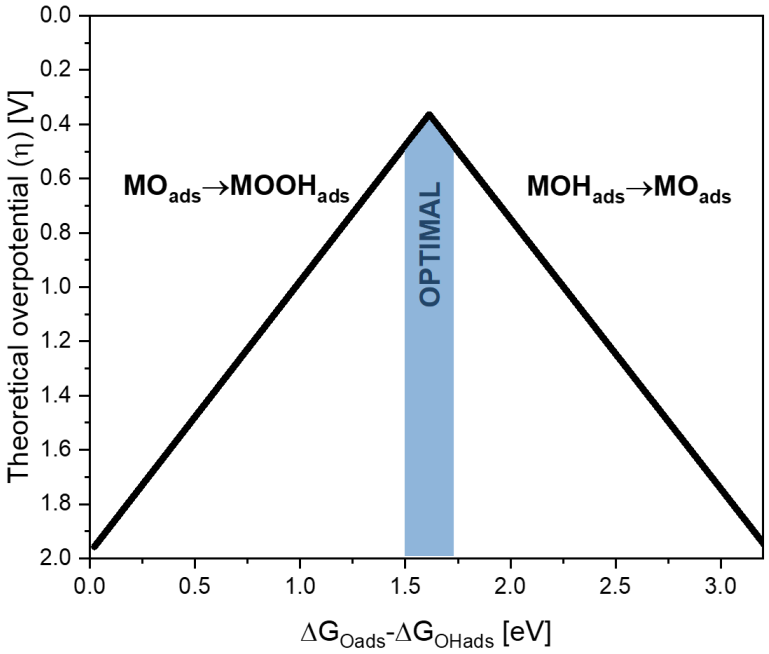

Figure 9. The volcano plot represents the overpotential concerning the adsorption energy of O_{ads} and OH_{ads}. The highlighted area is the optimal value for OER between OH_{ads} and OOH_{ads}.

according to the Sabatier principle [16,55]. The volcano plot showing this relation [56] is presented in Figure 9.

4.2 Lattice oxygen mechanism

Progress in OER mechanism studies indicates that not all processes can be explained via AdEM. It seems that some of the recently discovered novel materials do not fit the volcano theory. It was found that lattice oxygen (O_L) present in catalysts can directly participate in OER. As an example, the activation process of $IrNiO_x$ catalysts involves the leaching of Ni. This leads to the formation of vacancies in the Ir lattice. Moreover, this leaching process results in the shortening of Ir-O bonds and the creation of numerous d-band voids within the IrO_x shell. These structural changes contribute to an increase in oxygen ligand electrophilicity [57]. This mechanism, known as the lattice oxygen mechanism (LOM), differs from the AdEM. Density Functional Theory (DFT) calculations indicate that surface oxygen ligands (O_L) can participate in the OER by generating reversible oxygen vacancies (V_O) [55]. This pathway can be described using the following reactions:

$$M + H_2O \rightarrow MOH_{ads} + H^+ + e^-$$
$$MOH_{ads} \rightarrow MO_{ads} + H^+ + e^-$$
$$MO_{ads} + O_L \rightarrow O_2 + M + V_O$$
$$V_O + H_2O \rightarrow MH_{ads} + H^+ + e^-$$
$$MH_{ads} \rightarrow M + H^+ + e^-$$

In contrast to the AdEM, the LOM proposes that a portion of the O_2 molecules originate from surface oxygen ligands (O_L), and direct coupling of oxygen atoms without the formation of $MOOH_{ads}$ intermediates is a crucial step. The initial two steps resemble those in the AdEM mechanism. In the third step, the adsorbed MO_{ads} species react with O_L, resulting in the release of an O_2 molecule and the formation of surface oxygen vacancies (V_O). A neighbouring oxygen atom from a water molecule replaces the V_O site, generating an adsorbed MH_{ads} species. Finally, the adsorbed MH_{ads} species are removed, creating new active sites [55].

4.3 Catalysts in oxygen evolution reaction

In general, the catalyst for OER can be similarly distributed into three main categories: 1) noble metals, 2) transition metals and 3) non-metallic catalysts.

4.3.1 OER catalysts based on noble metals

Currently, noble metals, including rare earth metals, their oxides, alloys, and composites, have gained significant attention as highly effective catalysts for OER due to their remarkable activity. Among these noble metals, ruthenium (Ru) and iridium (Ir) exhibit great potential as candidates for OER, surpassing the reactivity of palladium (Pd), rhodium (Rh), and platinum (Pt) in the order Pt < Rh < Pd < Ir < Ru. This reactivity trend is also reflected in the overpotential required for these materials. However, the stability of noble metals in acidic media demonstrates the opposite trend. Extensive comparative studies have been conducted to evaluate the intrinsic catalytic response and durability of Pt, Ru, and Ir nanoparticles, as well as their corresponding bulk materials. Experimental data reveal that the intrinsic OER activity of metal nanoparticles follows the order: Ru > Ir > Pt. Noble metal oxides are highly regarded as advanced materials due to their exceptional catalytic activity and stability in both acidic and basic environments. Both RuO_2 and IrO_2 exhibit a rutile structure, with the metal positioned at the centre of an octahedron and oxygen at the corners [58].

4.3.2 OER catalysts based on non-noble metals

The non-noble metals are attractive due to their low costs and accessibility. Among them, two show the highest potential for OER electrocatalysts: nickel (Ni) and cobalt (Co).

Nickel is widely used in various applications due to its corrosion resistance and malleability. In the context of water oxidation, the utilization of Ni-based compounds was initially explored by Bode et al. [59], and since then, nickel-based oxides, hydroxides, perovskites, and mixed metal oxides have been frequently employed for water splitting. Ni higher oxidation state (Ni^{3+}) is more efficient towards OER, which can be promoted via metal doping with titan (Ti), iron (Fe) or Co. Recent years of research have revealed the reactivity order of transition metal oxides/hydroxides in alkaline conditions, with nickel exhibiting higher activity compared to cobalt, iron, and manganese [58].

Cobalt has gained significant attention as a remarkable non-noble metal catalyst for OER in alkaline conditions. This is attributed to its outstanding catalytic activity, excellent stability, distinctive 3d electronic configuration, and ability to adopt multiple oxidation states. Furthermore, the phase transformation of cobalt-containing materials, such as the transition from M−O to M−OH or M−OOH, during the OER process is widely

acknowledged to play a crucial role in its catalytic performance. To improve the activity of Co-based catalysts, in cobalt oxides oxygen vacancies can be developed. Moreover, the most active cobalt ion is Co^{2+}, which can be transformed into CoOOH during OER. Another way to boost the catalytic performance is atom doping, where onset overpotential can be significantly lowered [58].

However, for both elements, durability is still challenging, however, some efforts have been made through design and advanced architecture to overcome these obstacles [58].

4.3.3 OER catalyst based on non-metallic catalysts

In terms of their tuneability, low costs, and high surface area, carbon (C) based materials are the most promising electrocatalysts for oxygen evolution reactions. To increase carbon electrochemical properties, the common practice is elemental doping. Nitrogen (N) is the most commonly used dopant in carbon lattices, as it improves their electronic and electric properties. Nitrogen position in carbon, depending primarily on pyridinic or quaternary sites, is critical and responsible for the electrochemical activity. It is possible to do multielement doping to further develop the C-based electrocatalyst. The most popular and efficient dual-element dopants are nitrogen-phosphorus (N/P) and nitrogen-sulfur (N/S) [60,61].

Chapter III: Metal-Organic Framework Structures, Modifications and Application in OER

1. Introduction to MOF

Metal-organic frameworks (MOF) are a class of porous materials composed of metal ions or clusters coordinated with organic ligands. They are crystalline structures with a highly ordered network of metal nodes interconnected by organic linkers. MOF have an intricate structure that combines the properties of both metals and organic compounds, resulting in a wide range of applications. MOF have attracted significant attention in various fields due to their tuneable porosity, high surface area, and diverse chemical functionalities. Their porous nature allows gas storage and separation, including hydrogen and carbon dioxide. Additionally, MOF has applications in catalysis, drug delivery, sensing, and environmental remediation. Precise control over MOF composition and structure enables tailored materials design. By selecting specific metal ions and ligands, MOF's pore size, surface chemistry, and functionality can be customized for targeted applications. This versatility makes MOF promising candidates for addressing challenges in energy storage, gas purification, and sustainable chemistry [62].

Figure 10. Three different MOF structures: cubes (MOF-5), rhombic dodecahedrons (ZIF-67) and hexagon rods (In-MOF).

There are various types of MOF based on different metal ions, organic ligands, and structural features. Three different MOF structures are presented in Figure 10. Some commonly recognized types of MOF include:

- Zirconium-based MOF: Zirconium is a commonly used metal in MOF, known for its stability and high connectivity. Zirconium-based MOF, such as UiO-66 and MOF-808, have been widely studied for gas storage, catalysis, and drug delivery applications [63].

- Copper-based MOF: Copper ions form stable coordination bonds with organic ligands, leading to robust MOF structures. Examples include HKUST-1 ($Cu_3(BTC)_2$) and Cu-BTC ($Cu_3(BTC)_2(H_2O)_3$), which have shown potential for gas storage, catalysis, and sensing [64].
- Iron-based MOF: Iron-based MOF, such as MIL-88 (Fe), MIL-100 (Fe), and Fe-BTC (MOF-235), exhibit high stability and tuneable porosity. They have been explored for applications in gas separation, catalysis, and drug delivery [65,66].
- Aluminium-based MOF: Aluminium-based MOF, such as Al-MIL-53, MIL-125 (Al), MIL-100(Al) and MIL-101(Al) are known for their flexibility and structural transitions. These MOF have been studied for gas adsorption, sensing, and drug delivery applications [67,68].
- Lanthanide-based MOF: Lanthanide ions, such as cerium (Ce), terbium (Tb), and europium (Eu), have been incorporated into MOF to achieve luminescent properties. Lanthanide-based MOF have potential applications in sensing, imaging, and optoelectronics [69].
- Mixed-metal MOF: These MOF contain more than one type of metal ion in their structure. Mixing different metal ions allows for different properties and enhanced functionalities. Examples include mixed Zr/Al-MIL-53 and combined Cu/Zn-MOF

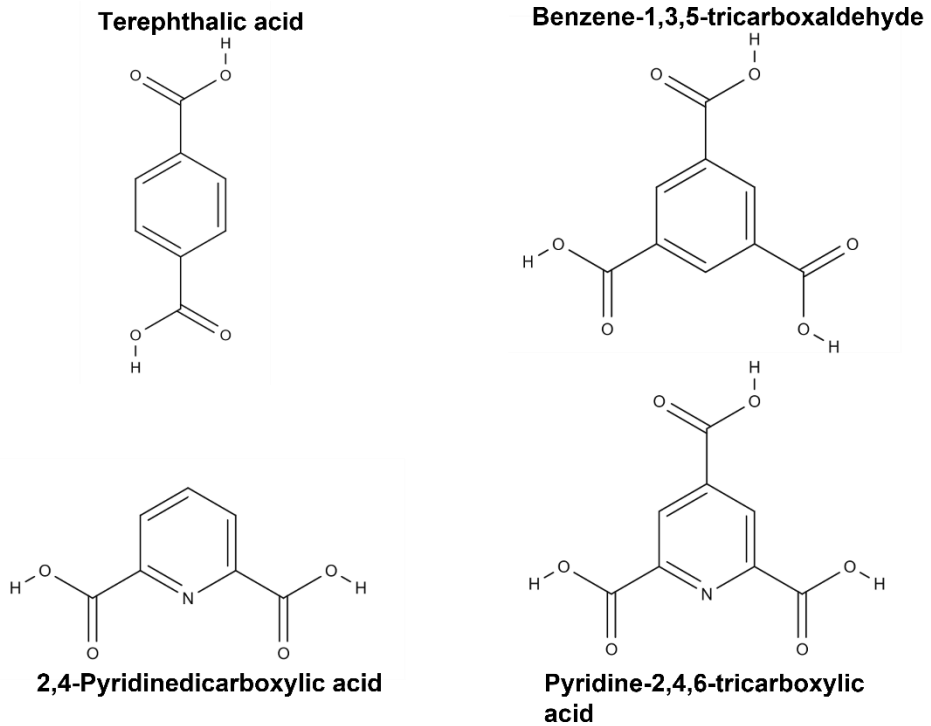

Figure 11. Examples of organic linkers commonly used in MOF synthesis. Two organic linkers are with one atom of nitrogen (pyridine).

[70,71].

MOF synthesis typically involves the reaction of metal-containing precursors with organic ligands in a solvent under specific conditions of temperature, pressure, and time. The metal-containing precursors can be inorganic salts or metal-organic compounds, and the organic ligands can be a variety of organic molecules such as carboxylic acids, amines, and pyridines (Figure 11). The solvent used can be polar or nonpolar, depending on the specific MOF being synthesized. The reaction conditions control the size, shape, and composition of the resulting MOF crystals. For example, temperature and pressure can affect the nucleation and growth of crystals. In addition, the choice of solvent can influence the solubility and reactivity of precursors and ligands [62]. Various synthesis methods have been developed (Figure 12):

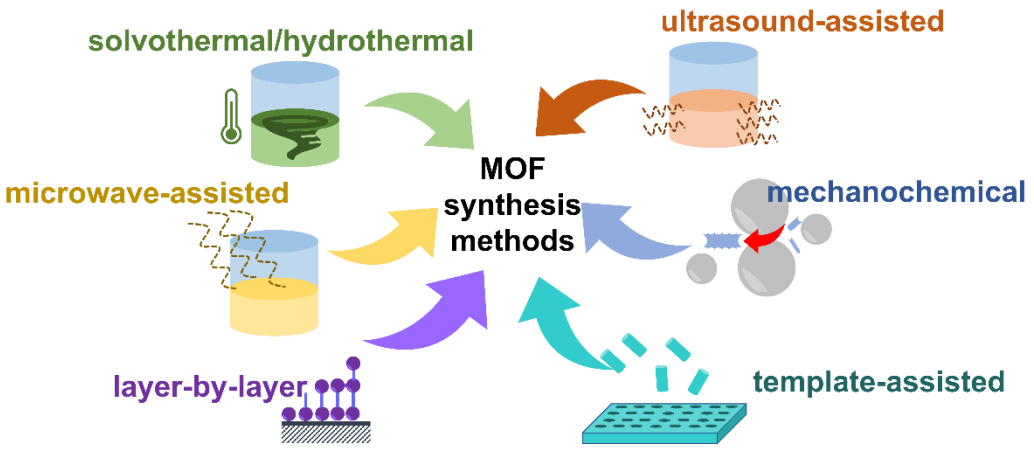

Figure 12. Scheme of MOF synthesis methods.

- Solvothermal or hydrothermal synthesis: This method involves the reaction of metal precursors and organic ligands in a solvent under high temperature and high-pressure conditions. The choice of solvent and reaction conditions can influence the size, shape, and properties of the resulting MOF [72,73].
- Microwave-assisted synthesis: In this approach, the reaction mixture containing metal precursors and organic ligands is subjected to microwave irradiation. Microwaves can accelerate synthesis and promote MOF formation [74].
- Ultrasound-assisted synthesis: Ultrasonic waves are applied to the reaction mixture to facilitate the mixing of metal precursors and ligands, leading to faster and more uniform MOF formation [75].
- Mechanochemical synthesis: This method involves the grinding or milling of solid metal precursors with organic ligands without or in the presence of a solvent. The mechanical force applied during grinding promotes MOF formation [76].

- Layer-by-layer (LbL) assembly: In this approach, alternating layers of metal precursors and organic ligands are sequentially deposited on a substrate. The layers react to form a crystalline MOF film [77].
- Template-directed synthesis: Templates such as nanoparticles or micelles guide MOF formation and growth. The templates can be removed after MOF synthesis, leaving behind the desired porous structure [78].

2. Synthesis of aluminium-based MOF

Aluminium (Al) based metal-organic frameworks (MOF) are a unique category of MOF due to their excellent thermal stability and chemical resistance. Moreover, like other MOF they exhibit large surface area and high pore volume. This allows for efficient adsorption in various applications, such as gas sorption or electrochemical processes, like energy storage or electrocatalysis. Al-MOF presents high tunability properties, making them suitable for different metal incorporation (catalysts) or modifying organic linkers, e.g. to provide other atoms like nitrogen by pyridine-based organic linkers. Additionally, Al-MOF is sustainable and eco-friendly due to the presence of aluminium in the earth's crust. Therefore, many aluminium-based MOF have been developed, such as MIL-100(Al) or MIL-101(Al). Typical MOF structures were presented in Figure 13.

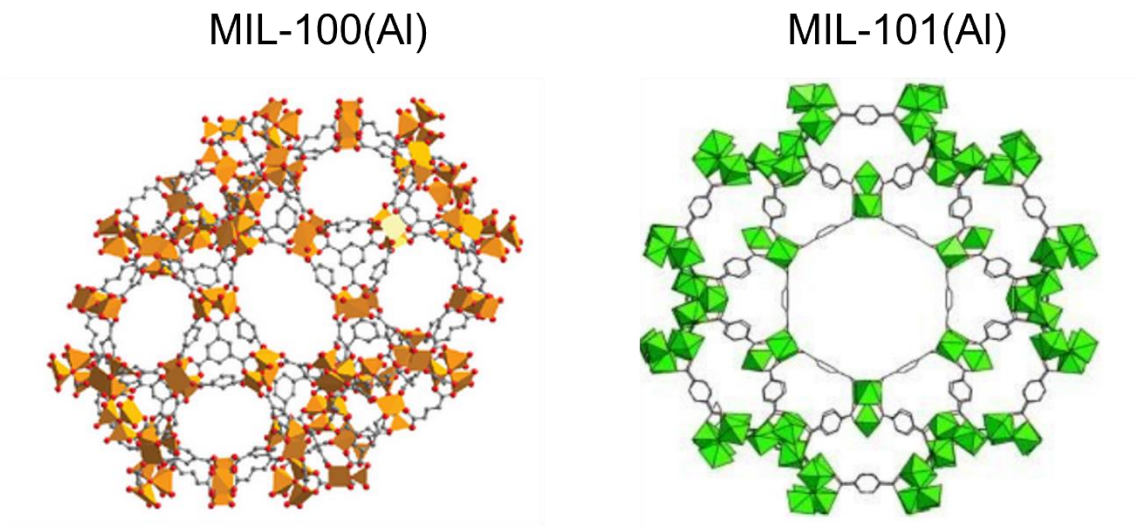

Figure 13. Scheme representation of MIL-100(Al) and MIL-101(Al) [101,102].

Depending on the type of organic linker and synthesis methods, the possible MOF structures that can be synthesised are almost limitless. Nevertheless, the most popular method for MOF synthesis is solvothermal. In this method, instead of water

(hydrothermal) other mediums are used, such as dimethylformamide (DMF). The method is based on the self-assembling of metal ions and organic linkers at high temperatures. Therefore, when using an organic linker with 2 carboxylic groups (H_2BDC) we can synthesise MIL-101(Al) and when using an organic linker with 3 carboxylic groups (H_2BTC) it is possible to synthesise MIL-100(Al) [67,79]. In the synthesis stage we can introduce some other atoms into the structure in two ways: 1) use the organic linker with nitrogen or phosphorus or 2) add other metal ions to the reaction mixture. However, MOF structure is easy to modify by synthesis parameters and substrates. Therefore, changing pH, changing solvent, changing temperature, changing the time of the process, adding other metals or changing the organic linkers significantly impacts the final structure (Figure 14).

Altering the pH during the synthesis or post-synthetic modification of aluminium-based MOF can influence the nucleation, crystal growth, and stability of the frameworks. Varying pH can affect the coordination environment around the aluminium nodes, leading to changes in the MOF's structure, pore size, and surface area. PH-dependent protonation or deprotonation reactions may also impact the charge distribution within the MOF, altering its electrochemical and catalytic properties [67,80,81].

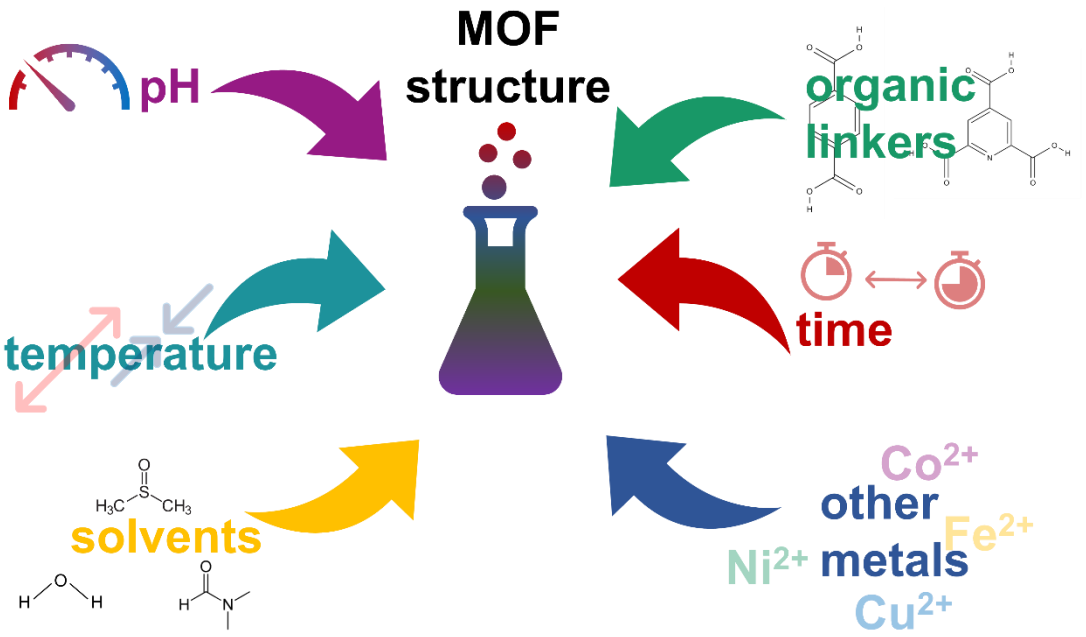

Figure 14. Schematic representation of synthesis parameters that impact MOF structure.

The choice of solvent or solvent mixture can significantly impact aluminium-based MOF formation, crystallinity, and morphology. Different solvents interact differently with metal ions and organic linkers, affecting their coordination and self-assembly processes.

Solvent polarity and coordination ability influence MOF surface area, pore size, and guest molecule uptake capacity. Additionally, solvent selection can impact the reaction kinetics and the removal of residual solvents during the synthesis, thereby affecting the final properties of the MOF [81,82]. Temperature plays a critical role in MOF synthesis and post-synthesis processes. Varying temperatures can influence the kinetics of crystal growth, nucleation, and framework stability. Temperature changes can impact MOF porosity, crystal size, surface area, and thermal stability. It can also affect the adsorption/desorption behaviour of guest molecules and MOF ability to accommodate functional groups or additional metals within its structure [81]. The reaction time during MOF synthesis or post-synthetic modification can directly impact the degree of crystallinity, phase purity, and morphological characteristics of aluminium-based MOF. Longer reaction times generally lead to larger crystals with enhanced crystallinity. However, excessively prolonged reaction times can also result in impurities or unwanted secondary phases. Optimizing reaction time is crucial to well-defined MOF structures with desirable properties [83]. Introducing other metals into aluminium-based MOF or altering the organic linkers can significantly impact their structural, electronic, and catalytic properties. The addition of different metal nodes can lead to a mixed-metal MOF, influencing framework stability, redox properties, and catalytic activity [84]. Changing the organic linkers can affect the connectivity, topology, and porosity of the MOF structure. This can lead to modified adsorption capacities, selectivity, or guest-host interactions [67].

3. MOF-based structures as catalysts for oxygen evolution reaction

MOF-based structures which are designed for specific applications, such as electrocatalysts for OER can be divided into two categories: 1) MOF, as a metal-organic structure and 2) carbonized MOF (CMOF) as a carbon structure with metal residues from MOF.

3.1 MOF for OER

There are several strategies for utilizing MOF in oxygen evolution reactions The use of a co-catalyst in MOF structures is one of the strategies. Li et al. [85] synthesized an electronic structure by building up Co-BDC and Fe-BDC, two MOF structures that were built simultaneously in one reactor. Next, the structure was treated with ultrasounds to maximize charge transfer possibility. This approach allowed for an increase in

electrochemical performance compared to the mechanical mixing of both MOF structures. The overpotential of such a structure was advantageous to ruthenium oxide (RuO_2) and reached η= 295 mV. Moreover, the electrocatalyst show good stability and started increasing the required potential for OER after 7 h of polarization. However, after long cycling, the structure of the MOF remains. Another example of a co-catalyst is presented by Wang et al. [86]. They synthesized bimetallic FeNi-MOF nanoarrays which show self-optimizing properties during OER via gradual valance increments of iron ions in MOF. Such improvement resulted in low overpotential η= 239 mV and excellent durability for more than 43 days of polarization at 100 mA/cm^2.

In general, the primary issue associated with structures based on MOF pertains to their limited durability during cycling, particularly under OER conditions, which often leads to structural collapse. To address this concern, Shi et al. [87] have introduced a strategy aimed at mitigating this problem for Co-MOF-74 by employing a protective polydopamine (PDA) coating. The resultant PDA-MOF composite exhibits enhanced structural stability under harsh OER conditions and, concurrently, demonstrates improved electrochemical performance. An additional avenue to enhance MOF durability involves the synthesis of meticulously engineered MOF-electrolyte interfaces [67,77]. Du et al. [88] have proposed a novel structure consisting of a CuO_x support with a RuO_2 layer deposited on its surface. The judiciously designed interface successfully addresses RuO_2's stability and activity limitations. Notably, the interfacial atoms, specifically the Ru-O-Co species, play a crucial role in enhancing the system's durability. The presence of ruthenium combined with nearby cobalt atoms significantly improves both the stability and activity of the interface, leading to improved overall performance.

3.2 Carbonized MOF for OER

The primary and most effective approach to addressing the issue of poor stability in metal-organic frameworks (MOF) during the oxygen evolution reaction (OER) process is carbonization. Carbonization involves subjecting organic materials to higher temperatures in a non-reactive atmosphere, such as nitrogen or argon, leading to structural transformation into carbon-based materials. The extent of graphitization achieved is directly influenced by the carbonization temperature, with higher temperatures promoting a higher degree of graphitization [89,90]. Notably, MOF structures consist of organic linkers and possess high surface areas. However, during carbonization, MOF porous structures tend to lose porosity due to structural collapse resulting in a lower surface area

[79,89,91,92]. Furthermore, the presence of certain metals within the MOF framework can lead to their migration [89,93] or sublimation [91,93] during carbonization. This migration often results in the formation of metal agglomerates and the creation of core-shell structures [89], where the metal acts as the core, encapsulated by a carbon shell – making it difficult to contact with electrolyte. Moreover, the migration of metals during the carbonization process can also contribute to the generation of pores by acting as a drilling agent [94]. Therefore, it introduces an additional dimension to the carbonization process and makes it more challenging for MOF-based materials. By understanding and optimizing carbonization conditions, it is possible to enhance MOF stability during the OER process [89]. In addition, it is possible to tailor the resulting carbon material's porosity and surface area for improved performance in various applications.

An effective strategy to enhance the structural integrity of carbonized Metal-Organic Frameworks (CMOF) is by incorporating guest compounds within the MOF structure before carbonization. This approach serves to mitigate structural collapse at high temperatures and prevent metal agglomeration. Wang et al. [90] have successfully implemented this technique by introducing guest structures into HKUST-1(Cu), thereby increasing the specific surface area of the resulting CMOF. By integrating guest compounds, the CMOF undergoes efficient morphological changes, resulting in the creation of more active sites suitable for various catalytic applications. This approach demonstrates promise in bolstering the stability and catalytic performance of carbonized MOF, thereby expanding their potential in diverse fields. Jiao et al. [95] introduced an advanced approach that involved nanocasting SiO_2 into the MOF-PNC-222(Fe) structure. This innovative technique demonstrated significant advancements in preventing iron atom agglomeration during carbonization by establishing a physical barrier through SiO_2 incorporation. Consequently, the synthesis of single-atom catalysts (SAC) became feasible. Additionally, this design enabled the formation of a SiO_2-FeN_4 interface, effectively enhancing the electrocatalyst's catalytic efficiency. The outcome of this approach yielded an efficient electrocatalyst with high iron loading and the absence of iron particle agglomeration. This breakthrough in catalyst design and synthesis holds substantial promise for superior electrocatalytic performance.

An alternative approach involves the modulation and fine-tuning of carbonization process parameters, such as temperature and time, to synthesize advanced structures [89,93]. Cendrowski et al. [93] demonstrated that precise control of the carbonization temperature in the case of MOF-5 allows for the manipulation of zinc (Zn) migration and

the synthesis of distinct structures based on this phenomenon. Carbonization at a temperature of 600°C resulted in the formation of Zn-core structures, with carbonized MOF-5 featuring agglomerates of Zn particles on the surface. Upon raising the temperature to the range of 700-900°C, Zn migration led to the formation of Zn-based rods intertwined with the CMOF structure. Finally, at a temperature of 1000°C, the Zn underwent sublimation from the CMOF, leaving behind a structure composed solely of carbon. By precisely controlling the carbonization temperature, it becomes possible to achieve diverse structures and morphologies, as well as exercise control over the migration behaviour of metal species at high temperatures. This ability to manipulate the carbonization conditions offers a promising avenue for tailoring the properties and functionalities of carbonized MOF, opening up new possibilities for their application in various fields.

Chapter IV: Experimental Methods

1. Synthesis methods

In this work, one type of metal-organic frameworks (MOF) was synthesised, modified and investigated -aluminium (Al)-based MOF.

1.1 Al-MOF synthesis

Aluminium metal-organic framework (Al-MOF) was synthesized via self-assembly in a round-bottom flask under reflux and heated and mixed with a magnetic stirrer (IKA Plate - RCT digital). A total of 7.5 grams of aluminium nitrate nonahydrate ($Al(NO_3)_3 \cdot 9H_2O$), 2.44 grams of 2,5-pyridinedicarboxylic acid (PDC), and 160 millilitres of N,N-dimethylformamide (DMF) were combined and stirred until a clear solution was obtained. The resulting solution was heated to 135°C for 72 hours. Following the heating process, the mixture was subjected to a vacuum evaporator until only a powder residue remained in the flask as presented in a scheme in Figure 15 [89]. The resulting powder was ground in a mortar and transferred to a vacuum dryer. The powder was left in the vacuum dryer overnight, maintaining a temperature of 100°C and a pressure of 30 millibars.

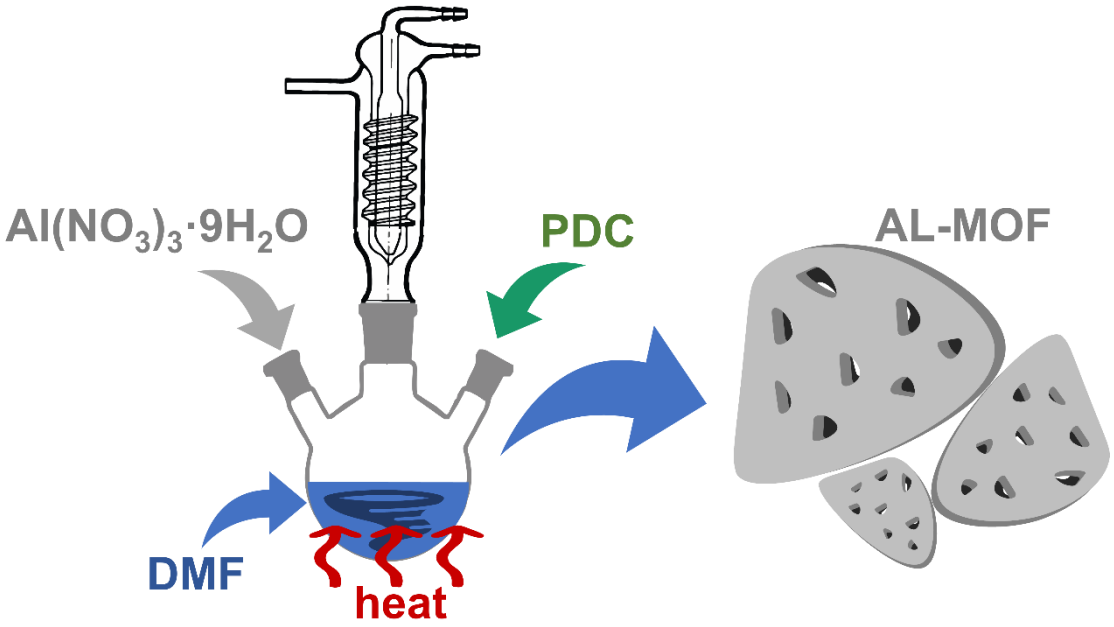

Figure 15. Scheme of Al-MOF synthesis.

1.1.1 Al-MOF modifications

During the synthesis of the Al-MOF, the first modification was introduced by incorporating varying amounts of platinum (Pt), nickel (Ni) and cobalt (Co) or a combination of Ni and Pt, into the synthesis mixture. These metals were added in different proportions relative to aluminium, with ratios of 1:1, 1:9, and 1:99. The reaction mixture, once all the ingredients were dissolved, underwent the same heating and treatment process as the basic Al-MOF synthesis method described earlier.

The third modification included the application of different Ni salts and investigating the impact of N-doping with cyanamide (CA) in ratio to Ni(100)-CMOF 1:1 and 0.5:1 conducted in standard optimized parameters. Both materials were ground in a mortar and placed in a crucible to conduct the carbonization. Therefore nitrogen enriched catalysts were synthesized.

The fourth modification included the carbonization of Ni+Pt(1:1) in a ratio of 1:99 to Al-MOF in a 10% NH_3/90% N_2 gas atmosphere with the same parameters as the standard carbonization method in the N_2 atmosphere presented in this work.

The fifth modification involved a post-synthesis step, where the Al-MOF structure was modified. In this step, Al-MOF was combined with a solution of ethanol and diphenyl chlorophosphate (DCP) to introduce a phosphorus compound into the structure. A total of 200 milligrams of Al-MOF were mixed with ethanol-DCP mixtures of varying concentrations, specifically 1 mM, 10 mM, 100 mM, and 1 M. The mixture was thoroughly mixed until complete drying was achieved. Subsequently, the Al-MOF-DCP composite obtained from the mixture was carbonized.

1.1.2 Thermal Treatment of Al-MOF and its Functionalization

The Al-MOF underwent a series of temperature treatments ranging from 150°C to 950°C, with an increment of 100°C and a heating rate of 10°C/min. This treatment was conducted in a nitrogen atmosphere for 2 hours. Temperature-treated Al-MOF samples and structural changes were characterized using Raman spectroscopy, thermogravimetric analysis, and transmission electron microscopy.

Following thermal treatment, the Al-MOF was functionalized using cobalt(II) nitrate ($Co(NO_3)_2$) at various concentrations (1 mM, 10 mM, 100 mM, and 1 M). In this process, 20 milligrams of thermally-treated Al-MOF were immersed in 2 millilitres of cobalt solution in ethanol. The mixture was sonicated for 15 minutes and dried. The resulting

powder was then transferred to a crucible and subjected to a reduction in a hydrogen atmosphere (5% H_2/95% N_2). The reduction process involved increasing the temperature from room temperature (RT) to 300°C, with an increment of 100°C and a heating rate of 10°C/min. No additional treatments were performed on the materials before the investigation [89].

In the case of DCP-functionalized Al-MOF, the composite was carbonized at 750°C for 2 hours in a nitrogen atmosphere.

2. Characterization of MOF and CMOF structures

MOF and CMOF structures of both Al-MOF and Zr-MOF were studied and monitored via an array of physicochemical methods. The FEI Tecnai F20 microscope operating at 200 kV acceleration voltage was utilized for high-resolution transmission electron microscopy (HR-TEM) imaging. Moreover, for elemental mapping, energy dispersive spectroscopy (EDS) combined with TEM was utilized. X-ray photoelectron spectroscopy (XPS) was employed to investigate the chemical composition and relative atomic percentages on the surface of the samples. The XPS measurements were carried out using MgKα (hν = 1253.6 eV) radiation in a PREVAC system from Poland, equipped with a Scienta SES 2002 electron energy analyser from Sweden. The electron energy analyser operated with constant transmission energy (Ep = 50 eV), and the analysis chamber was evacuated to a pressure below $5 \cdot 10^{-9}$ mbar. For determining the specific surface area, the Micrometrics ASAP 2460 apparatus collected N_2 adsorption/desorption isotherms at liquid nitrogen temperatures. The chemical composition of the materials under study was determined through X-ray powder diffraction - XRD (Aeris, Malvern Panalytical) with CuKα radiation. Raman spectra were obtained using an InVia Raman microscope from Renishaw, employing an excitation wavelength of 785 nm. Additionally, the SDT Q600 Simultaneous TGA/DSC instrument was used to perform thermogravimetric analysis in the oxygen atmosphere. The analysis was carried out at a heating rate of 10°C/min within the temperature range of 20–800°C.

3. Electrochemical testing of MOF-based materials

The electrochemical properties of structures based on metal-organic frameworks (MOF) or carbonized metal-organic frameworks (CMOF) were investigated concerning the processes of hydrogen evolution reaction (HER) and oxygen evolution reaction

(OER). To perform these investigations, all measurements were conducted using the EC-LAB VMP multichannel potentiostat manufactured by BioLogic Science Instruments in France. Electrodes for both processes were prepared in the same manner: 10 mg of the electrocatalyst was mixed with 1 mL of Nafion® 0.05% solution in 20% isopropanol/water. Such mixture was sonicated for 30 minutes with ultrasound cup-horn sonotrode. The suspension of the catalyst was dropcasted on a working electrode (graphite foil 1 cm x 1 cm; 99.8%, GoodFellow) in an amount of 30 μL on each side of the electrode. Then all of the measurements were conducted in a three-electrode system (Figure 16), where the working electrode (WE) was attached to a platinum/PTFE electrode, the auxiliary electrode (CE) was a platinum spring (ALS Co. Japan) and the reference electrode (RE) was mercury oxide electrode (MOE) filled with 1M KOH (ALS Co. Japan). All experiments were conducted at a stable temperature of 25°C under a thermostat (Hubner KISS 6, Germany) in a glass reactor, where the electrolyte for alkaline measurements was 1 M KOH (pH~13.5). All the potentials were calculated to a reversible hydrogen electrode (RHE) according to the equation:

$$E_{RHE} = E_{MOE} + 0.128 + pH \cdot 0.059$$

where 0.128 V is an electromotive force of MOE, 0.059 is the coefficient factor from the Nerst equation, pH is the pH value of the electrolyte.

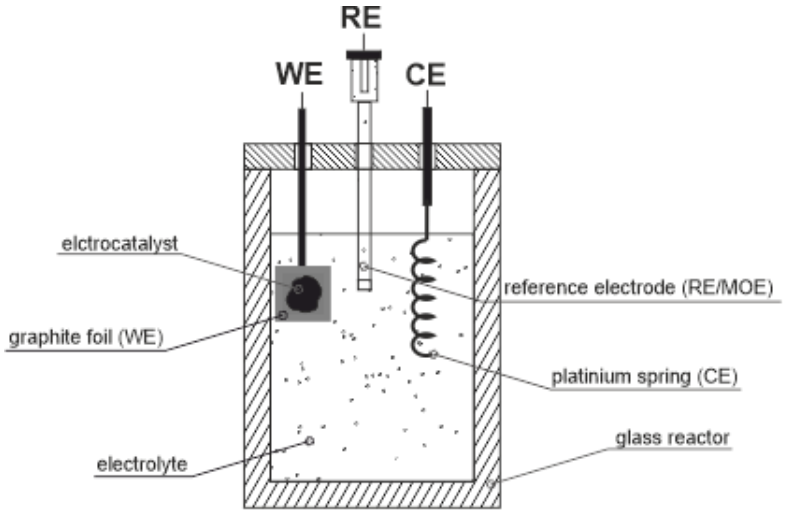

Figure 16. Schematic representation of electrocatalyst measurement cell.

3.1 HER/OER measurements and techniques

3.1.1 Open circuit voltage

Open circuit voltage (OCV) measurement is a technique used to determine the thermodynamic potential of an electrochemical reaction. The OCV is measured by connecting the working electrode and reference electrode in an electrochemical cell without external current flow. The voltage difference between the working electrode and the reference electrode is OCV. Notably, after immersing the electrodes in electrolyte and purging them for 30 minutes with nitrogen, OCV measurements were conducted for 15 minutes. Next all further measurement potentials were set according to OCV value (e.g. OCV was set as a 0 V state during measurement – E_{OCV}). A typical measurement is presented in Figure 17.

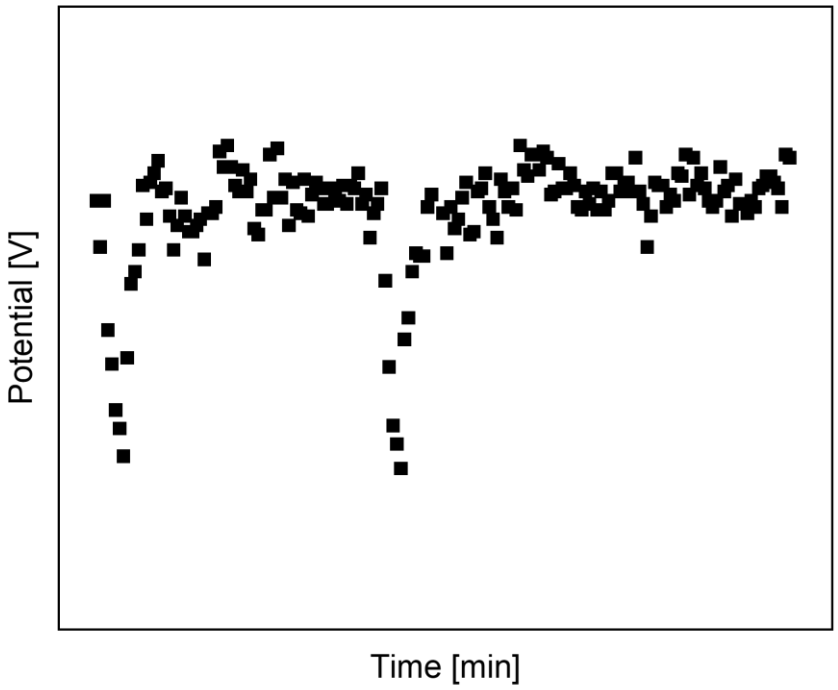

Figure 17. Typical plot of OCV measurement.

3.1.2 Ohmic drop compensation – potentiostatic electrochemical impedance spectroscopy

The ohmic drop is a fundamental component defined by the resistance within the solution between the working electrode and the reference electrode. This parameter holds

significant importance as it can cause substantial distortion in the voltammetric response. To accurately determine the uncompensated resistance (R_u), it is recommended to measure at high frequencies. The potentiostatic electrochemical impedance spectroscopy (PEIS) technique provides an effective means to determine solution resistance at a single high-frequency value.

PEIS measurements were conducted using the following parameters:

- A fixed frequency of 100 kHz was selected for the measurements. This frequency is conducive to accurate impedance data.
- A sinusoidal voltage signal with an amplitude (V_a) of 20 mV was recorded during the measurements. This voltage amplitude ensures appropriate excitation of the system while avoiding potential adverse effects.
- The measurements were compensated at 85%. This compensation level helps to minimize errors and enhances the accuracy of acquired impedance data.
- The measurements were performed within an electrochemical potential (E) range from -2.5 V to 2.5 V. This potential range provides sufficient coverage to capture the relevant electrochemical behaviour and obtain comprehensive impedance information.

By employing these parameters in the PEIS technique, it is possible to effectively determine the solution resistance (R_u) at a high-frequency value. This allows for a comprehensive understanding of the ohmic drop and facilitates an accurate interpretation of the voltametric response.

3.1.3 Cyclic voltammetry

Cyclic voltammetry (CV) is a highly prevalent and extensively employed technique in electrochemistry for obtaining qualitative insights into electrochemical reactions. This versatile method furnishes valuable information of various aspects such as redox processes, heterogeneous electron-transfer reactions, and adsorption phenomena. Furthermore, CV facilitates the accurate determination of electroactive species' redox potential. The cyclic voltammogram, generated through CV, represents the current response as a function of the applied potential. This graphical representation encapsulates crucial electrochemical behaviour and aids in the comprehensive characterization and analysis of the system under investigation.

As previously indicated, the potential was established based on the open circuit potential (E_{OCV}). The experimental procedure began by allowing the system to stabilize, which entailed a waiting period of 1 minute. Subsequently, the potential scan was executed with a step size of 10 mV/s, relative to the vertex potential E_1 of 0.1 V (versus E_{OCV}). The resulting data were recorded at intervals of 0.1 seconds to ensure comprehensive temporal resolution. To investigate the impact of different scan speeds on electrochemical behaviour, the measurement procedure was repeated at multiple scan speeds: specifically, 20 mV/s, 50 mV/ and 100 mV/s. This systematic approach enabled the acquisition of a range of data points, facilitating a comprehensive analysis of electrochemical processes under varying experimental conditions. A typical plot is presented in Figure 18.

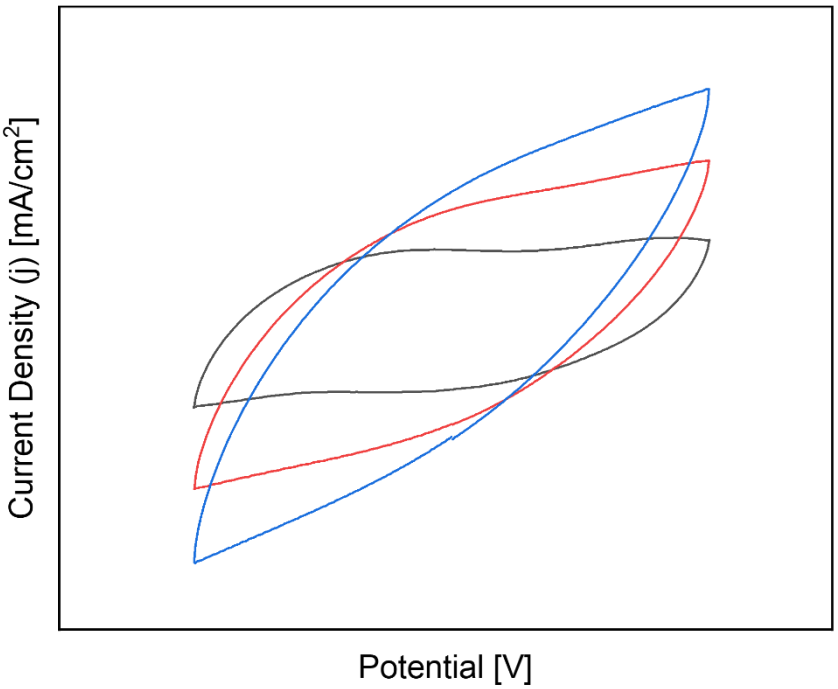

Figure 18. Typical plot of cyclovoltammetry measurement.

3.1.4 Linear sweep voltammetry

Potentiodynamic measurement refers to an electrochemical measurement technique known as linear sweep voltammetry (LSV). LSV is employed to investigate the electrochemical behaviour of a system by varying the potential linearly with time. This technique offers valuable insights into redox processes, electrode kinetics, and other

electrochemical phenomena. In LSV, the potential is continuously swept over a specified range at a constant scan rate. The scan rate determines the speed at which the potential is changed per unit of time. By monitoring the resulting current response as a function of the applied potential, detailed information regarding the electrochemical reactions taking place at the working electrode can be obtained. During a potentiodynamic LSV measurement, several key steps are typically followed. Throughout the potential sweep, the resulting current is recorded as a function of time or potential. This current response, known as the voltammogram, provides valuable information about electrochemical reactions occurring at the electrode surface. This includes oxidation and reduction processes. By analysing the shape, peak positions, and magnitudes of the voltammogram, significant electrochemical parameters such as redox potentials, reaction rates, and electrode surface properties can be determined. This information contributes to a deeper understanding of the system under investigation and aids in the development of electrochemical applications and technologies. To perform measurements related to the HER and OER, specific parameters were employed. The scan rate was set at a constant value of 5 mV/s, ensuring a controlled rate of voltage change during the experiment. The scan was initiated from a voltage of 0 V (versus E_{OCV}) and continued up to 2.4 V (versus E_{RE}) for the OER measurements or -2.4 V (versus E_{RE}) for the HER measurements. Subsequently, the scan direction was reversed, returning the potential back to 0 V. For these measurements, the potential range was set more broadly, spanning from -10 V to 10 V. This extended range allowed for the exploration of a wider electrochemical space, enabling a comprehensive investigation of the electrochemical behaviour and providing valuable insights into the kinetics and mechanisms of the HER and OER processes. By carefully selecting these parameters and conducting the measurements within the defined potential range, it becomes possible to evaluate the electrochemical characteristics of HER and OER reactions with enhanced precision and understanding. Typical polarization plots are presented in Figure 19.

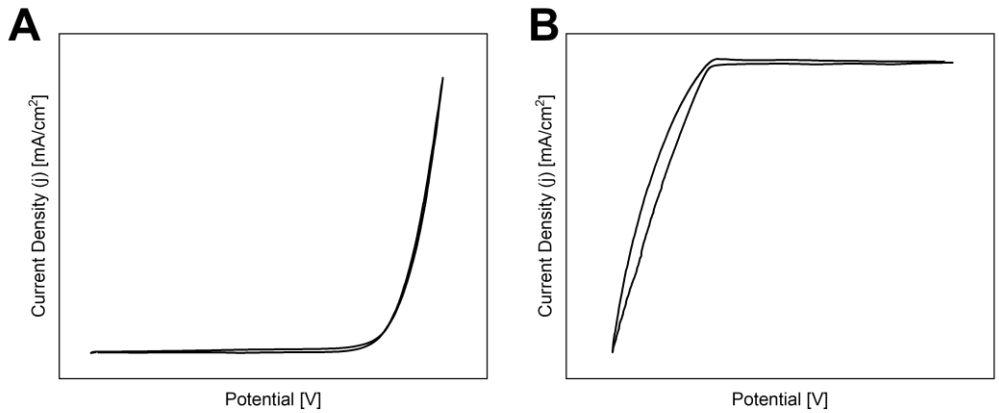

Figure 19. Linear sweep voltammetry plots of OER (A) and HER (B).

3.1.5 Electrochemical impedance spectroscopy

Electrochemical impedance spectroscopy (EIS) is a versatile technique with wide-ranging applications in corrosion studies, battery development, fuel cells, sensor technology, and physical electrochemistry. It serves as a valuable tool for obtaining information about various reaction parameters, corrosion rates, electrode surface porosity, coating properties, mass transport characteristics, and interfacial capacitance measurements. In the context of the HER and OER, galvanostatic electrochemical impedance spectroscopy (GEIS) was employed. GEIS allows impedance measurements while operating in galvanostatic mode, where sinusoidal perturbations are applied on direct current (DC). This technique enables electrochemical impedance evaluation under controlled current conditions. The parameters employed for both HER and OER measurements were similar, with one key difference: the applied current. For the OER measurements, a current of I=10 mA was used, while for the HER measurements, a current of I=-10 mA was applied. These current values facilitated the investigation of impedance behaviour specific to each reaction. The impedance scan was performed over a frequency range from 200 kHz to 100 mHz. A sinusoidal perturbation with an amplitude of V_a=10 mV was applied to the system. The potential range for these measurements extended from -10 V to 10 V, encompassing a wide electrochemical window to capture a comprehensive range of impedance data. By employing these parameters and techniques, GEIS enabled the detailed characterization of HER and OER processes. This provided valuable insights into the electrochemical behaviour, reaction kinetics, and impedance

properties associated with these reactions. A typical measurement is presented in Figure 20.

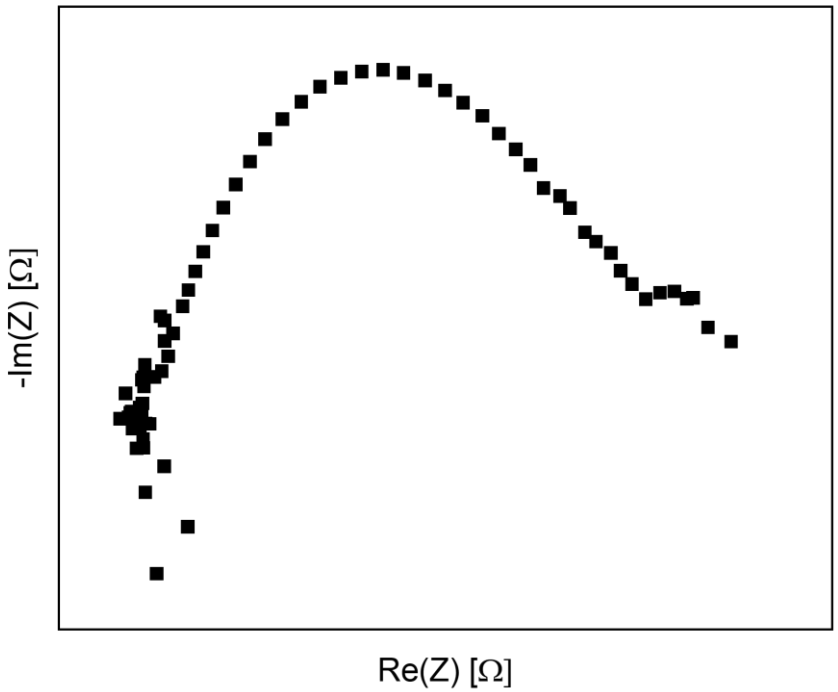

Figure 20. Electrochemical impedance spectroscopy (EIS) measurement.

3.1.6 Tafel slope measurement

The Tafel slope is a critical parameter used for electrochemical reactions characterization and analysis. It offers valuable insights into the relationship between the current density (j) and the overpotential (η), which is the deviation of the electrode potential from its thermodynamic equilibrium value. The Tafel slope is typically expressed in units of volts per decade (V/dec) indicating the change in overpotential required to produce a tenfold change in current density. It quantifies the rate at which current density varies in response to overpotential changes. The Tafel slope plays a crucial role in understanding the reaction mechanism, determining the reaction rate, and assessing the efficiency of electrochemical processes. In the measurements of OER and HER, the Tafel slope was determined under potentiostatic conditions, where a constant current was applied for 5 minutes. Specifically, for the OER measurements, a series of currents ranging from 0.1 mA to 40 mA were utilized. For the HER measurements, the same current values were employed with negative polarity. During these potentiostatic measurements, the electrode potential was controlled by applying a constant current for

the specified period. This approach allows the determination of the Tafel slope by analysing the resulting overpotential-current relationship. For the OER, a range of positive currents (0.1 mA, 0.3 mA, 0.5 mA, 1 mA, 2 mA, 5 mA, 10 mA, 20 mA, 30 mA, and 40 mA) was employed to systematically explore electrochemical behaviour and obtain a comprehensive understanding of reaction kinetics. Similarly, for the HER, the same currents as used in the OER measurements were applied, but with negative polarity. This facilitated the investigation of the electrochemical behaviour associated with hydrogen evolution. A typical plot for this method is presented in Figure 21.

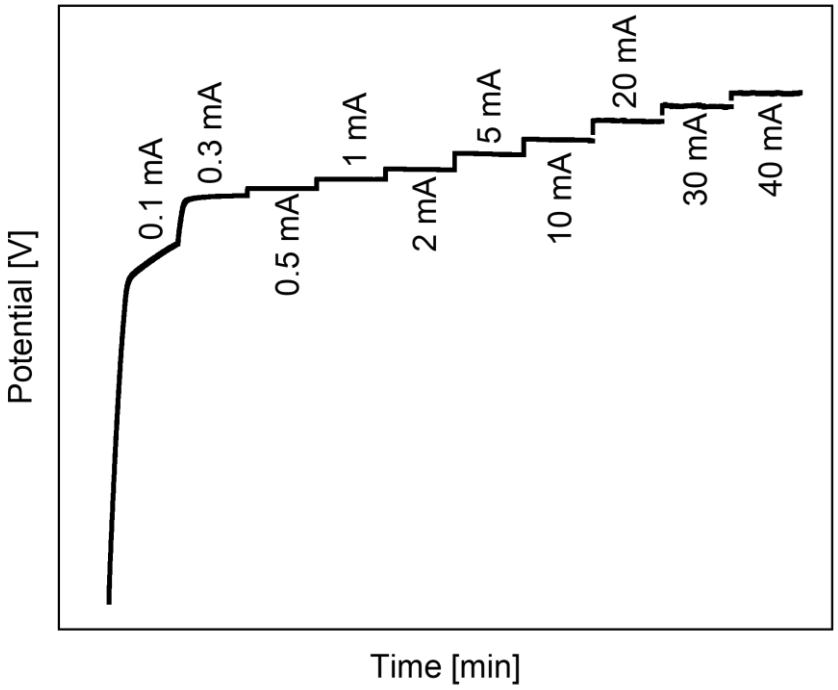

Figure 21. Typical measurement for chronopotentiometry used for Tafel slope calculation.

3.1.7 Stability measurement

Stability measurement for HER and OER involves assessing the long-term performance and durability of the electrochemical system under study. This measurement aims to determine the system's ability to sustain the desired electrochemical reaction over an extended period without significant degradation or loss of performance. In stability measurements for HER and OER, a constant current is applied to the system for a prolonged time. For HER, currents of -10 mA and -20 mA are utilized, while for OER,

currents of 10 mA and 20 mA are employed. These current values are selected to represent the relevant operating conditions and to explore the system's response to a constant current input over an extended time frame. By subjecting the system to this long-term current application, stability measurement allows for observation of system behaviour and performance over an extended duration. During stability measurement, it is critical to monitor the system's response to constant current input. If the electrocatalyst exhibits an increasing potential response over time, it may indicate the weakening or degradation of the material. These measurements are crucial for advancing the field of electrocatalysis and facilitating the design of efficient and robust electrochemical systems for sustainable energy conversion. A typical plot of stability measurement is presented in Figure 22.

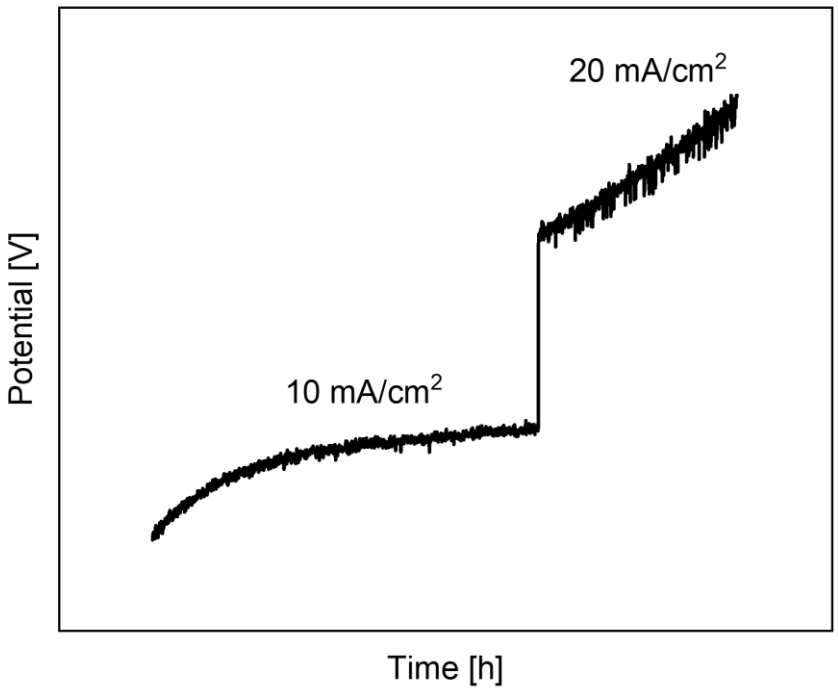

Figure 22. Typical stability measurement plot.

Chapter V: Results and Discussion

1. Physicochemical characterization

1.1 Al-MOF

Synthesis via solvothermal method Al-MOF structure was investigated by an array of methods to fully understand the morphological changes in the structure in further

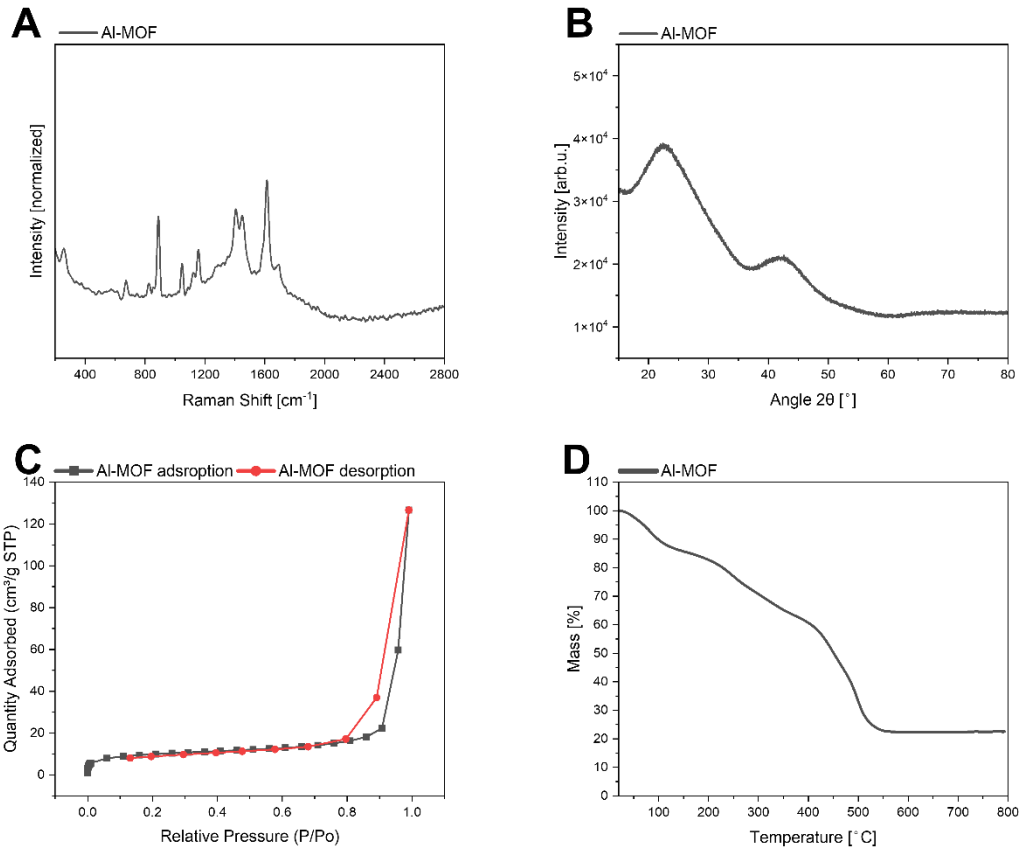

Figure 23. Physicochemical analysis of Al-MOF: (A) Raman spectroscopy, (B) XRD, (C) N_2 adsorption/desorption, (D) TGA.

processes of carbonization and functionalization. The most important objective for electrocatalyst design is to assess the structural properties and if they follow the synthesis route and predictions.

Figure 23 illustrates the physicochemical analysis conducted on the Al-MOF. In Figure 23A, the Raman spectrum of Al-MOF displays significant peaks at 256, 673, 829, 889, 1047, 1157, 1406, 1450, 1612, and 1695 cm^{-1}, which can be ascribed to MIL-53(Al) and other aluminium-containing materials. On the contrary, Figure 23B reveals an XRD pattern significantly different from the previous spectrum, with only two broad peaks instead of sharp ones. The first peak, observed between 20˚ and 30˚, is attributed to

amorphous carbon. The second peak, ranging from 35˚ to 50˚, corresponds to the amorphous form of aluminium oxide. Moving on to Figure 23C, presents the N_2 adsorption and desorption measurement, exhibiting a type IV isotherm with noticeable hysteresis. The specific surface area calculated using the BET method (SSA_{BET}) is 35 m^2/g. In Figure 23D, the thermal gravimetric analysis (TGA) of Al-MOF is depicted. The structure exhibits limited thermal stability and undergoes decomposition as the temperature rises. It reaches 550 C, beyond which no further decomposition or oxidation occurs. The ash content observed amounts to 25% of the sample mass, indicating aluminium presence [89].

The morphological analysis of the Al-MOF was performed using SEM, as depicted

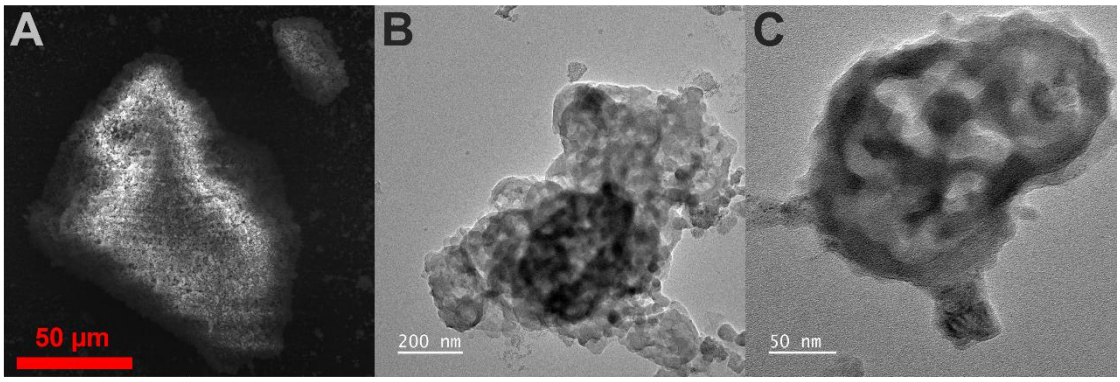

Figure 24. SEM image (A) and TEM images (B,C) of Al-MOF.

in Figure 24A, which confirms the presence of a porous structure within the MOF. Furthermore, the analysis reveals that the structure is composed of small MOF flakes. Subsequently, TEM was employed to delve deeper into the Al-MOF structural characteristics. TEM analysis, as illustrated in Figures 24B and C, provides compelling evidence that the Al-MOF exhibits a distinct flake structure with discernible pores. Notably, the TEM images also indicate that the 2D flakes deviate from flatness, displaying a distinctly wriggled morphology.

1.2 Carbonization of Al-MOF

To enhance the structural stability of the Al-MOF and render it suitable for electrochemical experiments, a carbonization process was employed. The Al-MOF was subjected to a range of high temperatures, ranging from 350˚C to 950˚C, with incremental temperature increments of 100˚C. Following this thermal treatment, the resultant

materials were accurately examined to evaluate any structural modifications that may have occurred. Based on that optimized structure was selected.

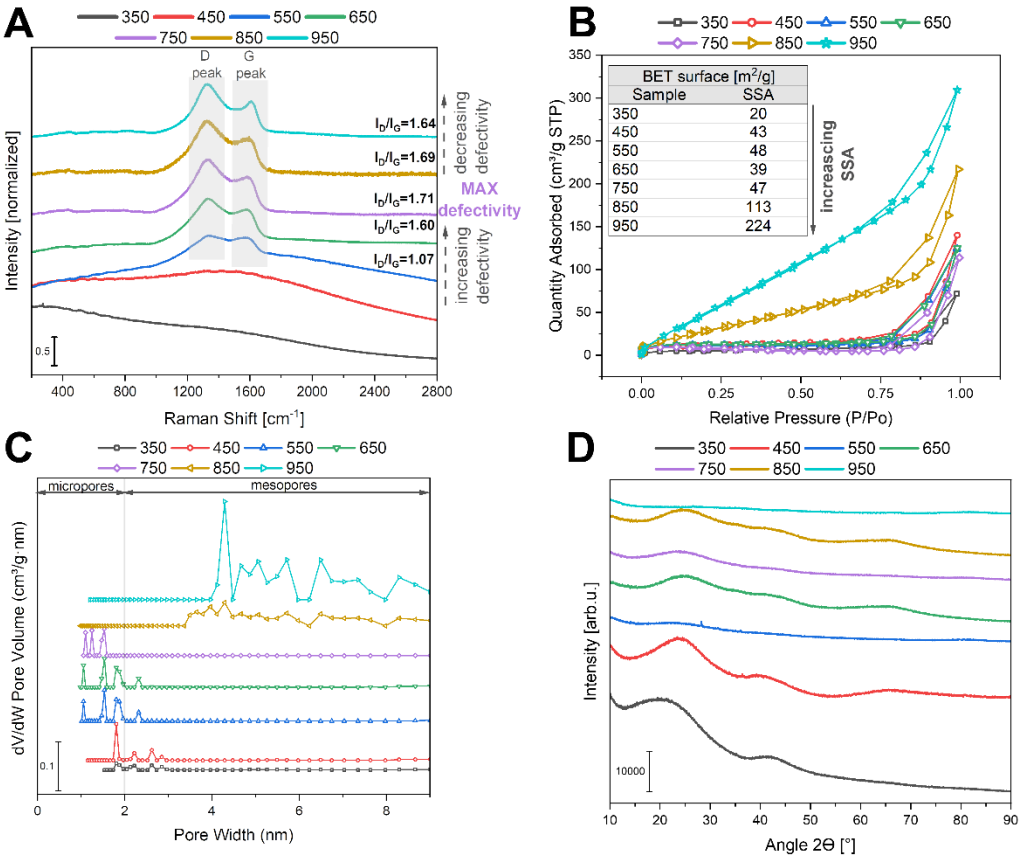

Figure 25. Raman spectra (A), N_2 adsorption/desorption (B), DFT calculation of pores size distribution (C) and XRD patterns (D) of thermal treated Al-MOF in 350˚C, 450˚C, 550˚C, 650˚C, 750˚C, 850˚C and 950˚C.

In Figure 25 physicochemical analysis of examined structures is presented. The Raman spectra (Figure 25A) were utilized to determine carbon-structure formation and its defectiveness. For most of the investigated material, two peaks can be distinguished D and G. The G peak, which manifests at approximately 1580 cm^{-1}, is associated with the in-plane vibrational motion of carbon atoms bonded in the sp^2 configuration within the material. This peak originates from the doubly degenerate zone-centered phonon E_{2g} mode, which corresponds to carbon-carbon (C-C) bond stretching. The presence and intensity of the G peak provide valuable insights into the graphitic nature and crystalline quality of the material. A strong and well-defined G peak signifies a high level of graphitic ordering and structural integrity. On the other hand, the D peak is typically observed near 1340 cm^{-1} and can be attributed to the breathing modes of carbon atoms bonded in the sp^2 configuration. It arises from the transverse optical (TO) phonon mode near the K points in the Brillouin zone. The D peak is highly sensitive to defects,

disorders, and structural modifications in the material. In pristine graphene, the D peak is generally weak or even undetectable due to significant defects. However, in materials with structural imperfections such as lattice vacancies, edges, or grain boundaries, the D peak becomes more pronounced. Its activation necessitates a second-order Raman scattering process involving intermittent double resonance, making it a reliable indicator of the presence and density of defects within the material [96]. In contrast, Al-MOF samples subjected to treatment temperatures of 350˚C and 450˚C exhibit no distinguishable peaks. This can be attributed to the incomplete formation of a carbon structure at these temperatures, resulting in the absence of characteristic carbon-related peaks. Furthermore, the absence of all Al-MOF peaks can be attributed to structural transformations and thermal decomposition induced by the treatment process. The defects ratio, represented by the I_D/I_G intensity ratio, can be utilized to calculate the extent of defects present in the material. As the temperature is elevated from 550˚C to 750˚C, an observable increase in the I_D/I_G ratio is noted, indicating the formation of a higher proportion of defective structures. In contrast, at higher temperatures such as 850˚C and 950˚C, an enhanced degree of graphitization takes place, leading to a more ordered carbon structure. Consequently, the I_D/I_G ratio decreases, reflecting the reduction in the presence of defects within the material. Figure 25B illustrates the adsorption/desorption isotherms of temperature-treated Al-MOF. Notably, all isotherms exhibit type IV behaviour with visible hysteresis. Interestingly, as the specific surface area (SSA) of Al-MOF fluctuates around its base structure, a significant increase in SSA is observed for samples treated at 850˚C and 950˚C. This intriguing phenomenon can be elucidated by the pore size distribution, as calculated using the density functional theory (DFT) mathematical model, as shown in Figure 25C. Up to 850 C, a substantial proportion of pores are localized in the micropore region. However, a substantial morphological transformation occurs in the materials treated at 850˚C and 950˚C, leading to the collapse of micropores and the formation of mesopores. This structural rearrangement results in a notable increase in the SSA. The observed changes can be attributed to aluminium migration within the material. Aluminium can act as a "drill" during structural evolution, facilitating micropore collapse and mesopore emergence. Figure 25D presents the XRD reflectograms of the materials under investigation. Similar to the Al-MOF, the reflectograms do not exhibit significant crystallinity in the structure, leading to broad peaks characteristic of amorphous carbon and aluminium oxide.

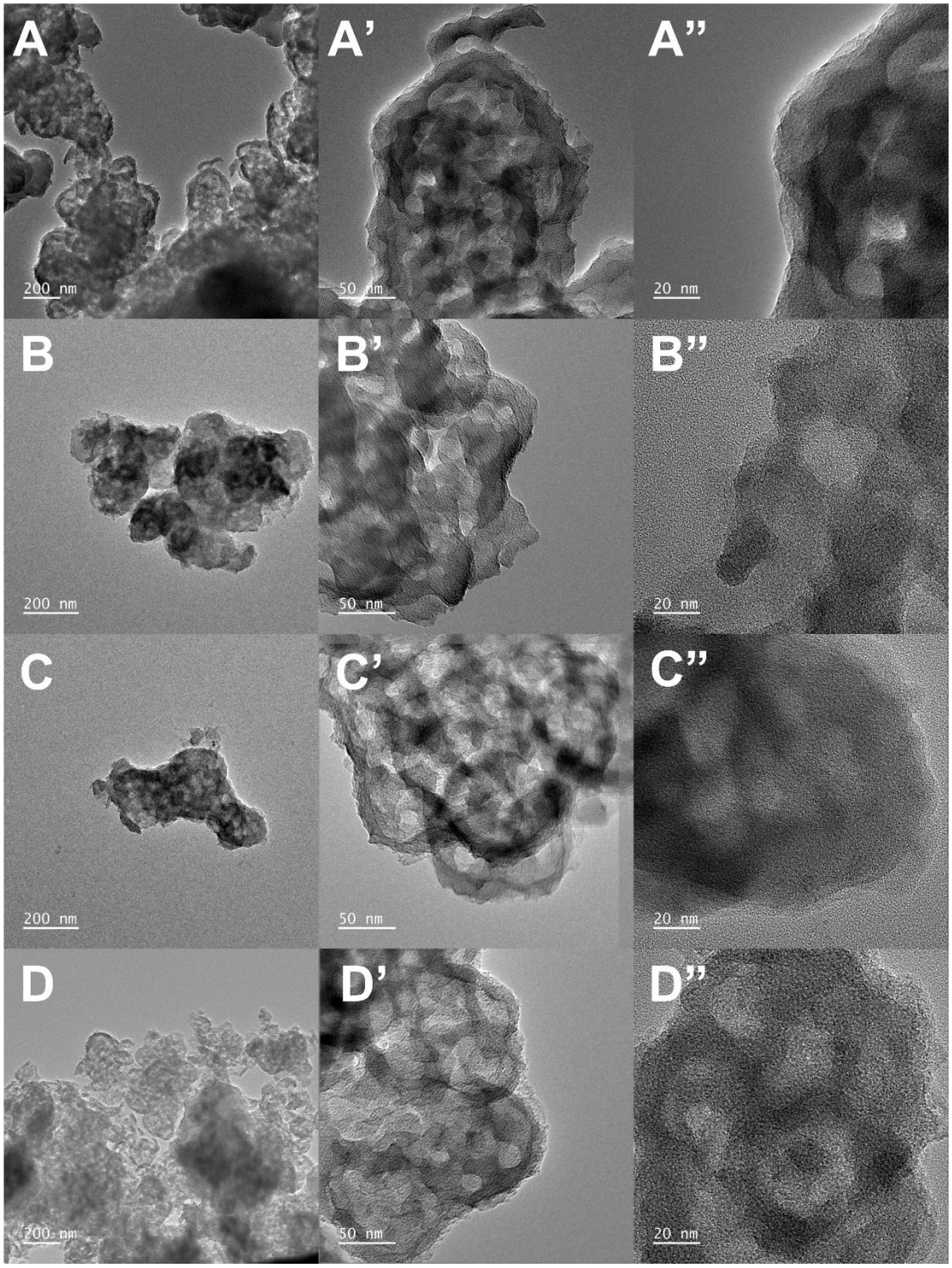

Figure 26. TEM images of thermal-treated Al-MOF at: 350˚C (A,A',A''), 450˚C (B,B',B''), 550˚C (C,C',C'') and 650˚C (D,D',D'').

The TEM images presented in Figures 26 and 27 depict thermal-treated Al-MOF samples. It is evident that, despite the temperature, the MOF structure generally maintains its integrity. However, up to 650°C, the structure remains composed of individual flakes agglomerated into larger bundles. At higher temperatures, an interconnected structure becomes apparent. Figure 27 shows more graphitized carbon is observed. Nevertheless,

elevated temperatures promote the formation of core-shell structures, characterized by highly graphitized shells, which are difficult to remove. These structures significantly

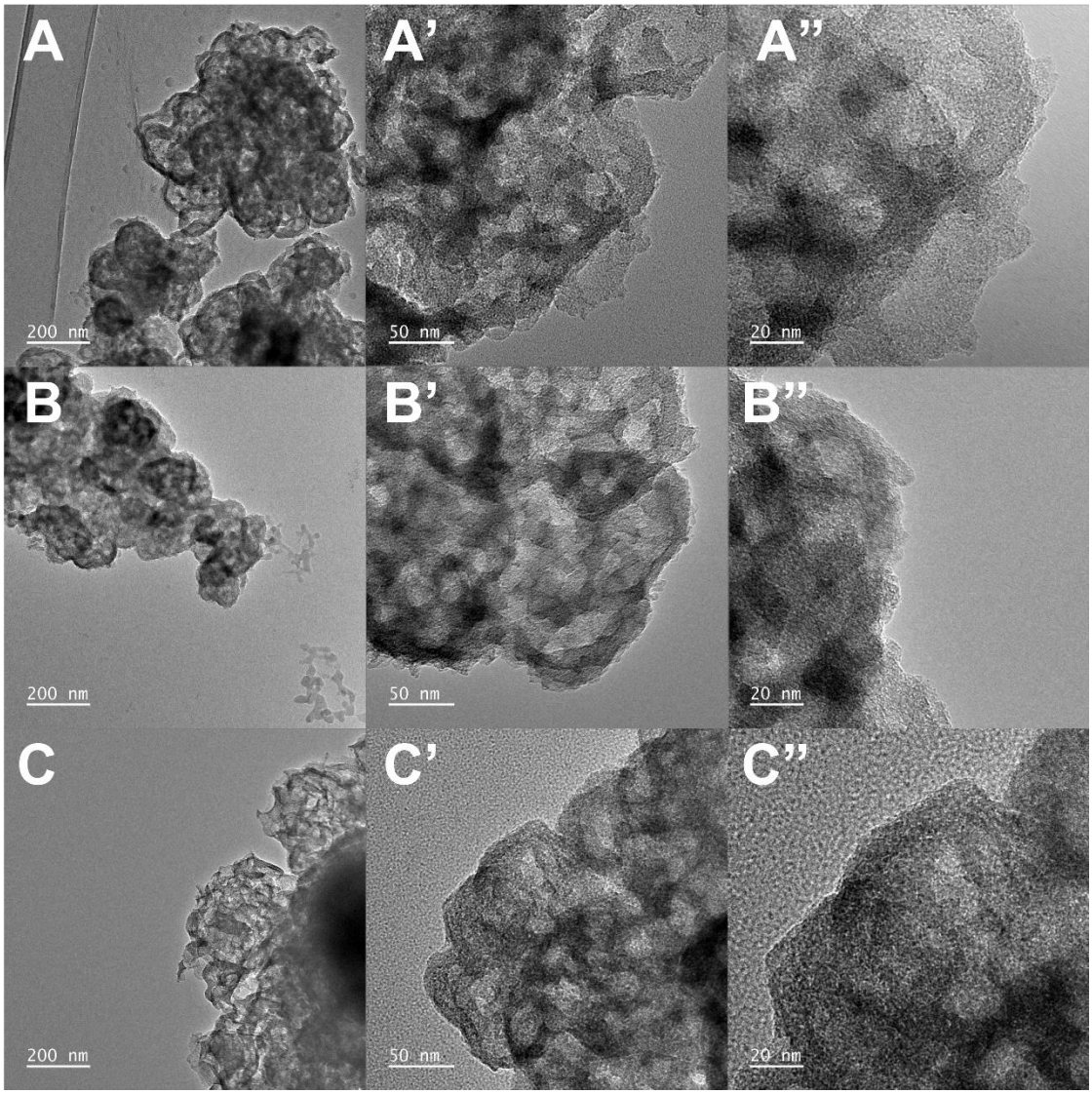

Figure 27. TEM images of thermal-treated Al-MOF at: 750˚C (A,A',A"), 850˚C (B,B',B") and 950˚C (C,C',C").

reduce the metal-electrolyte interface in electrochemical processes [89].

In summary, the low-temperature treatment of Al-MOF results in individual MOF structures with low-graphitized carbons and a relatively low surface area concentrated mainly in the microporous region. However, these carbons are less stable under harsh conditions, particularly in oxidizing environments. On the other hand, high-temperature treated Al-MOF exhibits a more ordered structure with highly graphitized carbon. Nevertheless, this can lead to significant catalyst deactivation due to core-shell structures. The Al-MOF treated at 750°C offers the advantages of both low- and high-temperature treatments, combining mesoporous porosity, a high defect ratio, and an interconnected

structure without core shells. As a result, these parameters have been identified as optimal for Al-MOF carbonization.

1.3 Functionalization of Al-MOF with nickel and cobalt

Al-MOF or Al-MOF temperature-treated (CMOF) were functionalized with nickel (Ni) in cobalt (Co) in two ways: 1) *in-situ* where Ni/Co was added to the reaction mixture of Al-MOF in different ratios of Ni/Co:Al – 1:1, 1:10, 1:100 and then temperature-treated, 2) *ex-situ*, where CMOF was immersed in Ni/Co salt.

1.3.1 *In-situ* functionalization

To incorporate catalytically active species into Al-MOF structures, partial aluminium substitution with nickel or cobalt salts was performed. The resulting MOF were carbonized at 750°C. This process led to the formation of two distinct groups: Ni(1)-CMOF, Ni(10)-CMOF, Ni(100)-CMOF, and Co(1)-CMOF, Co(10)-CMOF, Co(100)-CMOF, where the numbers represent the aluminium content in the respective samples (Figure 28).

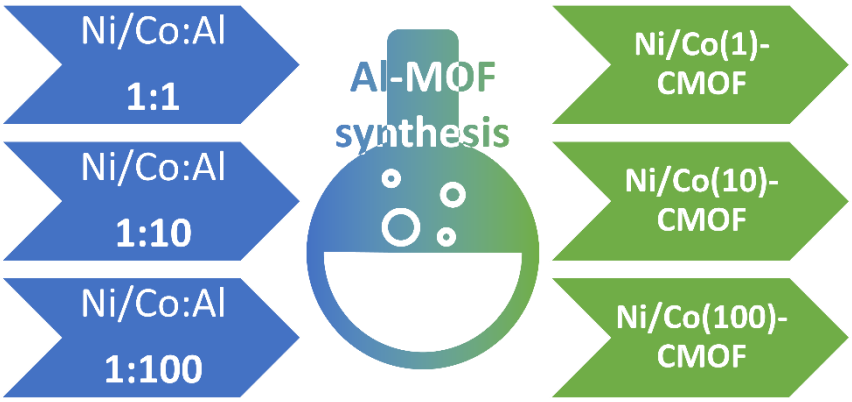

Figure 28. Schematic representation of Al-MOF *in-situ* functionalization with Ni/Co.

The morphology and functionalization effects were investigated using TEM. Figure 29 illustrates the in-situ functionalization of Al-MOF with nickel. It is observed that nanoparticles (NP) of nickel/nickel oxide are present in Ni(1)-CMOF and Ni(10)-CMOF, with a decreasing trend in their abundance. Notably, in Ni(10)-CMOF, the Ni-NPs are primarily concentrated at the edges where most defects are located, in contrast to

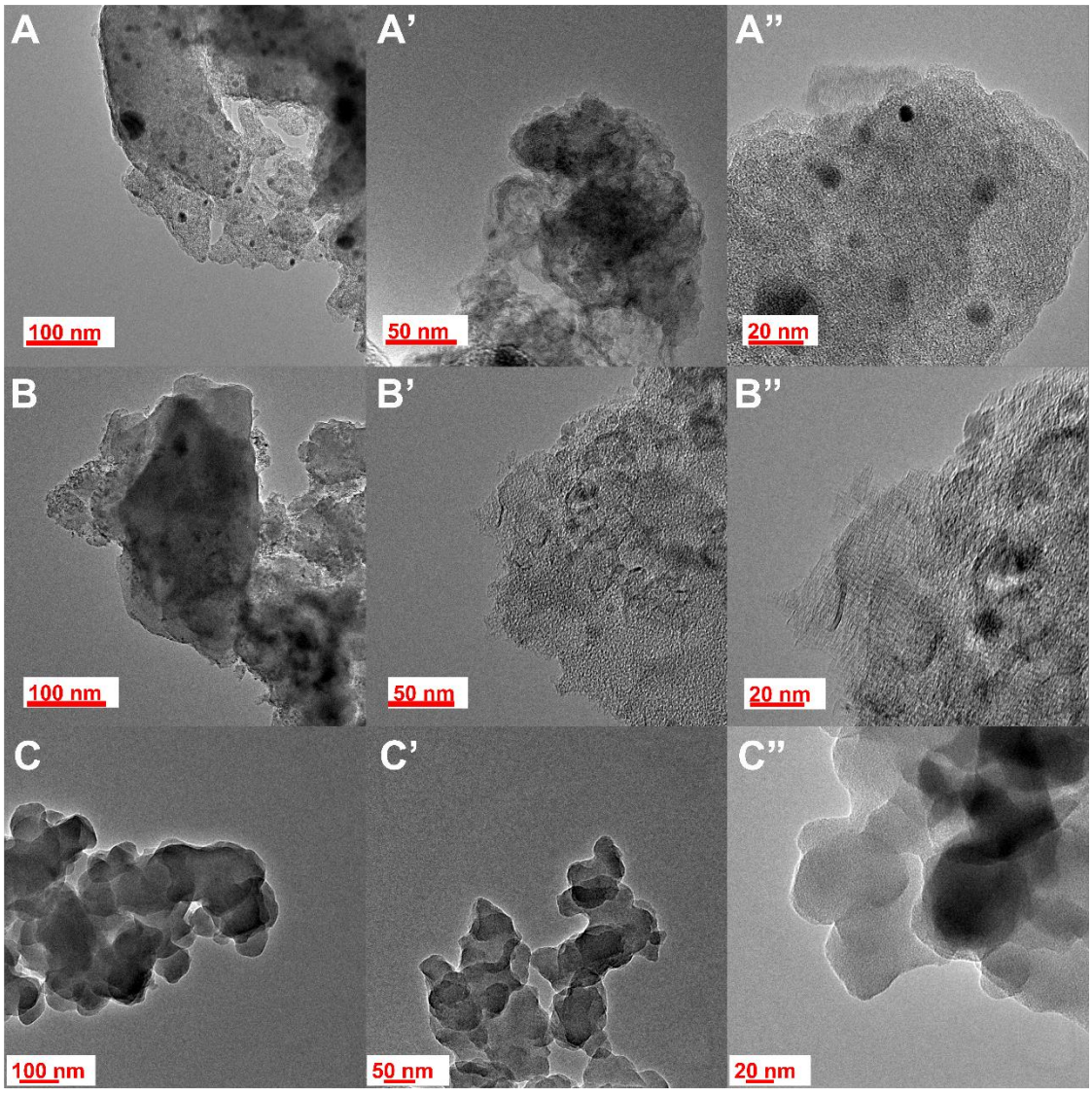

Figure 29. TEM images of carbonized in-situ Ni-funcionalized Al-MOF: Ni(1)-CMOF (A,A',A"), Ni(10)-CMOF (B,B',B") and Ni(100)-CMOF (C,C',C").

Ni(1)-CMOF. However, Ni(100)-CMOF does not exhibit the presence of Ni-NP, indicating that the nickel content did not allow for agglomeration and resulted in excellent dispersion of nickel on the CMOF surface. In Figure 30, a similar pattern is observed for the Co-functionalized CMOF samples. Co:Al ratios of 1:1 and 1:10 show the presence of Co-NP, while the ratio of 1:100 does not. Consequently, it can be concluded that the optimal surface-to-volume ratio of electrocatalytic species is achieved in Co(100)-CMOF and Ni(100)-CMOF. Furthermore, it should be noted that in the case of Ni-functionalized Al-MOF, the porosity of the structures does not exhibit the same characteristics for all Ni ratios. However, in Co-functionalized Al-MOF, porosity is retained in Co(100)-CMOF. In Co(1)-CMOF, numerous empty core-shell structures are observed, indicating porosity. In contrast to cobalt, nickel exhibits a "healing" effect on the carbon matrix, catalyzing

its reconstruction. This observation leads to the conclusion that nickel plays a significant role in facilitating carbon matrix regeneration.

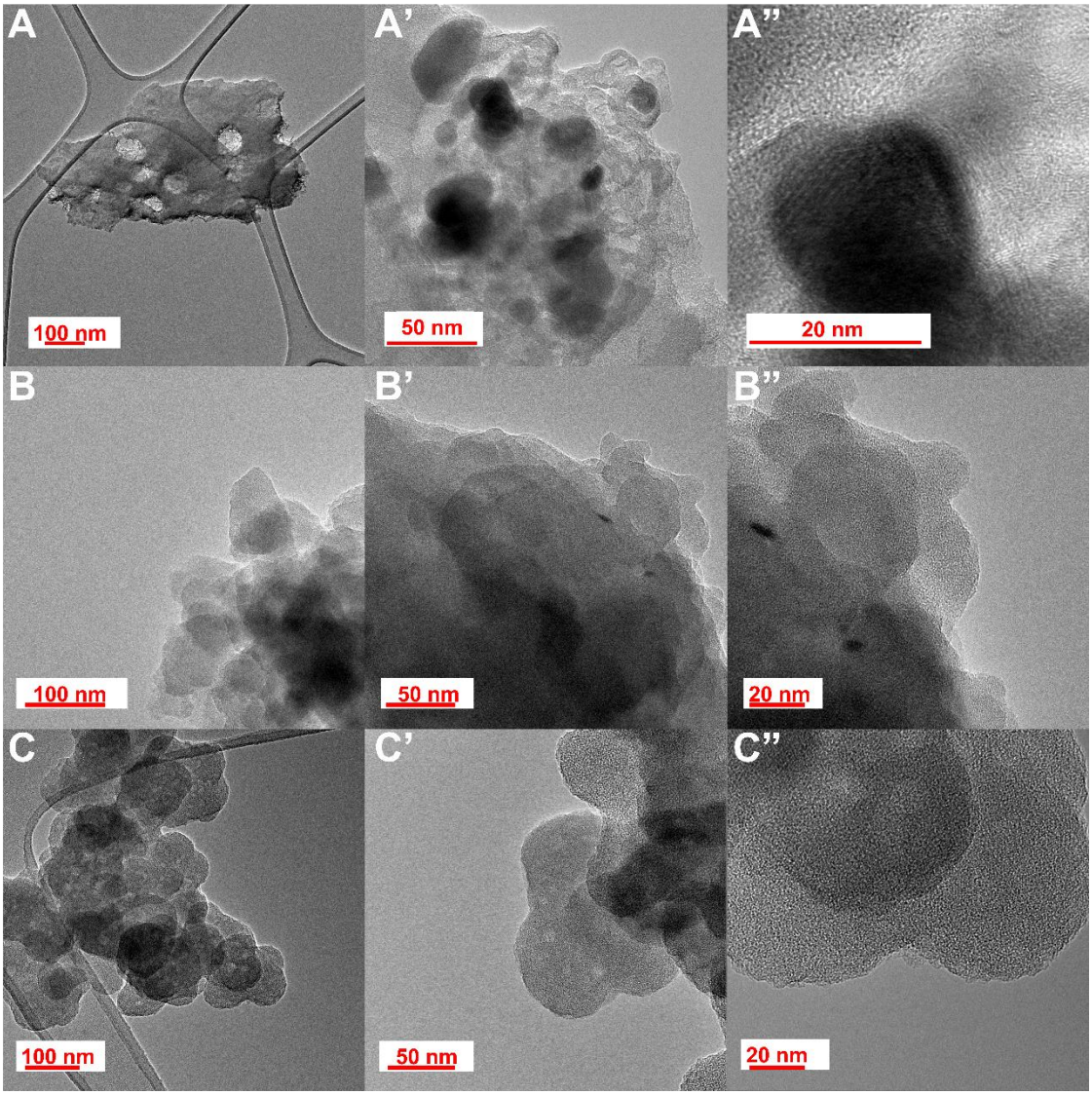

Figure 30. TEM images of carbonized in-situ Co-funcionalized Al-MOF: Co(1)-CMOF (A,A',A"), Co(10)-CMOF (B,B',B") and Co(100)-CMOF (C,C',C").

1.3.2 *Ex-situ* functionalization

An alternative method for incorporating electrocatalytic species into the Al-MOF structure involves their embedding into a carbonized Al-MOF through impregnation - *ex-situ* functionalization (refer to Figure 31). Nevertheless, during the carbonization process, ultrasmall Al-nanoparticles are formed. Consequently, two approaches were investigated: 1) the elimination of aluminium post-carbonization, followed by the introduction of Co into the resulting structure, and 2) the introduction of Co into the carbonized Al-MOF structure directly.

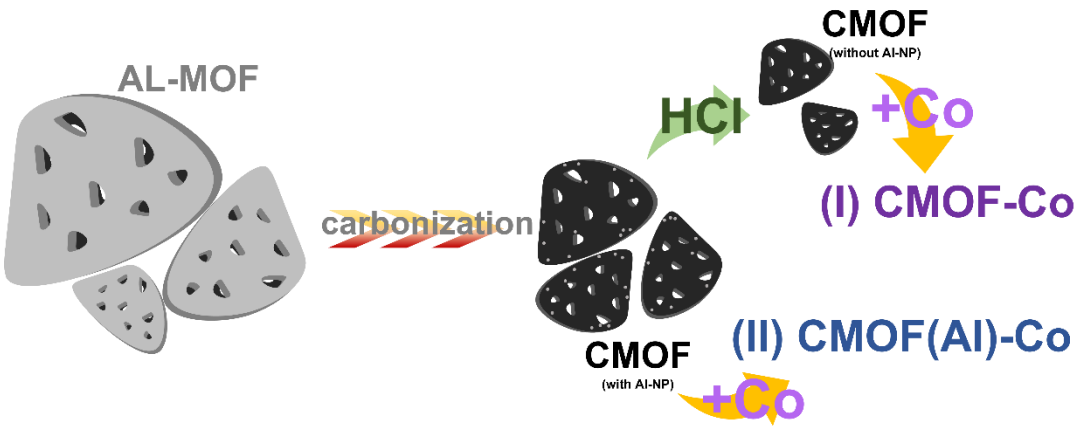

Figure 31. Schematic representation of *ex-situ* functionalization of carbonized Al-MOF (CMOF).

Firstly, the synthesized structures were examined using TEM, as shown in Figure 32. The analysis reveals the presence of Al nanoparticles (Al-NP) in the CMOF(Al)-Co materials, predominantly concentrated along the carbon edges. In contrast, no Al nanoparticles can be observed in the CMOF-Co material, providing compelling evidence that the HCl treatment effectively eliminated residual aluminium. However, cobalt presence cannot be proved via TEM imaging.

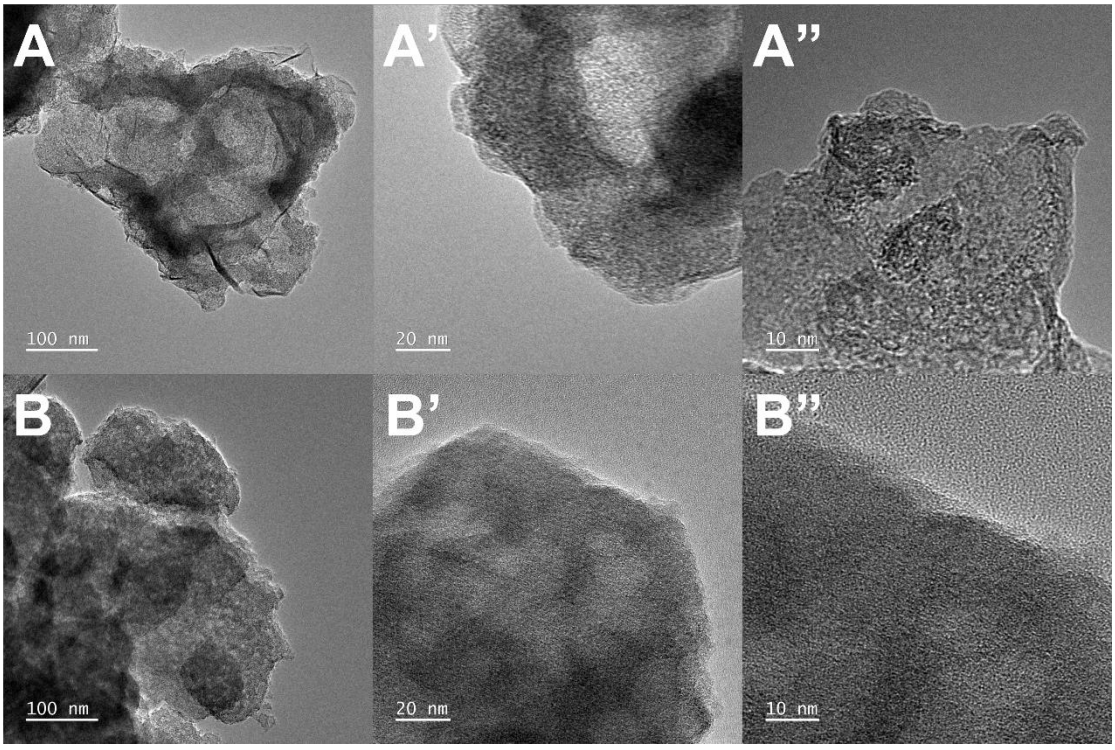

Figure 32. TEM images of CMOF(Al)-Co (A,A',A") and CMOF-Co (B,B',B").

Secondly, to confirm the presence of Co within the functionalized Al-MOF-based structure, energy-dispersive X-ray (EDS) mapping was performed, as illustrated in Figure 33. The elemental analysis reveals carbon (C), oxygen (O), nitrogen (N), and cobalt (Co)

in both materials. Additionally, aluminium (Al) was detected in the CMOF(Al)-Co sample. The analysis provides conclusive evidence of cobalt presence in the materials.

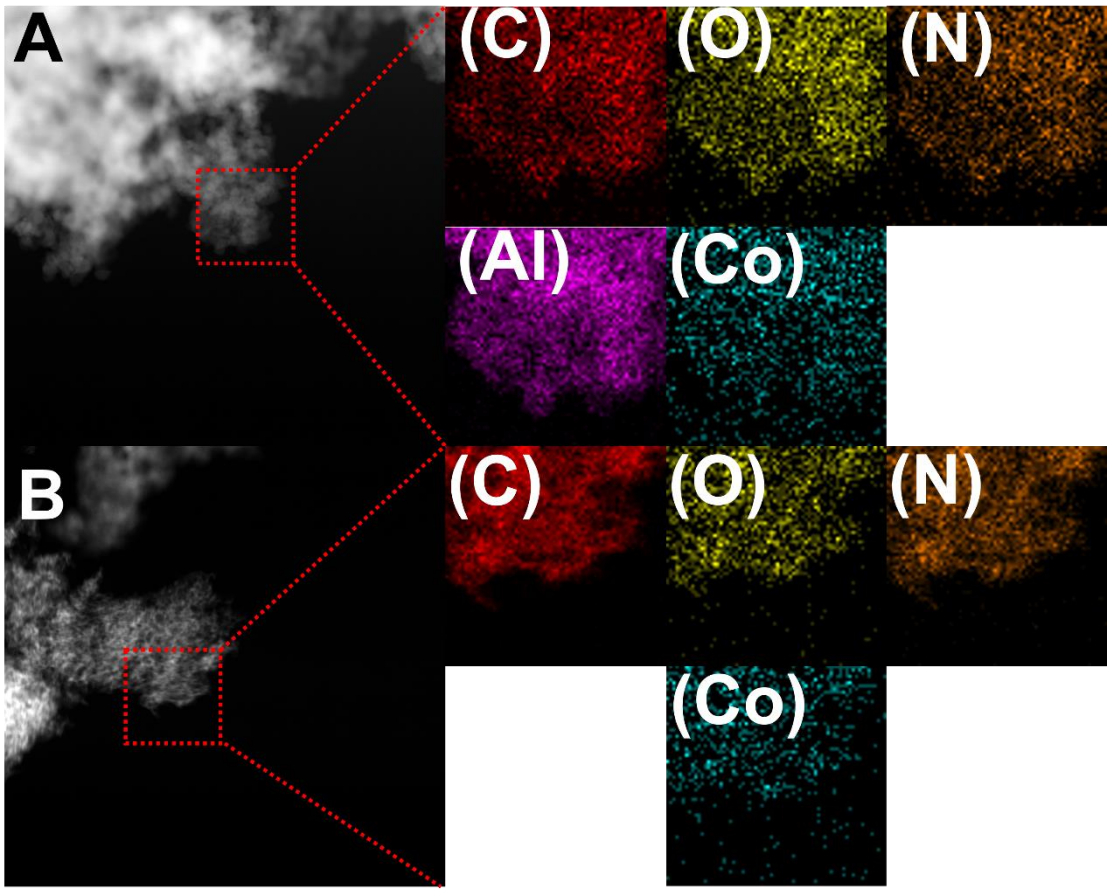

Figure 33. STEM images and EDS elemental mapping of CMOF(Al)-Co (A) and CMOF-Co (B).

To further quantify the cobalt content in the investigated materials, thermal gravimetric analysis (TGA) and X-ray photoelectron spectroscopy (XPS) measurements were performed, as depicted in Figure 34. TGA results indicate that CMOF(Al) aluminium content accounts for approximately 50% of the sample mass. The analysis reveals that cobalt functionalization occurs through different processes, depending on aluminium presence. In the presence of aluminium, cobalt constituted approximately 10% of the sample mass, while in the absence of aluminium (CMOF-Co), it was approximately 6.5% of the sample mass. Although the measurement's precision is limited, it provides a general understanding that aluminium enhances cobalt functionalization. XPS analysis offers valuable insights into atomic interactions within the CMOF(Al)-Co structure. The analysis reveals that aluminium enhances cobalt functionalization through the formation of an Al-Co alloy, leading to increased cobalt content within the material.

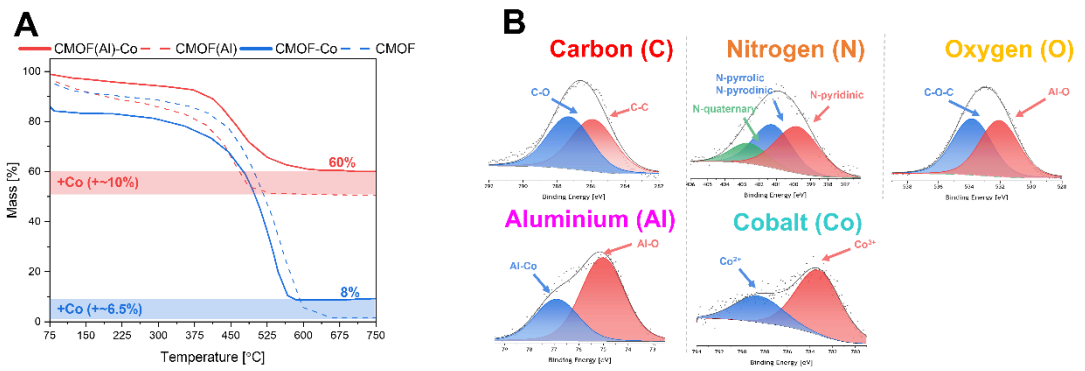

Figure 34. TGA analysis of CMOF(Al)-Co, CMOF(Al), CMOF-Co and CMOF (A) and XPS spectra of CMOF(Al)-Co (B).

1.4 Functionalization of Al-MOF with phosphorus

Al-MOF can be modified through the introduction of metallic species but also non-metallic elements, such as phosphorus. Consequently, after carbonization, a highly efficient structure enriched with nitrogen and phosphorus can be synthesized. Studies have demonstrated that electrochemically active species within the carbon matrix are predominantly non-metals, specifically nitrogen and phosphorus [97–100]. This presents an excellent opportunity to enhance the electrochemical properties of Al-MOF-based structures, highlighting their significant potential for improved performance.

The Al-MOF was immersed in an ethanol solution containing diphenyl chlorophosphate (DPC) at various concentrations, namely 1 mM, 10 mM, 100 mM, and 1000 mM. Following this, Al-MOF was carbonized to obtain phosphorus-doped nitrogen-rich carbon structures, denoted as P-CMOF: 1-P-CMOF, 10-P-CMOF, 100-P-CMOF, and 1000-P-CMOF (Figure 35).

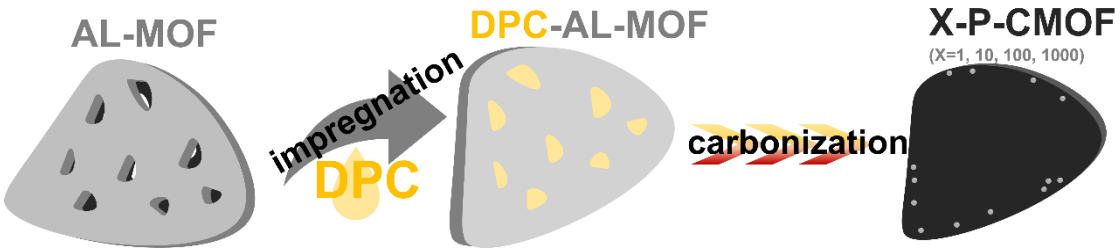

Figure 35. Schematic representation of 1,10,100,1000-P-CMOF synthesis.

TEM analysis (refer to Figure 36) of 1-P-CMOF demonstrated that the incorporation of DPC led to the reconstruction of the porous structure, resulting in a carbon matrix

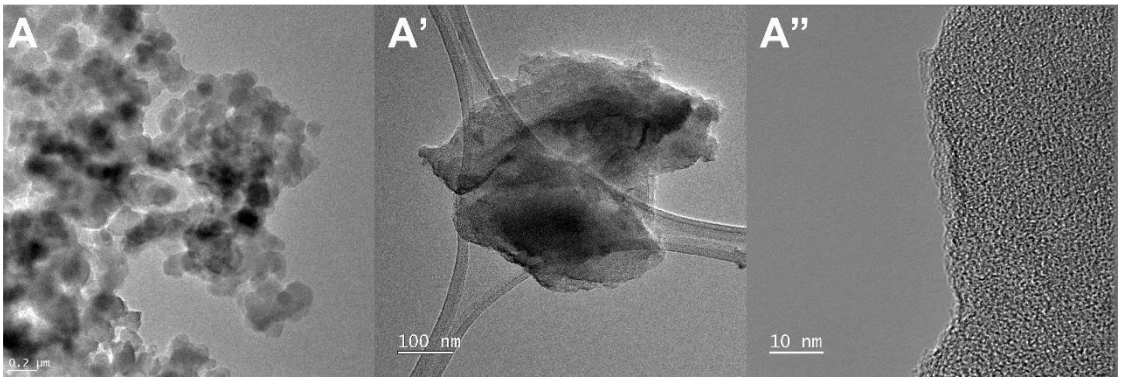

Figure 36. TEM images of 1-P-CMOF.

devoid of Al-MOF pores. The analysis revealed a complete transformation of the original Al-MOF framework, indicating that the DPC treatment effectively modified the material's morphology.

Furthermore, the 1-P-CMOF was treated with HCl to remove aluminium residues – 1-P-CMOF(HCl). Other DPC concentrations were excluded via electrochemical results. Raman spectra (Figure 37A) show that DPC treatment lowered defects in Al-MOF-based structure by lowering the I_D/I_G ratio to 1.29 (CMOF – 1.38). HCl treatment raised this value to 1.48. FTIR analysis (Figure 37B) shows that the P-functionalization of Al-MOF

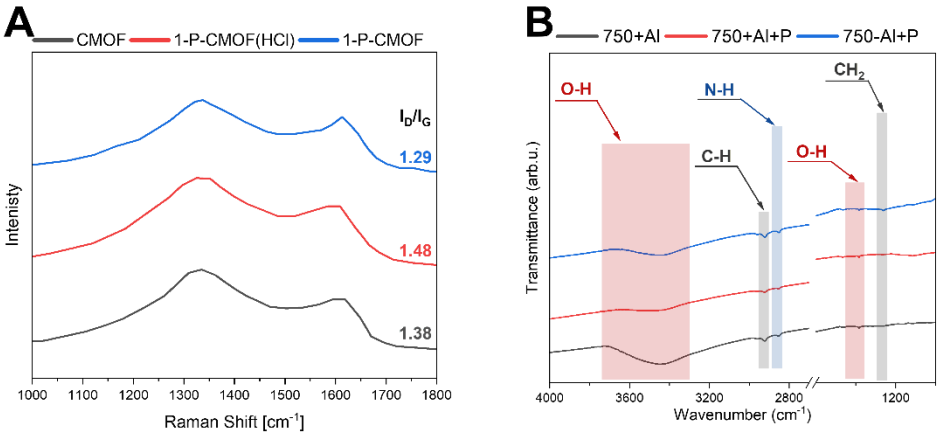

Figure 37. Raman spectra (A) and FTIR (B) of CMOF, 1-P-CMOF and 1-P-CMOF(HCl).

reduces the -OH groups on the surface of the material. XPS analysis provides conclusive evidence regarding the elemental composition and surface bonding characteristics of the investigated materials, as depicted in Figure 38. The obtained spectra for carbon, nitrogen, and aluminium indicate the presence of phosphorus. This phosphorus is embedded within the carbon matrix directly with carbon and nitrogen atoms. Additionally, phosphorus is observed on aluminium surfaces, forming AlP compounds. Furthermore, the oxygen spectrum reveals phosphorus atoms bonded to oxygen. This indicates the formation of

phosphorus-oxygen compounds on the material's surface. These findings are consistently supported by the phosphorus spectrum, confirming the aforementioned observations. Overall, the XPS analysis serves as a valuable tool for elucidating the elemental composition and surface bonding characteristics of the investigated materials. It sheds light on the precise distribution and chemical interactions involving phosphorus within

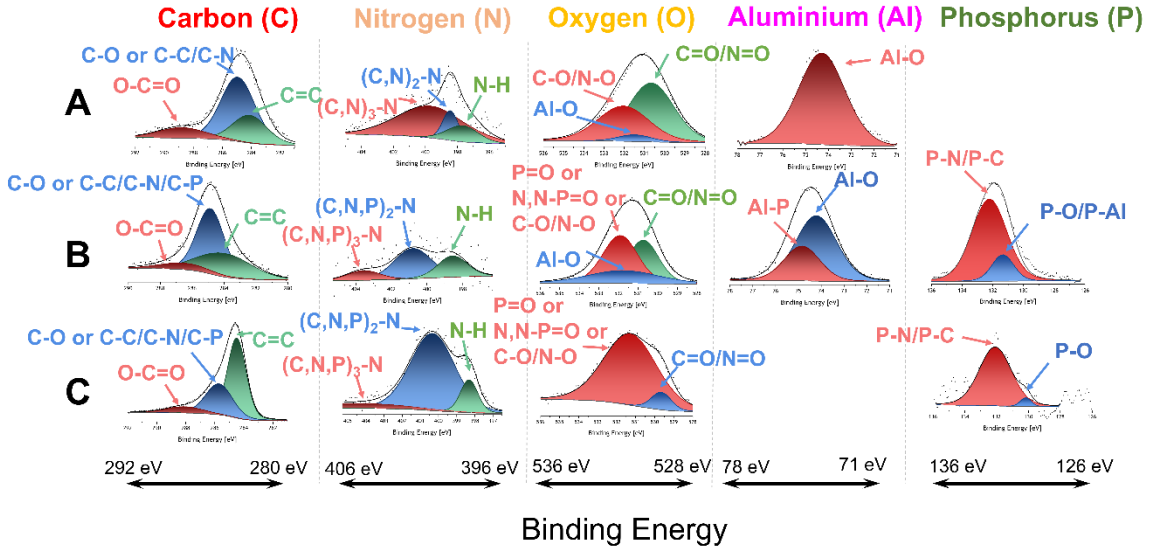

Figure 38. XPS spectra of CMOF (A), 1-P-CMOF (B) and 1-P-CMOF(HCl) (C).

the studied system.

2. Electrochemistry

2.1 HER

2.1.1 Ni-funcionalized CMOF

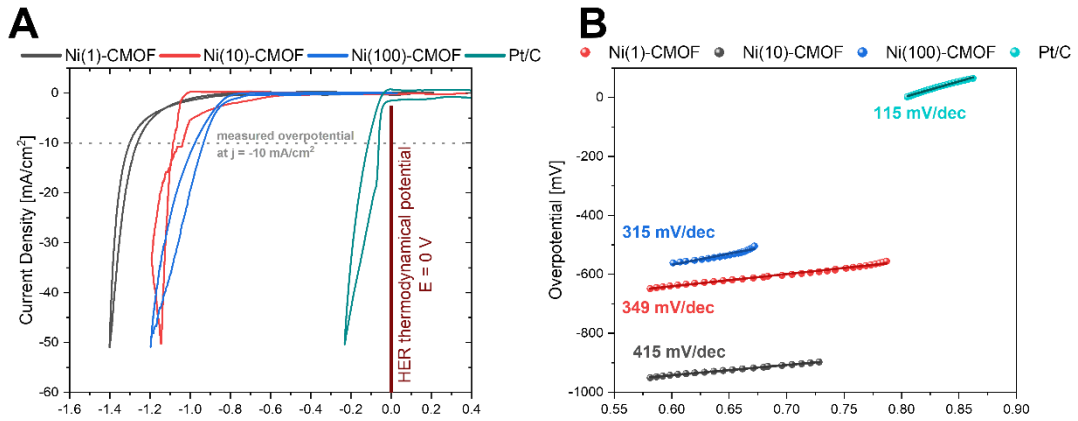

Figure 39. LSV (A) and Tafel slope (B) of Ni(1)-CMOF, Ni(10)-CMOF, NI(100)-CMOF and Pt/C.

Ni-functionalized Al-MOF-based structures were investigated for their electrochemical properties in the hydrogen evolution reaction (HER). Figure 39 presents the results of

linear sweep voltammetry (LSV) and Tafel slope analysis for three different concentrations of Ni in the CMOF framework, namely Ni(1)-CMOF, Ni(10)-CMOF, and Ni(100)-CMOF, compared to a commercial catalyst, platinum deposited on carbon (Pt/C). The LSV plots indicate that Ni(1)-CMOF exhibits the smoothest performance, suggesting that a higher nickel concentration contributes to a smoother electrochemical response. As the amount of electrocatalyst decreases, the overpotential (the difference between the measured potential and the thermodynamic HER value) at -10 mA/cm^2 also decreases. However, even the highest value observed for Ni(100)-CMOF, which is 1000 mV, does not approach the values obtained for Pt-based catalysts (approximately 100 mV). Figure 39B - Tafel slope analysis reflects the kinetics of investigated electrocatalysts. A slope value close to 0 indicates the most efficient electrochemical kinetics. Similar to the LSV results, the relationship between Ni concentration and Tafel slope demonstrates that as nickel concentration decreases, the kinetics improve. Nevertheless, the slope values obtained for the Ni-functionalized Al-MOF-based structures, even the lowest value of 315 mV/dec for Ni(100)-CMOF, are significantly higher than that of Pt/C, which is 115 mV/dec. Therefore, based on the presented form and composites, nickel-functionalized Al-MOF-based structures are not suitable for HER. These structures require further enhancement and development to be viable for HER applications in the future.

2.1.2 Optimization of Ni-based catalyst

To optimize the Ni-based catalyst for HER, an enrichment process involving a nitrogen-rich source was implemented before carbonization. The influence of increased nitrogen content on the catalyst composition was evaluated through LSV measurements, as depicted in Figure 40A. Furthermore, the impact of electrode material was investigated to assess catalyst performance on different surfaces, as illustrated in Figure 40B. Specifically, the conventional graphite film electrode was substituted for a more innovative carbon foam electrode.

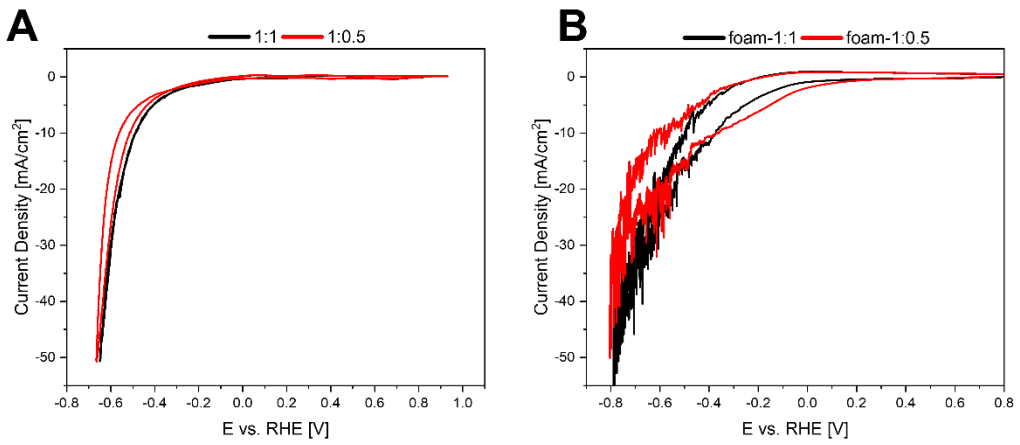

Figure 40. HER measurement via LSV of N-doped Ni(100)-CMOF with a ratio of Ni(100)-CMOF:CA - 1:1 and 1:0.5 (A) and measurement for same materials on carbon foam (B).

The introduction of N-doping in Ni(100)-CMOF resulted in a noticeable reduction in overpotential, with values of 500 mV (for a 1:0.5 ratio) and 480 mV (for a 1:1 ratio), in contrast to the overpotential of 1000 mV observed in Ni(100)-CMOF. This indicates that a higher nitrogen content enhances HER performance. However, increasing the cyanamide (CA) ratio to 1:1 slightly affects performance. Additionally, substituting graphite foil with carbon foam further enhances the HER performance of the catalyst. This leads to lower overpotential values of 360 mV and 340 mV for 1:0.5 and 1:1 ratios, respectively. It is imperative to note that despite the reduction in overpotential, the durability and kinetics of the catalyst suffer, resulting in the detachment of the electrocatalyst. These modifications have demonstrated improvements in HER overpotential performance. However, further advancements are necessary to enhance the durability of the materials involved.

To optimize the catalyst, the focus was placed on the Ni-source used in the catalyst. Various Ni-salts were tested following the same procedure as the $Ni(NO_3)_2$-

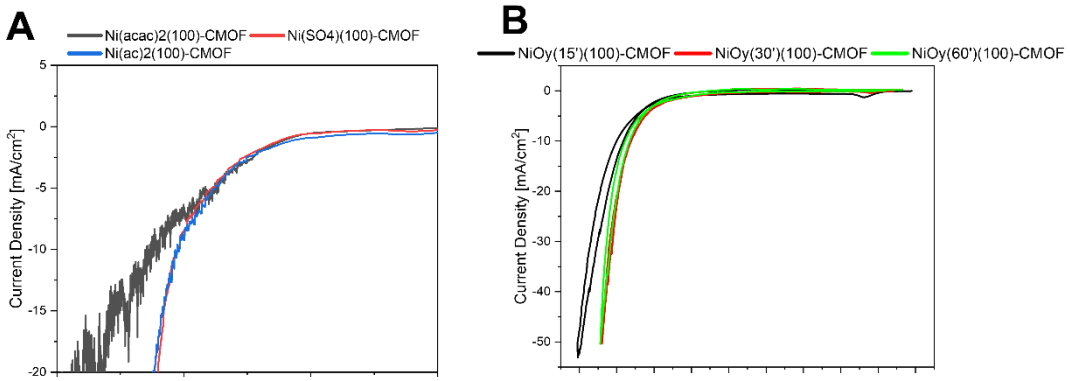

Figure 41. HER performance investigated through LSV for different nickel sources (A) and time of Ni(100)-CMOF surface oxidation (B).

based catalyst. The performance of these catalysts in HER was evaluated using the same methodology. Their performance was estimated through LSV, as depicted in Figure 41A. Additionally, another optimization approach involved surface oxidation. The Ni(100)-CMOF electrocatalyst was subjected to an oxygen atmosphere at elevated temperatures for a specified duration, as illustrated in Figure 41B. This oxidation process was aimed at improving catalyst performance and is presented for analysis.

To investigate the impact of different nickel salts on HER performance, various salts were employed, namely nickel(II) acetoacetate ($Ni(acac)_2$), nickel(II) sulfate(VI) ($NiSO_4$), and nickel(II) acetate ($Ni(ac)_2$). These salts were processed like Ni(100)-CMOF. The measured overpotential values were 650 mV for $Ni(acac)_2$ and 530 mV for both $NiSO_4$ and $Ni(ac)_2$ functionalized CMOF. While these overpotential values were successfully reduced compared to Ni(100)-CMOF, they were still considerably higher than those observed for Pt/C catalysts. Additionally, the $Ni(acac)_2$(100)-CMOF catalyst exhibited extremely sluggish reaction kinetics, indicating significant retardation in the system. Furthermore, the Ni(100)-CMOF catalyst underwent surface oxidation at elevated temperatures, resulting in oxidized Ni(100)-CMOF variants denoted as NiO_y(15')(100)-CMOF, NiO_y(30')(100)-CMOF, and NiO_y(60')(100)-CMOF. These variants exhibited overpotential values of 570 mV, 520 mV, and 530 mV, respectively. These results indicate that surface oxidation improves Ni(100)-CMOF HER performance, leading to a more effective electrocatalyst. However, even with these improvements, the electrocatalyst still falls short of Pt/C in HER performance. In summary, the utilization of different nickel salts and the surface oxidation of Ni(100)-CMOF demonstrated enhancements in HER performance. Nevertheless, the catalysts studied in this investigation remain insufficient to surpass Pt/C catalysts in the hydrogen evolution reaction.

2.1.3 Co-funcionalized CMOF

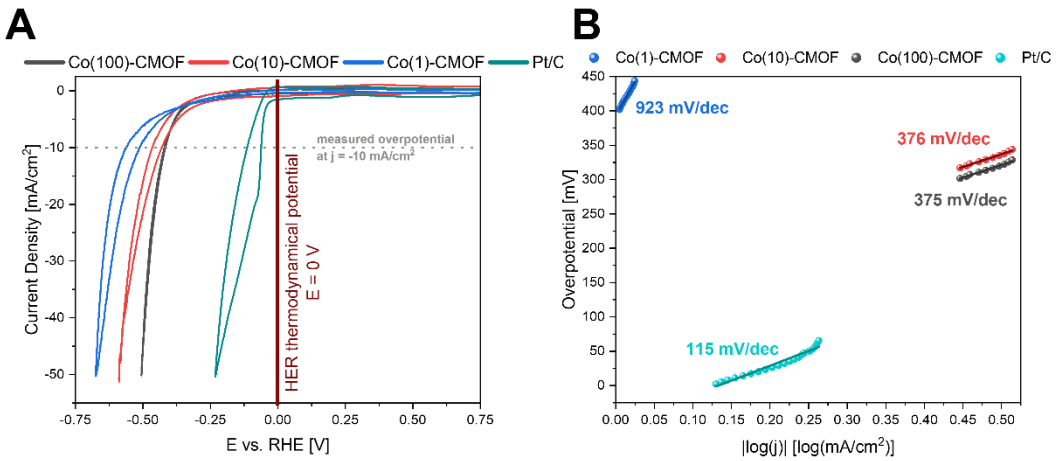

Figure 42. LSV (A) and Tafel slope (B) of Ni(1)-CMOF, Ni(10)-CMOF, NI(100)-CMOF and Pt/C.

The electrochemical properties of Al-MOF-derived structures functionalized with cobalt (Co) were examined for their efficacy in the HER. Figure 42 presents the results of LSV and Tafel slope analysis for Co(1)-CMOF, Co(10)-CMOF, and Co(100)-CMOF, in comparison to the commercial catalyst Pt/C. Interestingly, cobalt-based composites exhibited lower overpotential values than their nickel-containing counterparts. All composites show smooth LSV curves (Figure 42A) As the amount of electrocatalyst decreased, the overpotential at -10 mA/cm^2 also decreased. However, the overpotential values for Co(100)-CMOF, even at their highest performance of 470 mV, did not reach the levels achieved by Pt-based catalysts (~100 mV). On the other hand, the electrocatalyst kinetics followed a different pattern. The Tafel slope analysis in Figure 42B revealed that nickel-based structures exhibited better kinetics than cobalt-based composites. The Tafel slope, which reflects electrochemical kinetics, was lower for nickel-based structures. A lower slope value indicates improved electrochemical properties. Despite higher overpotentials, nickel-based structures demonstrated superior kinetics compared to cobalt-based composites. In conclusion, the cobalt-functionalized Al-MOF-based structures displayed lower overpotentials than their nickel-based counterparts. However, the nickel-based structures exhibited better kinetics. These findings underscore the need for further optimization and development of both cobalt and nickel-based composites to enhance their suitability for applications in the HER. Both functionalized Al-MOF-based composites show that decreasing the amount of catalyst is a good direction for optimizing the electrochemical properties of functionalization.

2.1.4 Pt-funcionalized CMOF

To investigate low-content platinum-based electrocatalyst, two different Pt sources - chloroplatinic acid (H_2PtCl_4) and platinum(II) acetylacetonate ($Pt(acac)_2$) were synthesized in the same manner as Ni(100)-CMOF. LSV measurement is presented in Figure 43A while in Figure 43B Tafel slope is presented.

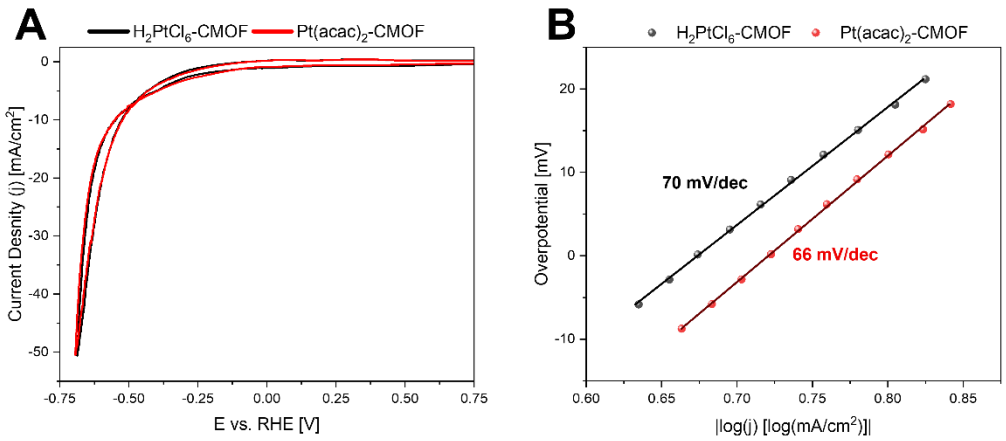

Figure 43. LSV (A) and Tafel slope (B) of Pt-funcionalized CMOF with 2 different platinum sources.

The LSV plots of both platinum sources demonstrate an identical overpotential of 527 mV in the HER reaction, which is five times higher than that observed with commercial Pt/C. However, when considering the Tafel slope for both Pt sources, it becomes apparent that the kinetics of these materials are smoother compared to commercial Pt/C. Specifically, $Pt(acac)_2$-CMOF exhibits the lowest Tafel slope of 66 mV/dec, followed by H_2PtCl_6-CMOF with a Tafel slope of 70 mV/dec, while commercial Pt/C demonstrates a higher Tafel slope of 115 mV/dec. This indicates that CMOF has a potential for smooth kinetics of HER, however, some further improvements for the materials are required to lower the overpotential.

Two distinct strategies were investigated to enhance the overpotential in the present study. The first approach involved the synthesis of a Pt-Ni co-catalyst, following the same procedure as the Ni(100)-CMOF, with a Pt:Ni ratio of 1:1. Two different platinum sources were employed in this synthetic process. The obtained LSV plot for this investigation is depicted in Figure 44A. The second approach focused on introducing a different gas mixture (10% NH_3: 90% N_2) during the carbonization process for the aforementioned materials. The resulting LSV plot for this particular investigation is presented in Figure 44B.

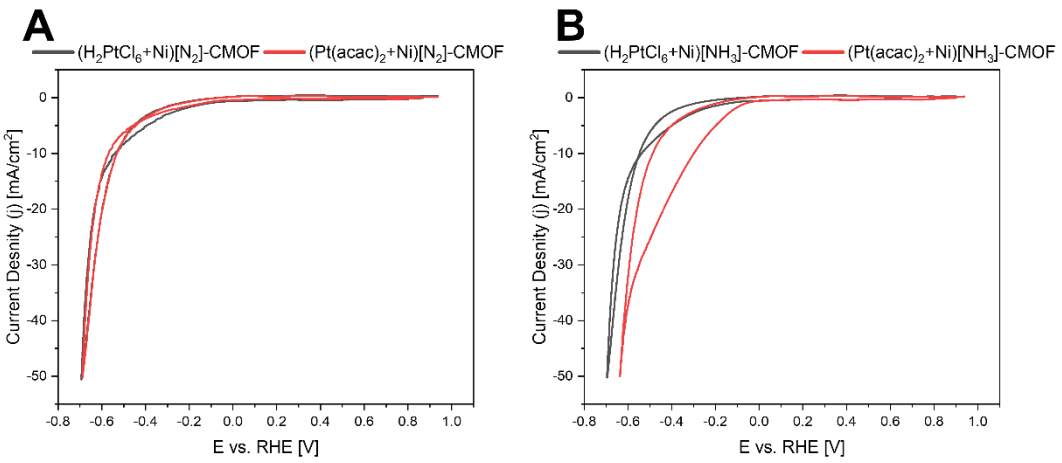

Figure 44. LSV plot of Pt-Ni-CMOF carbonized in nitrogen (A) and nitrogen+ammonium (B).

The LSV plots of Pt-Ni-CMOF carbonized under a nitrogen atmosphere, reveal an identical overpotential of 527 mV, which is five times higher than that of commercial Pt/C. However, when the carbonization process is conducted in a nitrogen and ammonium atmosphere (as shown in Figure 44B), (H_2PtCl_6+Ni)[NH_3]-CMOF exhibits a slight increase in overpotential to 536 mV, whereas (Pt(acac)$_2$+Ni)[NH_3]-CMOF demonstrates a significant improvement in HER performance, achieving an overpotential of 300 mV. Nevertheless, these improvements are still not comparable to Pt/C, a commercially available electrocatalyst.

In summary, the PT-functionalized CMOF electrocatalyst materials presented herein exhibit potential for application in the HER process. However, there are several obstacles to overcome, especially the high overpotential. Although the Pt-CMOF catalyst utilizing expensive platinum has achieved a certain level of performance, the Ni-CMOF catalyst has the potential to reach a similar level, offering a more cost-effective alternative.

2.2 OER

2.1.1 *In-situ* funcionalized CMOF

The electrochemical performance of *in-situ* functionalized Al-MOF-based structures, incorporating both cobalt and nickel, was investigated for the oxygen evolution reaction (OER), as illustrated in Figure 45. The results revealed overpotential values for each material. Among the nickel-functionalized composites, Ni(1)-CMOF exhibited the highest overpotential of 500 mV, while Ni(100)-CMOF showed a slightly lower overpotential of 470 mV. Similarly, for the cobalt-functionalized composites,

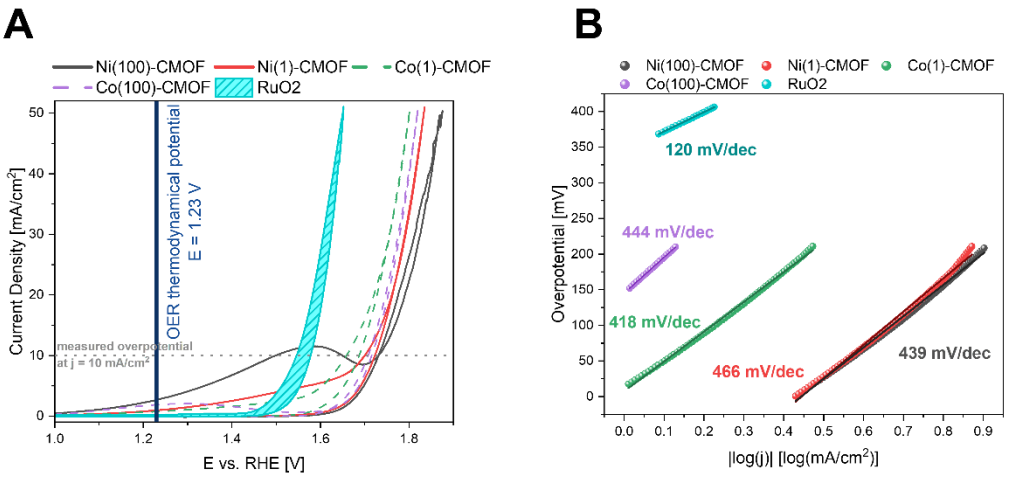

Figure 45. LSV (A) and Tafel slope (B) of Ni(1)-CMOF, Ni(100)-CMOF, Co(1)-CMOF, Co(100)-CMOF and RuO_2.

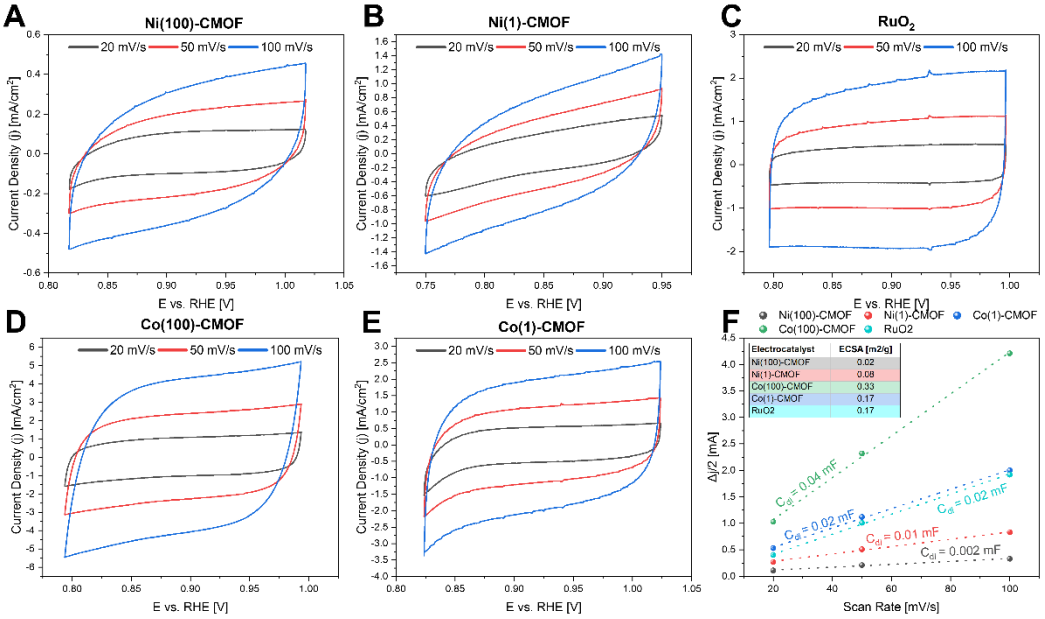

Figure 46. CV measurements of Ni(100)-CMOF (A), Ni(1)-CMOF (B), RuO_2 (C), Co(100)-CMOF (D), Co(1)-CMOF (E) and linear regression between the current density differences in the middle of the potential window of CV vs. scan rates (F) with calculated ECSA (inset).

Co(1)-CMOF demonstrated an overpotential of 470 mV, while Co(100)-CMOF demonstrated a slightly reduced overpotential of 450 mV. It is significant to note that both the nickel and cobalt-functionalized materials displayed significantly higher overpotential values than the reference material, ruthenium oxide (RuO_2), which showed an overpotential of 350 mV. Overall, the investigation of *in-situ* functionalized Al-MOF-based structures incorporating both cobalt and nickel for the OER demonstrated that the nickel-functionalized composites exhibited higher overpotentials than the cobalt-functionalized ones. Furthermore, all functionalized materials displayed considerably higher overpotential values compared to the reference material, ruthenium oxide. Additionally, it was observed that both Co(1)-CMOF and Ni(1)-CMOF exhibited

prominent oxidation peaks during the linear sweep voltammetry (LSV) analysis. The Tafel slope analysis provided insights into these materials' electrochemical kinetics. Co(1)-CMOF demonstrated the most favourable kinetics, with a Tafel slope value of 418 mV/dec. However, it is worth noting that achieving the kinetics level of ruthenium oxide (120 mV/dec) remains a challenging task. In contrast, the Ni-functionalized CMOF displayed a higher Tafel slope, which combined with its elevated overpotential, renders it unsuitable for the OER. Like the HER results, the in-situ functionalization approach still has room for improvement in terms of improving electrocatalytic performance.

The cyclic voltammetry (CV) plots depicted in Figure 46 were utilized to calculate the double-layer capacitance (C_{dl}) employing a linear fitting slope (Figure 46F). The determined C_{dl} values enabled the assessment of the electrochemically active surface area (ECSA) for Ni(100)-CMOF, Ni(1)-CMOF, Co(100)-CMOF, Co(1)-CMOF, and RuO_2. The analysis revealed that Co(100)-CMOF exhibits the largest ECSA of 0.33 m^2/g, which is twice as large as that of RuO_2 (0.17 m^2/g). On the other hand, Ni(100)-CMOF displayed the lowest ECSA – 0.02 m^2/g, indicating that the limited amount of nickel is not suitable for the oxygen evolution reaction, resulting in a minimal contribution of the surface area to the reaction.

Overall, the study highlights that although Co(1)-CMOF exhibited promising kinetics, surpassing ruthenium oxide performance remains a challenge. Furthermore, the Ni-functionalized CMOF exhibited unfavourable kinetics and high overpotential followed by low ECSA value, underscoring the need for further development and optimization of the in-situ functionalization technique to enhance the electrocatalyst's performance in both HER and OER applications.

2.1.2 *Ex-situ* Co-funcionalized CMOF

The functionalization of Al-MOF-based structures after carbonization offers significant advantages as it avoids any interaction with the support structure, which is formed during the carbonization process. Therefore, the key step for *ex-situ* functionalization is thermal treatment and Co concentration. Initially, the impact of carbonization on thermal treatment, as shown in Figure 47A, was investigated. Initially, as the temperature increases, the overpotential decreases. However, upon reaching 450˚C, the structure collapses and undergoes thermally induced decomposition, resulting in a significant increase in overpotential. Additionally, the carbon structure undergoes structural changes. Subsequently, as the temperature rises, the overpotential decreases

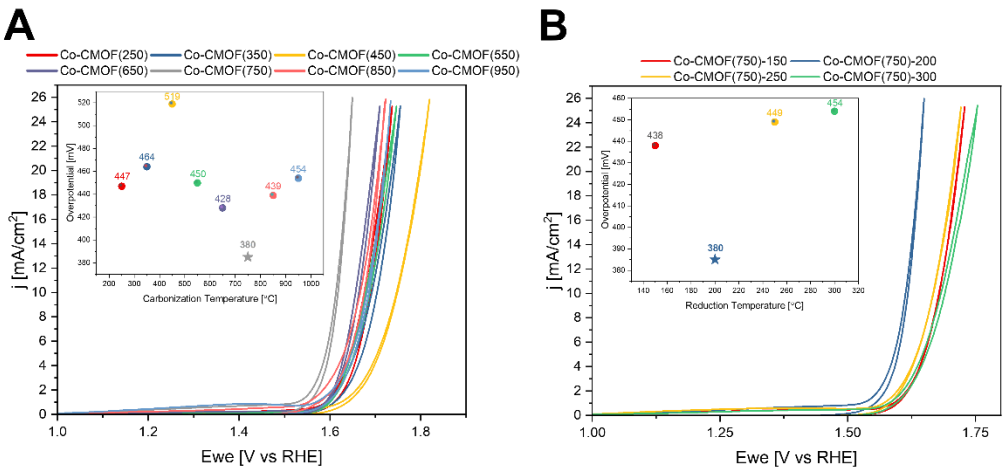

Figure 47. LSV result of Co-funcionalized Al-MOF-based structures treated with different temperatures (A) and different reduction temperatures of Co-salt in CMOF(750) (B).

again, reaching its minimum value of 380 mV for Co-CMOF(750). Following this, the overpotential increases again. This behaviour can be attributed to the formation of a core-shell structure consisting of aluminium and carbon, as well as a higher degree of graphitization.

Another crucial parameter associated with the temperature regime is the temperature at which cobalt salt reduction/decommissioning occurs in a hydrogen atmosphere, as depicted in Figure 47B. Four different temperatures ranging from 150˚C to 300˚C were examined for CMOF(750). Notably, the lowest overpotential value of 380 mV was achieved at 200˚C. This parameter highlights the significance of the reduction in temperature on the electrochemical performance of the system. By carefully selecting the appropriate temperature, the overpotential can be effectively minimized. This leads to improved efficiency and performance of the cobalt salt reduction process in the hydrogen atmosphere. The experimental findings emphasize the importance of optimizing the reduction temperature for achieving desirable electrochemical properties in the context of functionalizing Al-MOF-based structures after carbonization.

Cobalt concentration from 1 mM to 100 mM was investigated via LSV to estimate the optimal concentration of Co in Co-CMOF composite (see Figure 48). As illustrated in Figure 48, the composites with cobalt salt concentrations of 1 mM and 1 M exhibit the lowest overpotentials, measuring 380 mV and 390 mV, respectively. Following closely, the composite with a cobalt salt concentration of 100 mM demonstrates an overpotential of 410 mV, while the highest overpotential of 500 mV is observed for the composite with a concentration of 10 mM. Hence, the optimal cobalt salt concentrations, in terms of minimizing overpotential, lie at the highest and lowest levels. However, it should be noted that the lowest concentration of 1 mM does not involve an excess of cobalt concerning the surface-to-volume ratio. Therefore, the most efficient material, considering both the lowest overpotential and optimal cobalt concentration, is composite with a cobalt salt

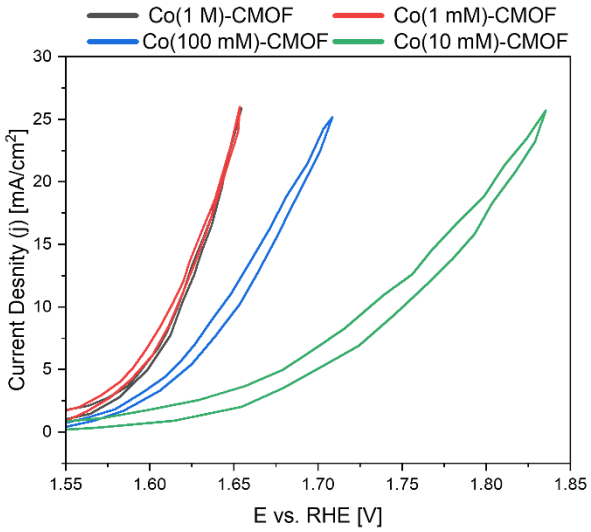

Figure 48. LSV measurement for different cobalt concentrations (1 mM, 10 mM, 100 mM and 1 M) in ex-situ funcionalized Co-CMOF.

concentration of 1 mM.

The optimized structure of Co-CMOF(750), reduced at 200˚C in a hydrogen atmosphere with a cobalt concentration of 1 mM, was further investigated to elucidate its low overpotential of 380 mV. A comparative analysis was conducted by considering two variations: one with aluminium (CMOF-Co(Al)) and another without aluminium (CMOF-Co). The cobalt-functionalized structures were prepared using optimized parameters and subjected to various characterization techniques, including LSV, Tafel slope analysis, electrochemical impedance spectroscopy (EIS), and stability measurements. These results were compared with those obtained for ruthenium oxide. Figure 49 illustrates the LSV measurement and Tafel slope analysis. The LSV curves demonstrate that CMOF-Co(Al) achieved an overpotential level comparable to ruthenium

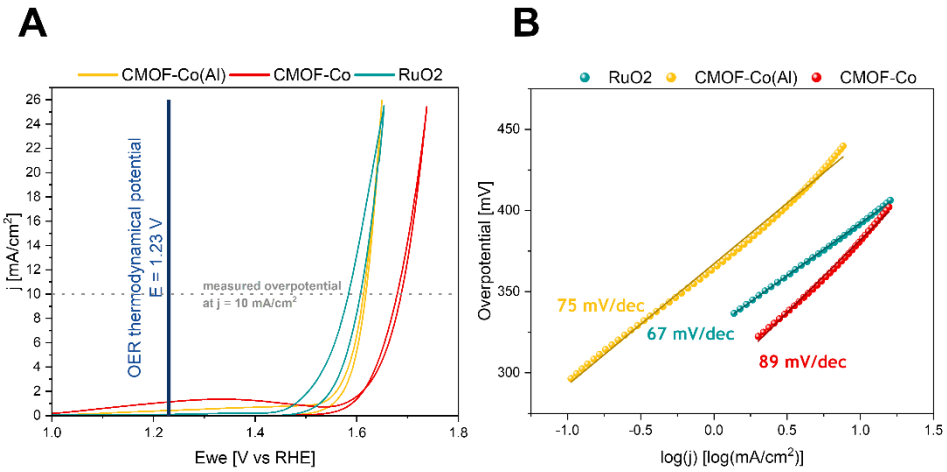

Figure 49. LSV (A) and Tafel slope results of CMOF-Co(Al), CMOF-Co and RuO_2.

oxide, at 380 mV and 350 mV, respectively. In contrast, CMOF-Co exhibited a significantly higher overpotential of 450 mV. These findings strongly suggest that aluminium is crucial to maintaining a low overpotential during OER. Furthermore, the Tafel slope results corroborate the LSV findings, revealing that RuO_2 exhibited the lowest slope of 67 mV/dec. CMOF-Co(Al) displayed a slightly higher slope of 75 mV/dec, while CMOF-Co displayed a higher slope of 89 mV/dec. This indicates that the presence of aluminium not only contributes to the reduction of overpotential but also enhances the kinetics of the OER. This boosts the cobalt-based catalyst's overall performance. These results collectively demonstrate the superior electrochemical performance and stability of the optimized Co-CMOF(750) structure, especially when aluminium is present. The incorporation of aluminium not only enables a low overpotential but also improves catalytic kinetics, making it a promising candidate for applications requiring an efficient cobalt-based electrocatalyst.

Figure 50 illustrates the CV plots for CMOF-Co(Al) and CMOF-Co. In Figure 50C, the slope of the linearly fitted Δj/2 versus scan rate is presented, along with the

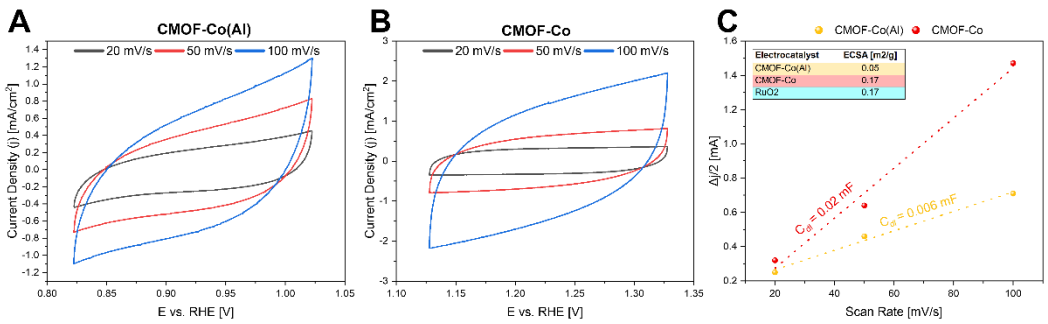

Figure 50. CV plots of CMOF-Co(Al) (A), CMOF-Co (B) and linear regression between the current density differences in the middle of the potential window of CV vs. scan rates (C) with calculated ECSA (inset).

calculated double-layer capacitance. These parameters were utilized to determine the electrochemically active surface area of the investigated materials. CMOF-Co(Al) exhibited a significantly lower ECSA value of 0.05 m^2/g, which is three times smaller than that of CMOF-Co and RuO_2, both measuring 0.17 m^2/g. This observation suggests that efficient utilization of the CMOF-Co(Al) material occurs only on a small portion of the total surface. It is noteworthy that treatment with hydrochloric acid increased the ECSA value; however, this process also resulted in the removal of aluminium, leading to an increase in overpotential.

To gain further insights into the remarkable electrochemical performance and better comprehend the oxygen evolution reaction mechanism for the electrocatalyst, additional measurements including EIS and durability tests were conducted and are presented in Figure 51. The EIS measurements revealed that aluminium significantly reduced the system resistance for CMOF-Co(Al) to R1 = 0.89, compared to CMOF-Co with R1 = 1.97 Ω and RuO_2 with R1 = 0.95 Ω. The resistance corresponding to the reaction kinetics, R2, was measured at 2.82 Ω, 2.62 Ω, and 3.7 Ω for CMOF-Co(Al), CMOF-Co, and RuO_2, respectively. These results indicate that low resistances indicate a strong potential for the cobalt-functionalized Al-MOF-based catalyst to overcome electrochemical obstacles encountered by ruthenium oxide. Furthermore, the durability test demonstrated that CMOF-Co(Al) exhibited the highest resistance to the constant current applied to the material, without a significant increase in the measured potential. On the other hand, the material without aluminium, CMOF-Co, showed a slight increase in potential at 20 mA/cm^2, indicating degradation. Both composites demonstrated

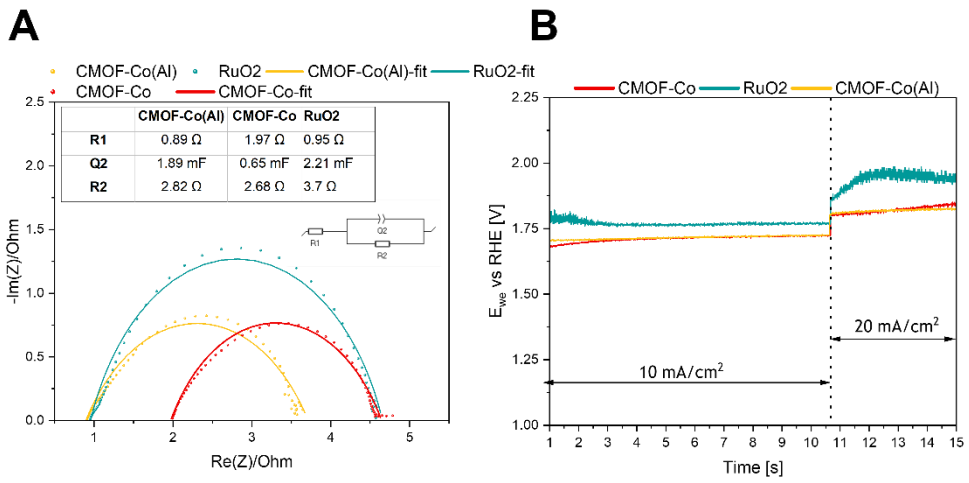

Figure 51. EIS results (A) with electric circuit equivalent (inset) and durability results (B) for CMOF-Co(Al), CMOF-Co and RuO_2.

superior stability compared to RuO_2. RuO_2 displayed a significant increase in potential response to the applied current, highlighting the high instability of the ruthenium oxide electrocatalyst.

In summary, the electrochemical results suggest that Al-MOF carbonized at 750˚C, functionalized with cobalt afterwards, and reduced at 200˚C under a hydrogen atmosphere, without removing the aluminium, serves as an efficient and durable catalyst for the oxygen evolution reaction. This catalyst can compete with ruthenium oxide. The combination of excellent electrochemical performance, low resistance, and superior stability positions the cobalt-functionalized Al-MOF-based catalyst as a promising alternative to conventional ruthenium oxide catalysts for OER applications.

2.1.3 P-doped CMOF

An alternative approach to enhancing Al-MOF-based electrocatalysts is through the introduction of non-metallic atoms, such as phosphorus, into the carbon structure. Phosphorus' attraction to nitrogen-carbon sites within the carbon matrix further contributes to its advantageous use. Previous studies estimated optimized Al-MOF carbonization parameters, which were applied to phosphorus doping of Al-MOF-based structures. Figure 52A depicts the results of LSV for phosphorus-doped CMOF with aluminium (P-CMOF(Al)), phosphorus-doped CMOF without aluminium (P-CMOF), and RuO_2 as the reference material. Among these, P-CMOF(Al) exhibited the lowest overpotential of 390 mV, while P-CMOF showed an overpotential of 510 mV. Consequently, the aluminium material displayed a significantly lower overpotential, similar to RuO_2 (350 mV). Figure 52B provides insights into the kinetics of the investigated electrocatalysts. The reference material showed a slope of 67 mV/dec, whereas P-CMOF(Al) demonstrated a slope of 103 mV/dec, and P-CMOF demonstrated a higher slope of 222 mV/dec. This indicates that despite similar overpotential values to those presented by Co-functionalized CMOF, phosphorus-doped materials have more challenging kinetics. The durability test in Figure 52C reveals that both P-CMOF(Al) and P-CMOF demonstrate a decrease in potential over time when subjected to a current density of 10 mA/cm^2, suggesting activation of the material. In contrast, RuO_2 remained stable. Upon increasing the current density to 20 mA/cm^2, both phosphorus-doped materials displayed an increase in voltage that continued to rise steadily, while RuO_2 remained stable. These findings indicate that P-doped materials lack substantial resistance to current density changes. The EIS measurement results in Figure 52D demonstrate that

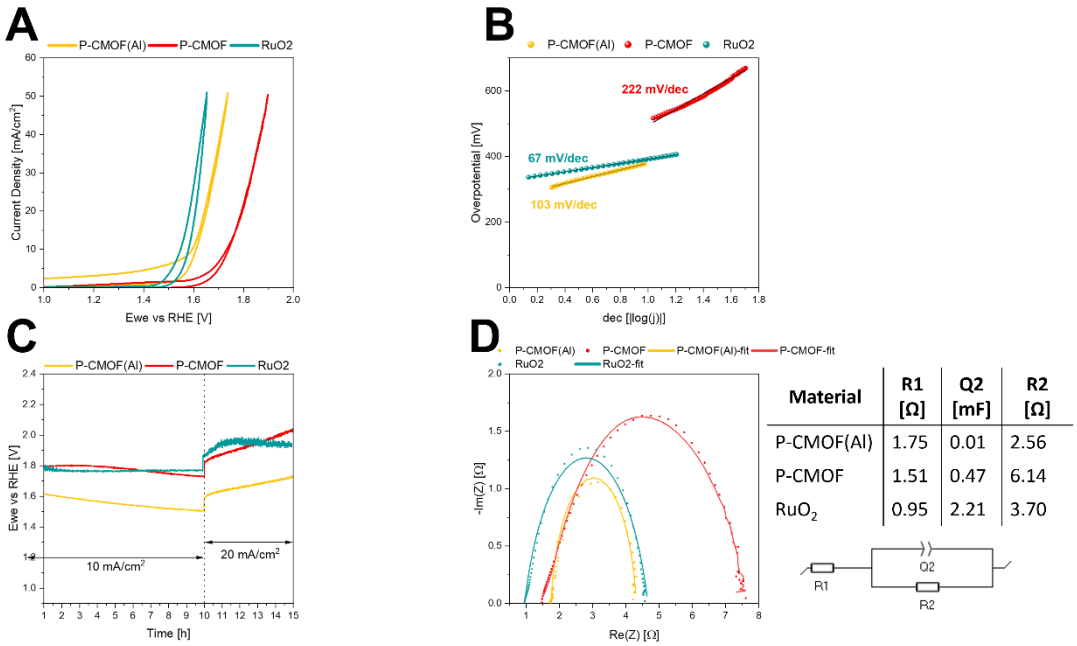

Material	R1 [Ω]	Q2 [mF]	R2 [Ω]
P-CMOF(Al)	1.75	0.01	2.56
P-CMOF	1.51	0.47	6.14
RuO_2	0.95	2.21	3.70

Figure 52. LSV results (A), Tafel slope (B), stability measurement (C) and EIS (D) with a scheme of an electrical circuit for P-CMOF(Al), P-CMOF and RuO_2.

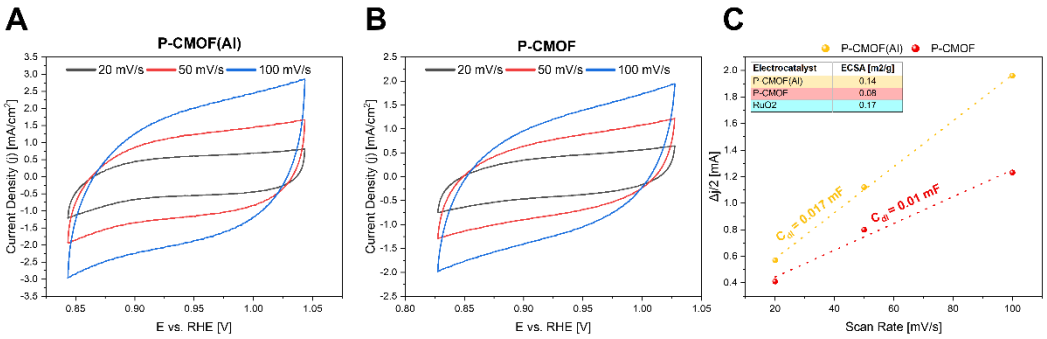

Figure 53. CV plots of P-CMOF(Al) (A), P-CMOF (B) and linear regression between the current density differences in the middle of the potential window of CV vs. scan rates (C) with calculated ECSA (inset).

both P-CMOF(Al) and P-CMOF display higher system resistance (R1) compared to the reference material, with values of 1.75 Ω, 1.51 Ω, and 0.95 Ω, respectively. However, the resistances associated with the reaction kinetics (R2) reveal that P-CMOF(Al) has the lowest resistance, while P-CMOF exhibits the highest, with values of 2.56 Ω and 6.14 Ω, respectively.

Figure 53 exhibits the cyclic voltammetry plots for P-CMOF(Al) and P-CMOF. The obtained data was employed to calculate the C_{dl}, as depicted in Figure 53C. Subsequently, the calculated C_{dl} values were utilized to determine the ECSA. For P-CMOF(Al), the ECSA was determined to be 0.14 m^2/g, which closely resembles the ECSA of RuO_2 at 0.17 m^2/g. However, upon removing the aluminium component, the ECSA decreased to 0.08 m^2/g for P-CMOF.

In summary, phosphorus doping shows excellent OER results; however, aluminium is necessary to improve electrochemical properties. P-CMOF(Al) demonstrates excellent OER performance with high ECSA value, approaching that of the reference material.

3. Insights into the mechanism of OER catalysis by MOF

To elucidate the underlying processes responsible for the favourable electrocatalytic performance in the oxygen evolution reaction (OER), the electrocatalysts were examined using transmission electron microscopy (TEM) and X-ray photoelectron spectroscopy (XPS) after the polarization process. Specifically, the CMOF-Co(Al) material was analyzed after polarization at the OER potential, as shown in Figure 54. TEM analysis revealed the formation of newly formed structures on the electrocatalyst surface, exhibiting a d-spacing of 0.24 nm. It was confirmed that these structures were formed as a result of the reaction of cobalt from the Co-Al alloy, leading to the formation of reactive CoOOH species through oxidation. This finding is supported by the XPS analysis presented in Figure 54B, where Co-Al bonding disappeared from the aluminium spectrum. Thus, it can be concluded that during polarization, distinct active species are generated on the electrocatalyst surface. No other significant changes were observed, indicating the excellent stability of CMOF-Co(Al) as structural integrity remained intact. These observations further support the durability and reliability of the CMOF-Co(Al) material as an efficient electrocatalyst for the OER. These TEM and XPS analyses provide valuable insights into the structural changes and chemical transformations occurring on the electrocatalyst surface during OER. The formation of reactive species

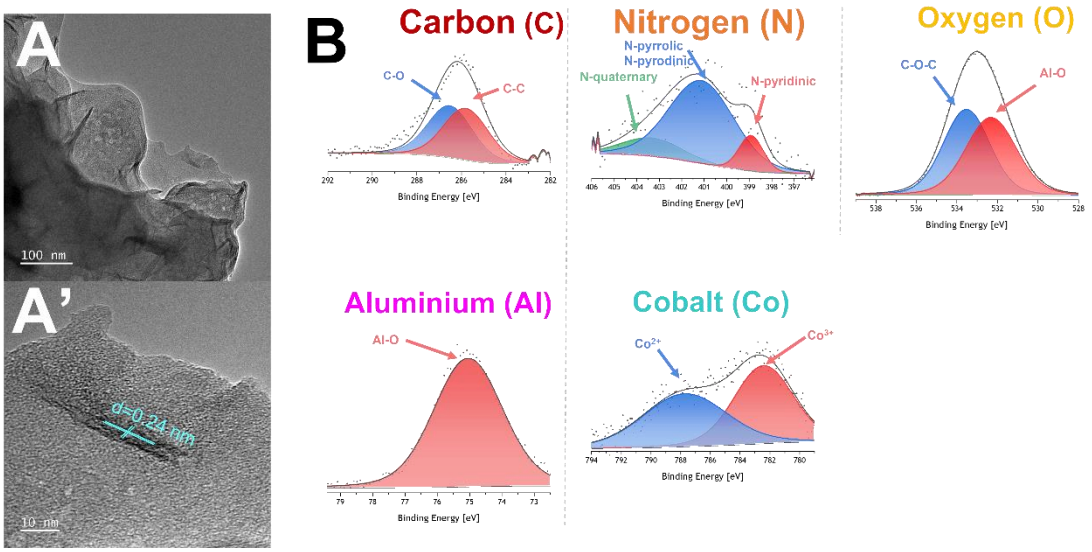

Figure 54. TEM images (A,A') and XPS analysis (B) of CMOF-Co(Al).

and the preservation of the catalyst's structural integrity contribute to its superior electrochemical performance. This reinforces its potential as a highly stable and effective catalyst for the OER process.

To gain a deeper understanding of the individual components and the underlying mechanism behind the excellent electrochemical performance observed in the oxygen evolution reaction (OER) for P-doped Al-MOF-based structures, TEM and XPS analyses were conducted on P-CMOF(Al). TEM analysis, presented in Figures 55A and 55A', revealed the formation of metallic structures on the surface of P-CMOF(Al). This observation was further confirmed by XPS analysis, as shown in Figure 55B, where AlP bonds disappeared in the aluminium spectrum. These findings indicate that the AlP component reacts with water molecules, resulting in the formation of aluminium oxide structures (as confirmed by TEM) and the release of gaseous PH_3. Consequently, during polarization at the OER potential, a portion of the phosphorus is expelled from the electrocatalyst, while the formed aluminium oxide (Al_2O_3) stabilizes the structure and reduces resistance. These results shed light on the role played by each component. They provide insights into the mechanism underlying P-CMOF(Al)'s enhanced electrochemical performance in the OER. The formation of metallic structures on the surface, accompanied by the transformation of AlP (after carbonization) to $Al(OH)_3$ and after the polarization to Al_2O_3, contributes to the stabilization of the catalyst structure and resistance reduction. This, in turn, improves the overall electrochemical performance and highlights the potential of P-doped Al-MOF-based structures as efficient and stable electrocatalysts for OER applications.

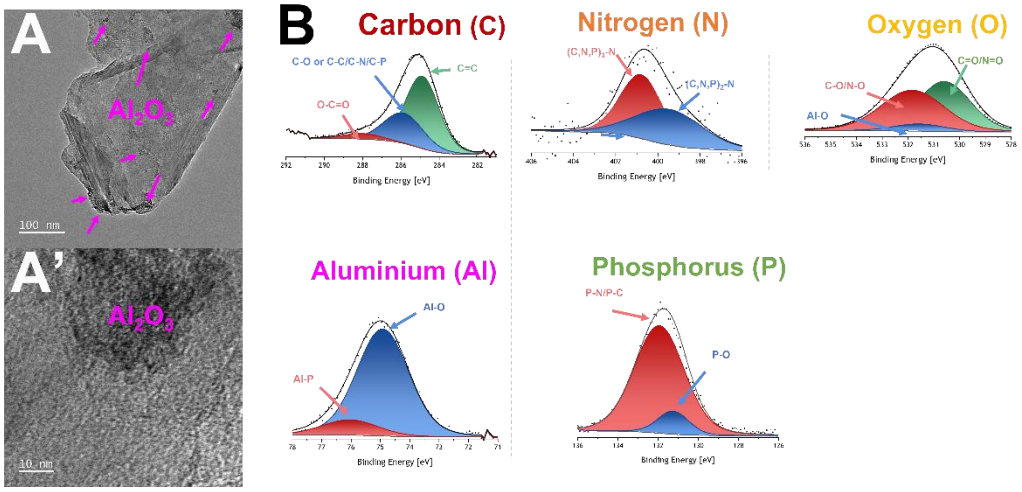

Figure 55. TEM images (A,A') and XPS spectra (B) of P-CMOF(Al).

In summary, despite the different approaches taken for functionalization and morphological changes of the structures, a key element that unifies the underlying mechanisms is the crucial role of aluminium's presence as summarised in Figure 56. Aluminium plays a dual role in both functionalization processes involving phosphorus and cobalt, as well as in the oxygen evolution reaction (OER) mechanism for P-CMOF(Al) and Co-CMOF(Al) electrocatalysts, leading to the formation of Al_2O_3 and CoOOH on the catalyst surface. Furthermore, the presence of aluminium serves to stabilize the structure, enhancing its durability even under harsh conditions encountered during the OER. Additionally, aluminium reduces resistances during the OER, improving electrocatalytic kinetics. Taken together, these findings highlight the significance of aluminium in the functionalization and electrochemical performance of catalysts.

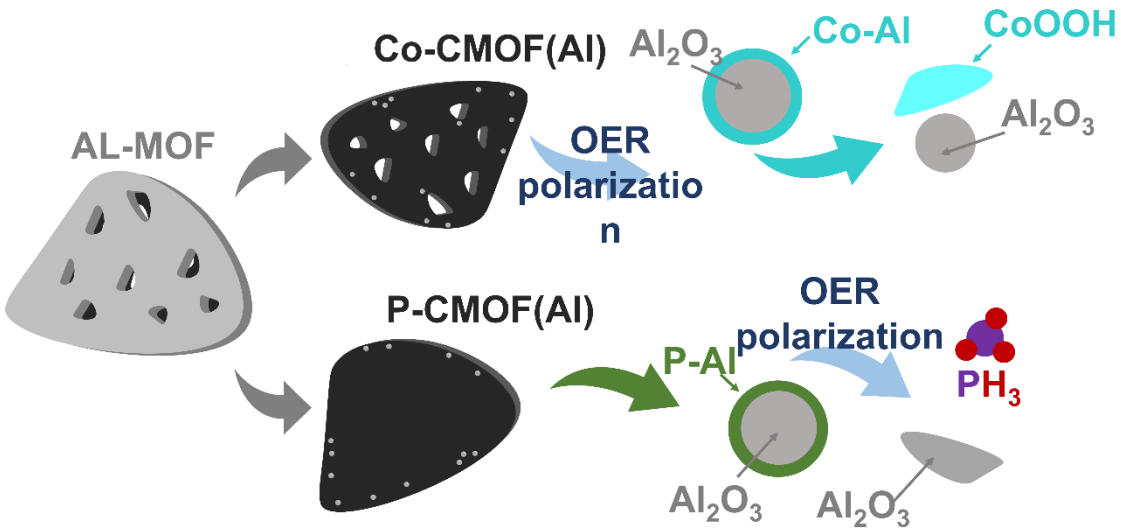

Figure 56. Schematic representation of two functionalization approaches and their mechanisms followed by importance of aluminium's presence.

Aluminium's dual role in facilitating functionalization and contributing to the OER mechanism, along with its ability to stabilize the structure and improve kinetics, underscores its crucial importance in the design and development of efficient and durable electrocatalysts.

Chapter VI: Conclusion and Future Work

1. Summary of the thesis

The PhD thesis focuses on the utilization of Al-MOF (aluminium-based metal-organic framework) for electrochemical water splitting, specifically the oxygen evolution reaction (OER) and hydrogen evolution reaction (HER) - both crucial steps in water electrolysis. The research investigates various aspects of the synthesis and modification processes involved in transforming Al-MOF into a carbon platform for functionalization with phosphorus and cobalt.

Significant emphasis is placed on the carbonization step. This is identified as a critical stage in the design and utilization of a carbonized Al-MOF (CMOF) structure. The optimal structure is achieved through pyrolysis of Al-MOF at 750˚C, which results in a highly defective and thus highly active carbon platform. The thesis extensively examines the deposition of cobalt (Co) on CMOF and its integration into the carbon matrix, employing various analysis methods to optimize the process by identifying key parameters and species. The polarization process is also studied, revealing structural transformations in detail.

Co-functionalized CMOF electrochemical properties exhibit excellent performance, successfully challenging the commercial catalyst RuO_2. Furthermore, the functionalization of CMOF with phosphorus (P) is shown to not only promote healing of the carbon matrix but also significantly enhance the electrochemical properties, rivalling the performance of RuO_2. Mechanism analysis and studies underscore the importance of aluminium’s presence throughout functionalization and OER processes.

In addition, the thesis investigates CMOF functionalization with nickel (Ni) and its performance in HER. However, achieving performance comparable to platinum (Pt), which is known for its superior performance in HER, remains a challenge for the materials studied in this research.

Overall, the thesis provides a comprehensive exploration of Al-MOF-based electrocatalysts for OER and HER, highlighting the critical role of carbonization, demonstrating the success of Co and P functionalization, and revealing the significance of aluminium’s presence. While the materials studied show promising electrochemical properties, further advancements are needed to overcome platinum's performance levels in HER.

2. Implications of the findings

The thesis findings have several profound implications for the field of electrochemical water splitting and the development of efficient catalysts in carbon-based materials. These implications can be further elaborated as follows:

1. Utilization of Al-MOF: The research highlights the potential of utilizing Al-MOF as a versatile platform for electrocatalysis. By carbonizing Al-MOF, a highly active and structurally tuneable carbon matrix is obtained, providing a promising foundation for functionalization with various elements and subsequent electrochemical applications.
2. Cobalt (Co) Functionalization: The successful functionalization of CMOF with cobalt and its integration into the carbon matrix offers an alternative to the commonly used commercial catalyst, ruthenium oxide (RuO_2), for the oxygen evolution reaction (OER). The excellent electrochemical properties exhibited by Co-functionalized CMOF indicate its potential as an effective and sustainable catalyst for OER, which is a crucial step in water splitting processes.
3. Phosphorus (P) Functionalization: The introduction of phosphorus into the carbon matrix improves the electrochemical properties of the catalyst. In addition to enhancing catalytic performance, P-functionalization promotes carbon structure healing, which further contributes to the catalyst's stability and durability. This finding opens up new possibilities for enhancing carbon-based electrocatalyst performance, positioning them as viable alternatives to conventional catalysts such as RuO_2.
4. Role of Aluminium (Al): The research emphasizes the crucial role of aluminium throughout the functionalization process and OER mechanism. Aluminium plays a dual role by facilitating the functionalization of the carbon matrix through binding with other elements such as cobalt and phosphorus. Additionally, aluminium stabilizes the catalyst structure, leading to improved durability during OER harsh conditions. Moreover, the presence of aluminium contributes to decreased resistances, thereby enhancing the kinetics of the OER process.
5. Nickel (Ni) Functionalization: Although Ni-functionalized CMOF in the hydrogen evolution reaction (HER) is yet to match platinum (Pt), the research provides valuable insights into alternative HER catalyst design and development. Further advancements in Ni-functionalization hold the potential to bridge the performance gap and offer cost-effective alternatives to Pt, which is a precious and expensive catalyst.

In summary, the findings suggest that Al-MOF-based catalysts, functionalized with elements such as cobalt and phosphorus, demonstrate promising prospects for achieving efficient electrocatalysis in water-splitting processes. The understanding of aluminium's role and the insights gained from this research can inform the development of novel and effective electrocatalysts for renewable energy generation through water electrolysis. These findings pave the way for further investigations and advancements in the field, driving the development of sustainable and economical catalysts for future energy applications.

3. Future directions for research

The research conducted on Al-MOF-based electrocatalysts and their functionalization opens up several exciting avenues for future investigations and applications. The findings provide a solid foundation for further research and offer valuable insights into advancing electrochemical water splitting. Future perspective for those studies:

1. Optimization of Functionalization: while research has demonstrated successful Al-MOF functionalization with cobalt, phosphorus, and nickel, further optimization of these processes is warranted. Future studies can focus on fine-tuning functionalization parameters, such as precursor concentrations, reaction conditions, and deposition techniques, to enhance the catalytic activity and stability of the materials. This optimization will contribute to the development of more efficient and cost-effective electrocatalysts.
2. Mechanistic Understanding: deeper insights into the mechanistic aspects of the functionalization processes and the subsequent OER and HER mechanisms are essential for further improvement of the catalysts. Advanced characterization techniques, such as in situ spectroscopy and operando measurements, can provide real-time information about active sites, reaction intermediates, and electron transfer processes. This understanding will enable the rational design of enhanced performance catalysts.
3. Catalyst Engineering: the research opens up opportunities for catalyst engineering through the controlled synthesis of Al-MOF with tailored structures and porosities. By manipulating Al-MOF composition and morphology, it is possible to optimize their catalytic properties and tailor them to specific electrochemical reactions. Future work can focus on exploring various synthesis strategies, such as template-assisted

synthesis, doping with additional elements, or hybridization with other materials, to further enhance catalytic performance.

4. Scalability and Cost-Effectiveness: as electrochemical water splitting technologies move towards commercialization, scalability and cost-effectiveness become critical factors. Future research can focus on developing scalable synthesis methods for Al-MOF-based catalysts while maintaining their catalytic activity and stability. Additionally, efforts can be directed towards utilizing abundant and low-cost materials as precursors for functionalization, reducing the reliance on expensive or scarce elements, such as ruthenium or platinum.
5. Integration into Device Architectures: to realize the practical implementation of Al-MOF-based electrocatalysts, their integration into device architectures, such as electrolyzers or fuel cells, is crucial. Future research can explore the fabrication of functionalized Al-MOF catalysts as electrodes and their integration into complete electrochemical devices. This will involve understanding the interactions between the catalysts, electrolytes, and supporting materials. In addition, it will involve optimizing the device design for efficient mass transport and charge transfer.
6. Beyond Water Splitting: while the research focuses on water splitting, the insights gained from Al-MOF-based electrocatalysts can potentially be extended to other energy conversion and storage processes. Future studies can explore the applicability of these catalysts to other electrochemical reactions, such as carbon dioxide reduction, nitrogen fixation, or rechargeable metal-air batteries. This broad scope of applications will contribute to sustainable energy technology development.

In conclusion, the research on Al-MOF-based electrocatalysts offers a solid foundation for future investigations and opens up exciting possibilities for advancing electrochemical water splitting. By addressing the outlined future perspectives, researchers can further optimize these catalysts. This will deepen our understanding of their mechanisms, and drive their practical application in sustainable energy conversion and storage systems. Moreover, development of hydrogen generation through water electrolysis can significantly challenge energetic sector and replace other hydrogen generation methods such as “grey hydrogen”.

List of publications

1. Aleksandrzak, M., Baranowska, D., Kedzierski, T., **Sielicki, K.**, Zhang, S., Biegun, M., & Mijowska, E. (2019). Superior synergy of g-C3N4/Cd compounds and Al-MOF-derived nanoporous carbon for photocatalytic hydrogen evolution. Applied Catalysis B: Environmental, 257. https://doi.org/10.1016/j.apcatb.2019.117906; **IF=24.219, MEiN =200**

2. Aleksandrzak, M., Jedrzejczak-Silicka, M., **Sielicki, K.**, Piotrowska, K., & Mijowska, E. (2019). Size-Dependent In Vitro Biocompatibility and Uptake Process of Polymeric Carbon Nitride. ACS Applied Materials & Interfaces, 0(ja). https://doi.org/10.1021/acsami.9b17427; **IF=10.383, MEiN=200**

3. Aleksandrzak, M., **Sielicki, K.**, & Mijowska, E. (2020). Enhancement of photocatalytic hydrogen evolution with catalysts based on carbonized MOF-5 and g-C 3 N 4. RSC Advances, 10(7), 4032–4039. https://doi.org/10.1039/C9RA08388J; **IF=4.036, MEiN=100**

4. Dymerska, A., Zielińska, B., **Sielicki, K.**, Chen, X., & Mijowska, E. (2022). Porous silica matrix as an efficient strategy to boosted photocatalytic performance of titania/carbon composite. Diamond and Related Materials, 125. https://doi.org/10.1016/j.diamond.2022.109027; **IF=3.806, MEiN=100**

5. Li, J., Dou, F., Gong, J., Gao, Y., Hua, Y., **Sielicki, K.**, Zhang, D., Mijowska, E., & Chen, X. (2023). Recycling of Plastic Wastes for the Mass Production of Yolk–Shell-Nanostructured Co 3 O 4 @C for Lithium-Ion Batteries. ACS Applied Nano Materials. https://doi.org/10.1021/acsanm.2c04757; **IF=6.14, MEiN=20**

6. **Sielicki, K.**, Aleksandrzak, M., & Mijowska, E. (2020). Oxidized SWCNT and MWCNT as co-catalysts of polymeric carbon nitride for photocatalytic hydrogen evolution. Applied Surface Science, 508, 145144. https://doi.org/10.1016/j.apsusc.2019.145144; **IF=7.392, MEiN=140**

7. **Sielicki, K.**, Chen, X., & Mijowska, E. (2023). The role of aluminium in metal-organic frameworks derived carbon doped with cobalt in electrocatalytic oxygen evolution reaction. Materials & Design, 112021. https://doi.org/10.1016/J.MATDES.2023.112021; **IF=9.417, MEiN=140**

8. **Sielicki, K.**, Maślana, K., Chen, X., & Mijowska, E. (2022). Bottom up approach of metal assisted electrochemical exfoliation of boron towards borophene. Scientific Reports, 12(1), 1–7. https://doi.org/10.1038/s41598-022-20130-w; **IF=4.996, MEiN=140**

9. Wang, Y., Jiang, D., Wen, X., Tang, T., Szymańska, K., **Sielicki, K.**, Wenelska, K., & Mijowska, E. (2021). Investigating the Effect of Aluminum Diethylphosphinate on Thermal Stability, Flame Retardancy, and Mechanical Properties of Poly(butylene succinate). Frontiers in Materials, 8. https://doi.org/10.3389/fmats.2021.737749; **IF=3.985, MEiN=70**

10. Xu, X., **Sielicki, K.**, Min, J., Li, J., Hao, C., Wen, X., Chen, X., & Mijowska, E. (2022). One-step converting biowaste wolfberry fruits into hierarchical porous carbon and its application for high-performance supercapacitors. Renewable Energy, 185, 187–195. https://doi.org/10.1016/j.renene.2021.12.040; **IF=8.634, MEiN=140**

11. Zhang, S., Galiński, M., Liu, X., **Sielicki, K.**, Chen, X., Chu, P. K., Holze, R., & Mijowska, E. (2021). Investigation of the microstructure on the nanoporous carbon based capacitive performance. Microporous and Mesoporous Materials, 310, 110629. https://doi.org/10.1016/J.MICROMESO.2020.110629; **IF=5.876, MEiN=100**

12. Czerniawska E., **Sielicki K.**, Maślana K., & Mijowska E. In vivo study on borophene nanoflakes interaction with Tenebrio molitor beetle - viability of hemocytes and short-term immunity effect. Scientific Reports (under review); **IF=4.996, MEiN=140**

13. Dymerska A., Środa B., **Sielicki K.**, Leniec G., Zielińska B., & Mijowska E. Robust and highly efficient electrocatalyst based on ZIF-67 and Ni2+ dimers for oxygen evolution reaction: in situ mechanistic insight. Journal of Energy Chemistry (under review); **IF=13.599, MEiN=100**

14. **Sielicki K.**, & Mijowska E. Fallen autumn leaves – the source of highly porous carbon for Zn-ion hybrid supercapacitors. **Submitted**

15. **Sielicki K.**, Matlak A., Chen X., & Mijowska E. Role of Phosphorus and Al in N-doped carbon derived from metal-organic frameworks for electrocatalytic oxygen evolution reaction. **Submitted**

16. Maślana K., **Sielicki K.**, & Mijowska E. Borophene oxide derivative enriched with B2O3 phase as metal-free electrocatalysts in oxygen evolution reaction. **Submitted**

References

[1] EUR-Lex - 52023PC0160 - EN - EUR-Lex, (n.d.). https://eur-lex.europa.eu/legal-content/EN/TXT/?uri=CELEX%3A52023PC0160 (accessed May 16, 2023).

[2] Use of electricity - U.S. Energy Information Administration (EIA), (n.d.). https://www.eia.gov/energyexplained/electricity/use-of-electricity.php (accessed April 15, 2023).

[3] Electricity production, consumption and market overview - Statistics Explained, (n.d.). https://ec.europa.eu/eurostat/statistics-explained/index.php?title=Electricity_production,_consumption_and_market_overview (accessed April 15, 2023).

[4] Energy use booming in Southeast Asia, (n.d.). https://www.enerdata.net/publications/executive-briefing/growing-economy-access-electricity-mean-booming-energy-use-southeast-asia.html (accessed April 15, 2023).

[5] Ashley Lawson, Decarbonizing U.S. Power - Center for Climate and Energy SolutionsCenter for Climate and Energy Solutions, (2018). https://www.c2es.org/document/decarbonizing-u-s-power/ (accessed April 15, 2023).

[6] D. Lüthi, M. Le Floch, B. Bereiter, T. Blunier, J.M. Barnola, U. Siegenthaler, D. Raynaud, J. Jouzel, H. Fischer, K. Kawamura, T.F. Stocker, High-resolution carbon dioxide concentration record 650,000-800,000 years before present, Nature. 453 (2008) 379–382. https://doi.org/10.1038/NATURE06949.

[7] Energy: China’s renewables progress comes alongside a coal power boom, (n.d.). https://www.cnbc.com/2023/03/08/energy-chinas-renewables-progress-comes-alongside-a-coal-power-boom.html (accessed April 15, 2023).

[8] Renewable energy targets, (n.d.). https://energy.ec.europa.eu/topics/renewable-energy/renewable-energy-directive-targets-and-rules/renewable-energy-targets_en (accessed April 17, 2023).

[9] Clean Energy Future | U.S. Department of the Interior, (n.d.). https://www.doi.gov/priorities/clean-energy-future (accessed April 17, 2023).

[10] S. O'Meara, Y. Ye, Four research teams powering China's net-zero energy goal, Nature. 603 (2022) S41–S43. https://doi.org/10.1038/D41586-022-00801-4.

[11] Japan's New Basic Energy Plan until 2030 approved | EU-Japan, (n.d.). https://www.eu-japan.eu/news/japans-new-basic-energy-plan-until-2030-approved (accessed April 17, 2023).

[12] EU ban on sale of new petrol and diesel cars from 2035 explained | News | European Parliament, (n.d.). https://www.europarl.europa.eu/news/en/headlines/economy/20221019STO44572/eu-ban-on-sale-of-new-petrol-and-diesel-cars-from-2035-explained (accessed April 17, 2023).

[13] H2Valleys | Mission Innovation Hydrogen Valley Platform, (n.d.). https://h2v.eu/ (accessed April 17, 2023).

[14] Hydrogen valleys in Poland - Portal wodorowy, (n.d.). https://h2poland.eu/en/categories/hydrogen-valleys/public-perception/doliny-wodorowe-w-polsce/ (accessed April 17, 2023).

[15] D.S. (David S. Scott, Smelling land : the hydrogen defense against climate catastrophe, (2007). http://inis.iaea.org/Search/search.aspx?orig_q=RN:39001829 (accessed April 18, 2023).

[16] J. Qi, G. Korotcenkov, Metal Oxides and Related Solids for Electrocatalytic Water Splitting, Metal Oxides and Related Solids for Electrocatalytic Water Splitting. (2022) 1–380. https://doi.org/10.1016/C2020-0-02924-5.

[17] H. Meng, Deep desulfurization of sintering flue gas in iron and steel works based on low-temperature oxidation, Open Chem. 18 (2020) 1370–1380. https://doi.org/10.1515/CHEM-2020-0169/MACHINEREADABLECITATION/RIS.

[18] S.S. Penner, Steps toward the hydrogen economy, Energy. 31 (2006) 33–43. https://doi.org/10.1016/J.ENERGY.2004.04.060.

[19] A. Haryanto, S. Fernando, N. Murali, S. Adhikari, Current status of hydrogen production techniques by steam reforming of ethanol: A review, Energy and Fuels. 19 (2005) 2098–2106.

https://doi.org/10.1021/EF0500538/ASSET/IMAGES/LARGE/EF0500538F00003.JPEG.

[20] A. Fujishima, K. Honda, Electrochemical Photolysis of Water at a Semiconductor Electrode, Nature 1972 238:5358. 238 (1972) 37–38. https://doi.org/10.1038/238037a0.

[21] R. Marschall, 50 Years of Materials Research for Photocatalytic Water Splitting, Eur J Inorg Chem. 2021 (2021) 2435–2441. https://doi.org/10.1002/EJIC.202100264.

[22] M. Yu, E. Budiyanto, H. Tüysüz, Principles of Water Electrolysis and Recent Progress in Cobalt-, Nickel-, and Iron-Based Oxides for the Oxygen Evolution Reaction, Angewandte Chemie International Edition. 61 (2022) e202103824. https://doi.org/10.1002/ANIE.202103824.

[23] S. Jayabal, G. Saranya, J. Wu, Y. Liu, D. Geng, X. Meng, Understanding the high-electrocatalytic performance of two-dimensional MoS2 nanosheets and their composite materials, J Mater Chem A Mater. 5 (2017) 24540–24563. https://doi.org/10.1039/C7TA08327K.

[24] J.C. Fornaciari, L.C. Weng, S.M. Alia, C. Zhan, T.A. Pham, A.T. Bell, T. Ogitsu, N. Danilovic, A.Z. Weber, Mechanistic understanding of pH effects on the oxygen evolution reaction, Electrochim Acta. 405 (2022) 139810. https://doi.org/10.1016/J.ELECTACTA.2021.139810.

[25] Z. Xiao, X. Huang, L. Xu, D. Yan, J. Huo, S. Wang, Edge-selectively phosphorus-doped few-layer graphene as an efficient metal-free electrocatalyst for the oxygen evolution reaction, Chemical Communications. 52 (2016) 13008–13011. https://doi.org/10.1039/c6cc07217h.

[26] A.A. Alireza, N. Hamnabard, S.M.H. Meshkati, M. Pakan, Y.H. Ahn, Effectiveness of phase- and morphology-controlled MnO2 nanomaterials derived from flower-like δ-MnO2 as alternative cathode catalyst in microbial fuel cells, Dalton Transactions. 48 (2019) 5429–5443. https://doi.org/10.1039/C9DT00520J.

[27] N. Gallandat, K. Romanowicz, A. Züttel, N. Gallandat, K. Romanowicz, A. Züttel, An Analytical Model for the Electrolyser Performance Derived from Materials

Parameters, Journal of Power and Energy Engineering. 5 (2017) 34–49. https://doi.org/10.4236/JPEE.2017.510003.

[28] I. Vincent, E.C. Lee, H.M. Kim, Comprehensive impedance investigation of low-cost anion exchange membrane electrolysis for large-scale hydrogen production, Scientific Reports 2021 11:1. 11 (2021) 1–12. https://doi.org/10.1038/s41598-020-80683-6.

[29] A. Hodges, A.L. Hoang, G. Tsekouras, K. Wagner, C.Y. Lee, G.F. Swiegers, G.G. Wallace, A high-performance capillary-fed electrolysis cell promises more cost-competitive renewable hydrogen, Nature Communications 2022 13:1. 13 (2022) 1–11. https://doi.org/10.1038/s41467-022-28953-x.

[30] S. Shiva Kumar, V. Himabindu, Hydrogen production by PEM water electrolysis – A review, Mater Sci Energy Technol. 2 (2019) 442–454. https://doi.org/10.1016/J.MSET.2019.03.002.

[31] Y. Wang, W. Li, L. Ma, W. Li, X. Liu, Degradation of solid oxide electrolysis cells: Phenomena, mechanisms, and emerging mitigation strategies—A review, J Mater Sci Technol. 55 (2020) 35–55. https://doi.org/10.1016/J.JMST.2019.07.026.

[32] S. Gunduz, D.J. Deka, U.S. Ozkan, Advances in High-Temperature Electrocatalytic Reduction of CO2 and H2O, Advances in Catalysis. 62 (2018) 113–165. https://doi.org/10.1016/BS.ACAT.2018.08.003.

[33] C.I. Igwe, C.H. Achebe, A. Chinweze, Review of alternative energy production methods by oxidation of electrolyzed hydrogen in a hydrogen cell, Global Scientific Journals. 10 (2022) 2032–2050.

[34] Y. Wang, D.F. Ruiz Diaz, K.S. Chen, Z. Wang, X.C. Adroher, Materials, technological status, and fundamentals of PEM fuel cells – A review, Materials Today. 32 (2020) 178–203. https://doi.org/10.1016/J.MATTOD.2019.06.005.

[35] T.B. Ferriday, P.H. Middleton, Alkaline fuel cell technology - A review, Int J Hydrogen Energy. 46 (2021) 18489–18510. https://doi.org/10.1016/J.IJHYDENE.2021.02.203.

[36] Q. Xu, Z. Guo, L. Xia, Q. He, Z. Li, I. Temitope Bello, K. Zheng, M. Ni, A comprehensive review of solid oxide fuel cells operating on various promising

alternative fuels, Energy Convers Manag. 253 (2022) 115175. https://doi.org/10.1016/J.ENCONMAN.2021.115175.

[37] Inamuddin Inamuddin, Tariq A. Altalhi, Sayed Mohammed Adnan, Mohammed A. Amin, eds., Materials for hydrogen production, conversion, and storage, first, John Wiley & Sons, Inc.,Scrivener Publishing LLC, 2023. https://www.wiley.com/en-us/Materials+for+Hydrogen+Production%2C+Conversion%2C+and+Storage-p-9781119829560 (accessed April 30, 2023).

[38] F. Liu, C. Shi, X. Guo, Z. He, L. Pan, Z.F. Huang, X. Zhang, J.J. Zou, Rational Design of Better Hydrogen Evolution Electrocatalysts for Water Splitting: A Review, Advanced Science. 9 (2022) 2200307. https://doi.org/10.1002/ADVS.202200307.

[39] C. Li, J.B. Baek, Recent Advances in Noble Metal (Pt, Ru, and Ir)-Based Electrocatalysts for Efficient Hydrogen Evolution Reaction, ACS Omega. 5 (2020) 31–40. https://doi.org/10.1021/ACSOMEGA.9B03550/ASSET/IMAGES/LARGE/AO9B03550_0013.JPEG.

[40] J. Hu, L. Zhou, G. Sang, C. Xu, Tuning Structure and Properties of Pt Catalysts Confined in Single-Walled Carbon Nanotubes (SWNTs) for Electrocatalysis, ChemNanoMat. 8 (2022) e202200355. https://doi.org/10.1002/CNMA.202200355.

[41] K.L. Zhou, Z. Wang, C.B. Han, X. Ke, C. Wang, Y. Jin, Q. Zhang, J. Liu, H. Wang, H. Yan, Platinum single-atom catalyst coupled with transition metal/metal oxide heterostructure for accelerating alkaline hydrogen evolution reaction, Nature Communications 2021 12:1. 12 (2021) 1–10. https://doi.org/10.1038/s41467-021-24079-8.

[42] D. Yang, J.H. Yang, Y.P. Yang, Z.Y. Liu, High-dispersed ruthenium sites on copper phosphide/graphene for electrocatalytic hydrogen evolution in acidic and alkaline conditions, Appl Catal B. 326 (2023) 122402. https://doi.org/10.1016/J.APCATB.2023.122402.

[43] Y. Zhu, K. Fan, C.-S. Hsu, G. Chen, C. Chen, T. Liu, Z. Lin, S. She, L. Li, H. Zhou, Y. Zhu, H. Ming Chen, H. Huang, Y. Zhu, K. Fan, G. Chen, C. Chen, T. Liu, Z. Lin, S. She, L. Li, H. Zhou, H. Huang, C. Hsu, H.M. Chen, Supported Ruthenium Single-Atom and Clustered Catalysts Outperform Benchmark Pt for Alkaline Hydrogen Evolution, Advanced Materials. (2023) 2301133. https://doi.org/10.1002/ADMA.202301133.

[44] Z. Lei, W. Cai, Y. Rao, K. Wang, Y. Jiang, Y. Liu, X. Jin, J. Li, Z. Lv, S. Jiao, W. Zhang, P. Yan, S. Zhang, R. Cao, Coordination modulation of iridium single-atom catalyst maximizing water oxidation activity, Nature Communications 2022 13:1. 13 (2022) 1–10. https://doi.org/10.1038/s41467-021-27664-z.

[45] C. Peng, W. Zhao, Z. Kuang, J.T. Miller, H. Chen, Boosting neutral hydrogen evolution reaction on iridium by support effect of W18O49, Appl Catal A Gen. 623 (2021) 118293. https://doi.org/10.1016/J.APCATA.2021.118293.

[46] S. Geng, Y. Ji, J. Su, Z. Hu, M. Fang, D. Wang, S. Liu, L. Li, Y. Li, J.M. Chen, J.F. Lee, X. Huang, Q. Shao, Homogeneous Metastable Hexagonal Phase Iridium Enhances Hydrogen Evolution Catalysis, Advanced Science. 10 (2023) 2206063. https://doi.org/10.1002/ADVS.202206063.

[47] Z. Qin, W. Liu, W. Que, J. Feng, W. Shi, F. Wu, X. Cao, Non-noble-metal electrocatalysts for oxygen evolution reaction toward seawater splitting: A review, ChemPhysMater. (2022). https://doi.org/10.1016/J.CHPHMA.2022.11.001.

[48] H. Wu, C. Feng, L. Zhang, J. Zhang, D.P. Wilkinson, Non-noble Metal Electrocatalysts for the Hydrogen Evolution Reaction in Water Electrolysis, Electrochemical Energy Reviews 2021 4:3. 4 (2021) 473–507. https://doi.org/10.1007/S41918-020-00086-Z.

[49] L. Huo, C. Jin, K. Jiang, Q. Bao, Z. Hu, J. Chu, Applications of Nickel-Based Electrocatalysts for Hydrogen Evolution Reaction, Advanced Energy and Sustainability Research. 3 (2022) 2100189. https://doi.org/10.1002/AESR.202100189.

[50] B. Pattengale, Y. Huang, X. Yan, S. Yang, S. Younan, W. Hu, Z. Li, S. Lee, X. Pan, J. Gu, J. Huang, Dynamic evolution and reversibility of single-atom Ni(II) active site in 1T-MoS2 electrocatalysts for hydrogen evolution, Nature

Communications 2020 11:1. 11 (2020) 1–9. https://doi.org/10.1038/s41467-020-17904-z.

[51] X. Liu, Y. Deng, L. Zheng, M.R. Kesama, C. Tang, Y. Zhu, Engineering Low-Coordination Single-Atom Cobalt on Graphitic Carbon Nitride Catalyst for Hydrogen Evolution, ACS Catal. 12 (2022) 5517–5526. https://doi.org/10.1021/ACSCATAL.2C01253/ASSET/IMAGES/MEDIUM/CS2C01253_M009.GIF.

[52] S. Zhou, W. Pei, Y. Zhao, X. Yang, N. Liu, J. Zhao, Low-dimensional non-metal catalysts: principles for regulating p-orbital-dominated reactivity, Npj Computational Materials 2021 7:1. 7 (2021) 1–34. https://doi.org/10.1038/s41524-021-00654-x.

[53] Y. Zheng, Y. Jiao, Y. Zhu, L.H. Li, Y. Han, Y. Chen, A. Du, M. Jaroniec, S.Z. Qiao, Hydrogen evolution by a metal-free electrocatalyst, Nature Communications 2014 5:1. 5 (2014) 1–8. https://doi.org/10.1038/ncomms4783.

[54] W.A. Saidi, T. Nandi, T. Yang, C.A. Wissam Saidi, Designing multinary noble metal-free catalyst for hydrogen evolution reaction, Electrochemical Science Advances. (2022) e2100224. https://doi.org/10.1002/ELSA.202100224.

[55] C. Wang, A. Schechter, L. Feng, Iridium-based catalysts for oxygen evolution reaction in acidic media: Mechanism, catalytic promotion effects and recent progress, Nano Research Energy. 2 (2023) e9120056. https://doi.org/10.26599/NRE.2023.9120056.

[56] M.J. Craig, G. Coulter, E. Dolan, J. Soriano-López, E. Mates-Torres, W. Schmitt, M. García-Melchor, Universal scaling relations for the rational design of molecular water oxidation catalysts with near-zero overpotential, Nature Communications 2019 10:1. 10 (2019) 1–9. https://doi.org/10.1038/s41467-019-12994-w.

[57] W.H. Lee, J. Yi, H.N. Nong, P. Strasser, K.H. Chae, B.K. Min, Y.J. Hwang, H.S. Oh, Electroactivation-induced IrNi nanoparticles under different pH conditions for neutral water oxidation, Nanoscale. 12 (2020) 14903–14910. https://doi.org/10.1039/D0NR02951C.

[58] T. Noor, L. Yaqoob, N. Iqbal, Recent Advances in Electrocatalysis of Oxygen Evolution Reaction using Noble-Metal, Transition-Metal, and Carbon-Based

Materials, ChemElectroChem. 8 (2021) 447–483. https://doi.org/10.1002/CELC.202001441.

[59] H. Bode, K. Dehmelt, J. Witte, Zur kenntnis der nickelhydroxidelektrode—I.Über das nickel (II)-hydroxidhydrat, Electrochim Acta. 11 (1966) 1079–1087. https://doi.org/10.1016/0013-4686(66)80045-2.

[60] L. Zhang, J. Xiao, H. Wang, M. Shao, Carbon-Based Electrocatalysts for Hydrogen and Oxygen Evolution Reactions, ACS Catal. 7 (2017) 7855–7865. https://doi.org/10.1021/ACSCATAL.7B02718/ASSET/IMAGES/LARGE/CS-2017-02718P_0012.JPEG.

[61] Y. Zhou, G. Chen, J. Zhang, A review of advanced metal-free carbon catalysts for oxygen reduction reactions towards the selective generation of hydrogen peroxide, J Mater Chem A Mater. 8 (2020) 20849–20869. https://doi.org/10.1039/D0TA07900F.

[62] Q. Wang, D. Astruc, State of the Art and Prospects in Metal-Organic Framework (MOF)-Based and MOF-Derived Nanocatalysis, Chem Rev. 120 (2020) 1438–1511. https://doi.org/10.1021/ACS.CHEMREV.9B00223/ASSET/IMAGES/MEDIUM/CR-2019-00223Z_0061.GIF.

[63] L. Feng, G.S. Day, K.Y. Wang, S. Yuan, H.C. Zhou, Strategies for Pore Engineering in Zirconium Metal-Organic Frameworks, Chem. 6 (2020) 2902–2923. https://doi.org/10.1016/J.CHEMPR.2020.09.010.

[64] J.E. Cun, X. Fan, Q. Pan, W. Gao, K. Luo, B. He, Y. Pu, Copper-based metal–organic frameworks for biomedical applications, Adv Colloid Interface Sci. 305 (2022) 102686. https://doi.org/10.1016/J.CIS.2022.102686.

[65] G.S. Day, G.T. Rowe, C. Ybanez, R.O. Ozdemir, J. Ornstein, Evaluation of Iron-Based Metal-Organic Framework Activation Temperatures in Acetylene Adsorption, Inorg Chem. 61 (2022) 9242–9250. https://doi.org/10.1021/ACS.INORGCHEM.2C00890/SUPPL_FILE/IC2C00890_SI_001.ZIP.

[66] J. Joseph, S. Iftekhar, V. Srivastava, Z. Fallah, E.N. Zare, M. Sillanpää, Iron-based metal-organic framework: Synthesis, structure and current technologies for water

reclamation with deep insight into framework integrity, Chemosphere. 284 (2021) 131171. https://doi.org/10.1016/J.CHEMOSPHERE.2021.131171.

[67] T. Steenhaut, Y. Filinchuk, S. Hermans, Aluminium-based MIL-100(Al) and MIL-101(Al) metal–organic frameworks, derivative materials and composites: synthesis, structure, properties and applications, J Mater Chem A Mater. 9 (2021) 21483–21509. https://doi.org/10.1039/D1TA04444C.

[68] H. Xiao, W. Zhang, Q. Yao, L. Huang, L. Chen, B. Boury, Z. Chen, Zn-free MOFs like MIL-53(Al) and MIL-125(Ti) for the preparation of defect-rich, ultrafine ZnO nanosheets with high photocatalytic performance, Appl Catal B. 244 (2019) 719–731. https://doi.org/10.1016/J.APCATB.2018.11.026.

[69] Y. Zhang, S. Liu, Z.S. Zhao, Z. Wang, R. Zhang, L. Liu, Z.B. Han, Recent progress in lanthanide metal–organic frameworks and their derivatives in catalytic applications, Inorg Chem Front. 8 (2021) 590–619. https://doi.org/10.1039/D0QI01191F.

[70] Q. Huo, J. Li, X. Qi, G. Liu, X. Zhang, B. Zhang, Y. Ning, Y. Fu, J. Liu, S. Liu, Cu, Zn-embedded MOF-derived bimetallic porous carbon for adsorption desulfurization, Chemical Engineering Journal. 378 (2019) 122106. https://doi.org/10.1016/J.CEJ.2019.122106.

[71] C.W. Ashling, D.N. Johnstone, R.N. Widmer, J. Hou, S.M. Collins, A.F. Sapnik, A.M. Bumstead, P.A. Midgley, P.A. Chater, D.A. Keen, T.D. Bennett, Synthesis and Properties of a Compositional Series of MIL-53(Al) Metal-Organic Framework Crystal-Glass Composites, J Am Chem Soc. 141 (2019) 15641–15648. https://doi.org/10.1021/JACS.9B07557/ASSET/IMAGES/LARGE/JA9B07557_0007.JPEG.

[72] Z. Hu, Y. Wang, D. Zhao, Modulated Hydrothermal Chemistry of Metal-Organic Frameworks, Acc Mater Res. 3 (2022) 1106–1114. https://doi.org/10.1021/ACCOUNTSMR.2C00104/ASSET/IMAGES/MEDIUM/MR2C00104_0008.GIF.

[73] C. McKinstry, R.J. Cathcart, E.J. Cussen, A.J. Fletcher, S. V. Patwardhan, J. Sefcik, Scalable continuous solvothermal synthesis of metal organic framework

(MOF-5) crystals, Chemical Engineering Journal. 285 (2016) 718–725. https://doi.org/10.1016/J.CEJ.2015.10.023.

[74] N. Couzon, M. Ferreira, S. Duval, A. El-Achari, C. Campagne, T. Loiseau, C. Volkringer, Microwave-Assisted Synthesis of Porous Composites MOF-Textile for the Protection against Chemical and Nuclear Hazards, ACS Appl Mater Interfaces. (2022). https://doi.org/10.1021/ACSAMI.2C03247/SUPPL_FILE/AM2C03247_SI_001.PDF.

[75] F. Zarekarizi, A. Morsali, Ultrasonic-assisted synthesis of nano-sized metal-organic framework; a simple method to explore selective and fast Congo Red adsorption, Ultrason Sonochem. 69 (2020) 105246. https://doi.org/10.1016/J.ULTSONCH.2020.105246.

[76] S. Głowniak, B. Szczęśniak, J. Choma, M. Jaroniec, Mechanochemistry: Toward green synthesis of metal–organic frameworks, Materials Today. 46 (2021) 109–124. https://doi.org/10.1016/J.MATTOD.2021.01.008.

[77] J.G. Hinman, J.G. Turner, D.M. Hofmann, C.J. Murphy, Layer-by-Layer Synthesis of Conformal Metal-Organic Framework Shells on Gold Nanorods, Chemistry of Materials. 30 (2018) 7255–7261. https://doi.org/10.1021/ACS.CHEMMATER.8B03341/SUPPL_FILE/CM8B03341_SI_001.PDF.

[78] R. Fan, N. Kang, Y. Li, L. Gao, A template-directed synthesis of metal–organic framework (MOF-74) ultrathin nanosheets for oxygen reduction electrocatalysis, RSC Adv. 11 (2021) 9353–9360. https://doi.org/10.1039/D0RA09973B.

[79] S. Zhang, X. Shi, D. Moszyński, T. Tang, P.K. Chu, X. Chen, E. Mijowska, Hierarchical porous carbon materials from nanosized metal-organic complex for high-performance symmetrical supercapacitor, Electrochim Acta. 269 (2018) 580–589. https://doi.org/10.1016/J.ELECTACTA.2018.03.043.

[80] R. Seetharaj, P. V. Vandana, P. Arya, S. Mathew, Dependence of solvents, pH, molar ratio and temperature in tuning metal organic framework architecture, Arabian Journal of Chemistry. 12 (2019) 295–315. https://doi.org/10.1016/J.ARABJC.2016.01.003.

[81] R. Seetharaj, P. V. Vandana, P. Arya, S. Mathew, Dependence of solvents, pH, molar ratio and temperature in tuning metal organic framework architecture, Arabian Journal of Chemistry. 12 (2019) 295–315. https://doi.org/10.1016/J.ARABJC.2016.01.003.

[82] M. Bhindi, L. Massengo, J. Hammerton, M.J. Derry, S.D. Worrall, Structure Control Using Bioderived Solvents in Electrochemical Metal-Organic Framework Synthesis, Applied Sciences 2023, Vol. 13, Page 720. 13 (2023) 720. https://doi.org/10.3390/APP13020720.

[83] K.A.S. Usman, J.W. Maina, S. Seyedin, M.T. Conato, L.M. Payawan, L.F. Dumée, J.M. Razal, Downsizing metal–organic frameworks by bottom-up and top-down methods, NPG Asia Materials 2020 12:1. 12 (2020) 1–18. https://doi.org/10.1038/s41427-020-00240-5.

[84] Y. Han, H. Yang, X. Guo, Y. Han, H. Yang, X. Guo, Synthesis Methods and Crystallization of MOFs, Synthesis Methods and Crystallization. (2020). https://doi.org/10.5772/INTECHOPEN.90435.

[85] F. Li, J. Li, L. Zhou, S. Dai, Enhanced OER performance of composite Co–Fe-based MOF catalysts via a one-pot ultrasonic-assisted synthetic approach, Sustain Energy Fuels. 5 (2021) 1095–1102. https://doi.org/10.1039/D0SE01750G.

[86] C.P. Wang, Y. Feng, H. Sun, Y. Wang, J. Yin, Z. Yao, X.H. Bu, J. Zhu, Self-Optimized Metal-Organic Framework Electrocatalysts with Structural Stability and High Current Tolerance for Water Oxidation, ACS Catal. 11 (2021) 7132–7143. https://doi.org/10.1021/ACSCATAL.1C01447/ASSET/IMAGES/MEDIUM/CS1C01447_M006.GIF.

[87] F. Shi, Z. Wang, K. Zhu, X. Zhu, W. Yang, Enhancing activity and stability of Co-MOF-74 for oxygen evolution reaction by wrapping polydopamine, Electrochim Acta. 416 (2022) 140293. https://doi.org/10.1016/J.ELECTACTA.2022.140293.

[88] K. Du, L. Zhang, J. Shan, J. Guo, J. Mao, C.C. Yang, C.H. Wang, Z. Hu, T. Ling, Interface engineering breaks both stability and activity limits of RuO2 for sustainable water oxidation, Nature Communications 2022 13:1. 13 (2022) 1–9. https://doi.org/10.1038/s41467-022-33150-x.

[89] K. Sielicki, X. Chen, E. Mijowska, The role of aluminium in metal-organic frameworks derived carbon doped with cobalt in electrocatalytic oxygen evolution reaction, Mater Des. (2023) 112021. https://doi.org/10.1016/J.MATDES.2023.112021.

[90] T. Wang, H.K. Kim, Y. Liu, W. Li, J.T. Griffiths, Y. Wu, S. Laha, K.D. Fong, F. Podjaski, C. Yun, R.V. Kumar, B. V. Lotsch, A.K. Cheetham, S.K. Smoukov, Bottom-up Formation of Carbon-Based Structures with Multilevel Hierarchy from MOF-Guest Polyhedra, J Am Chem Soc. 140 (2018) 6130–6136. https://doi.org/10.1021/JACS.8B02411/ASSET/IMAGES/LARGE/JA-2018-02411J_0004.JPEG.

[91] M. Aleksandrzak, K. Sielicki, E. Mijowska, Enhancement of photocatalytic hydrogen evolution with catalysts based on carbonized mof-5 and g-C3N4, RSC Adv. 10 (2020) 4032–4039. https://doi.org/10.1039/c9ra08388j.

[92] M. Aleksandrzak, K. Sielicki, E. Mijowska, Enhancement of photocatalytic hydrogen evolution with catalysts based on carbonized MOF-5 and g-C3N4, RSC Adv. 10 (2020) 4032–4039. https://doi.org/10.1039/C9RA08388J.

[93] K. Cendrowski, P. Skumial, P. Spera, E. Mijowska, Thermally induced formation of zinc oxide nanostructures with tailoring morphology during metal organic framework (MOF-5) carbonization process, Mater Des. 110 (2016) 740–748. https://doi.org/10.1016/J.MATDES.2016.08.043.

[94] C. Wang, J. Huang, Q. Li, L. Cao, J. Li, K. Kajiyoshi, Catalyzing carbon surface by Ni to improve initial coulombic efficiency of sodium-ion batteries, J Energy Storage. 32 (2020) 101868. https://doi.org/10.1016/J.EST.2020.101868.

[95] L. Jiao, R. Zhang, G. Wan, W. Yang, X. Wan, H. Zhou, J. Shui, S.H. Yu, H.L. Jiang, Nanocasting SiO2 into metal–organic frameworks imparts dual protection to high-loading Fe single-atom electrocatalysts, Nature Communications 2020 11:1. 11 (2020) 1–7. https://doi.org/10.1038/s41467-020-16715-6.

[96] J. Hong, M.K. Park, E.J. Lee, D. Lee, D.S. Hwang, S. Ryu, Origin of New Broad Raman D and G Peaks in Annealed Graphene, Scientific Reports 2013 3:1. 3 (2013) 1–5. https://doi.org/10.1038/srep02700.

[97] Z. Zhao, Y. Long, Y. Chen, F. Zhang, J. Ma, Phosphorus doped carbon nitride with rich nitrogen vacancy to enhance the electrocatalytic activity for nitrogen reduction reaction, Chemical Engineering Journal. 430 (2022) 132682. https://doi.org/10.1016/J.CEJ.2021.132682.

[98] Y. Zhao, R. Nakamura, K. Kamiya, S. Nakanishi, K. Hashimoto, Nitrogen-doped carbon nanomaterials as non-metal electrocatalysts for water oxidation, Nature Communications 2013 4:1. 4 (2013) 1–7. https://doi.org/10.1038/ncomms3390.

[99] F. Meng, S. Wang, B. Jiang, L. Ju, H. Xie, W. Jiang, Q. Ji, Coordinated regulation of phosphorus/nitrogen doping in fullerene-derived hollow carbon spheres and their synergistic effect for the oxygen reduction reaction, Nanoscale. 14 (2022) 10389–10398. https://doi.org/10.1039/D2NR02358J.

[100] B. Wu, H. Meng, D.M. Morales, F. Zeng, J. Zhu, B. Wang, M. Risch, Z.J. Xu, T. Petit, Nitrogen-Rich Carbonaceous Materials for Advanced Oxygen Electrocatalysis: Synthesis, Characterization, and Activity of Nitrogen Sites, Adv Funct Mater. 32 (2022) 2204137. https://doi.org/10.1002/ADFM.202204137.

[101] S.H. Lo, D. Senthil Raja, C.W. Chen, Y.H. Kang, J.J. Chen, C.H. Lin, Waste polyethylene terephthalate (PET) materials as sustainable precursors for the synthesis of nanoporous MOFs, MIL-47, MIL-53(Cr, Al, Ga) and MIL-101(Cr), Dalton Transactions. 45 (2016) 9565–9573. https://doi.org/10.1039/C6DT01282E.

[102] S.K. Springthorpe, C.M. Dundas, B.K. Keitz, Microbial reduction of metal-organic frameworks enables synergistic chromium removal, Nature Communications 2019 10:1. 10 (2019) 1–11. https://doi.org/10.1038/s41467-019-13219-w.